NANOPOROUS LAYERED OXIDE MATERIALS AND MEMBRANES FOR GAS SEPARATIONS

A Thesis
Presented to
The Academic Faculty

by

Wun-gwi Kim

In Partial Fulfillment
of the Requirements for the Degree
Doctor of Philosophy in Chemical Engineering
in the School of Chemical & Biomolecular Engineering

Georgia Institute of Technology
May 2013

NANOPOROUS LAYERED OXIDE MATERIALS AND MEMBRANES FOR GAS SEPARATION

Approved by:

Dr. Sankar Nair, Advisor
School of Chemical & Biomolecular Engineering
Georgia Institute of Technology

Dr. J. Carson Meredith
School of Chemical & Biomolecular Engineering
Georgia Institute of Technology

Dr. Christopher W. Jones
School of Chemical & Biomolecular Engineering
Georgia Institute of Technology

Dr. Meisha L. Shofner
School of Materials Science and Engineering
Georgia Institute of Technology

Dr. William J. Koros
School of Chemical & Biomolecular Engineering
Georgia Institute of Technology

Date Approved: March 7th , 2013

To my lovely wife, Jinook

ACKNOWLEDGEMENTS

I thank God for giving me this gracious opportunity to study in Georgia Tech. The 5 years of life at Georgia Tech and in Atlanta were exciting, joyous and happy, and I will always remember this memorable time.

I would like to thank my advisor, Prof. Sankar Nair, for teaching me with patience. His perfect guidance at each point of my PhD study made this accomplishment possible. I am also grateful to my committee members, Prof. William J. Koros, Prof. J. Carson Meredith, Prof. Christopher Jones and Prof. Meisha L. Shofner for their input towards my PhD research and thesis. It was my pleasure to have these great professors in my thesis committee.

I would like to thank my collaborators Dr. Jong Suk Lee (Koros group) for his help with gas permeation experiments, and Xueyi Zhang (Tsapatsis group, University of Minnesota) for some excellent HR-TEM images. I want to thank all of the previous and current group members in the Nair research group. They shared how to study/research and live in Atlanta. I am also very grateful to the many friends in the ChBE Korean Student Association for sharing their life and their support to living in this community.

I would like to thank my lovely wife Jinook for her love, trust in me, and for the submission of her life to make our family strong. I love you, Jinook.

TABLE OF CONTENTS

Page

LIST OF TABLES

LIST OF FIGURES

SUMMARY

The overall focus of this thesis is on the development and understanding of nanoporous layered silicates and membranes, particularly for potential applications in gas separations. Nanoporous layered materials are a rapidly growing area of interest, and include materials such as layered zeolites, porous layered oxides, layered aluminophosphates, and porous graphenes. They possess unique transport properties that may be advantageous for membrane and thin film applications. These materials also have very different chemistry from 3-D porous materials due to the existence of a large, chemically active, external surface area. This feature also necessitates the development of innovative strategies to process these materials into membranes and thin films with high performance.

Chapter 1 of my thesis presents a review on the state-of-the-art in nanoporous layered materials and membranes. I will first discuss fundamentals of the synthesis and structural characterization of nanoporous layered materials. Thereafter, I will elucidate the different approaches for fabrication of membranes and thin films from these materials followed by the discussion on the applications of such membranes in diverse areas relating to molecular transport and separation, e.g., gas and liquid-phase separations, water purification, fuel cell membranes, and others. This discussion leads to my statement of the main objectives of my thesis and my research strategy.

One objective of this work is to develop effective chemical and mechanical methods for swelling, functionalizing, and exfoliating nanoporous layered materials. Chapter 2 describes the swelling and surface modification chemistry of two attractive nanoporous layered silicate materials, AMH-3 and MCM-22 has been studied. I first describe a method, using long-chain diamines instead of monoamines, for swelling of AMH-3 while preserving its pore structure to a greater extent during the swelling process. Then, I describe a step-wise functionalization method for functionalizing the layer surfaces of AMH-3 and MCM-22 *via* silane condensation reactions. The covalently-attached hydrocarbon chain molecules improved the hydrophobicity of AMH-3, MCM-22 particle surface, and therefore allow the possibility of effectively dispersing these materials in polymer matrices for thin film/membrane applications.

Nanoporous layered silicate/polymer composite membranes are of interest because they can exploit the high aspect ratio of exfoliated selective flakes/layers to enhance molecular sieving and create a highly tortuous transport path for the slower molecules. As another main objective of this thesis, Chapter 3 develops a viable route towards membrane synthesis including active exfoliation process, detailed microstructural characterization, and mixed gas permeation measurements and demonstrated that nanoporous flake/polymer membranes allows significant improvement in gas permeability while maintaining selectivity. I begin with the primary-amine-intercalated porous layered silicate SAMH-3 and show that it can be exfoliated using a high shear rate generated by a high-speed mixer. The exfoliated SAMH-3 flakes were used to form SAMH-3/cellulose acetate (CA) membranes. Their microstructure was

analyzed by small angle X-ray scattering (SAXS), revealing a high degree of exfoliation of AMH-3 layers in the CA membrane with a small number of layers (4-8) in the exfoliated flakes. TEM analysis visualized the thickness of the flakes as 15-30 nm, and is consistent with the SAXS analysis. The CO_2/CH_4 gas separation performance of the CA membrane was significantly increased by incorporating only 2-6 wt% of SAMH-3 flakes. There was a large increase in CO_2 permeability with maintenance of selectivity. This cannot be explained by conventional models of transport in flake-containing membranes, and indicates complex transport paths in the membrane. It is also in contrast to the much higher loadings of isotropic particles required for similar enhancements. The present approach may allow avoidance of particle aggregation and poor interfacial adhesion associated with larger quantities of inorganic fillers.

The synthesis of hybrid zeolitic materials with complex micropore-mesopore structures and morphologies is an expanding area of recent interest for a number of applications. Recent work on layered MFI has shown possible paths to extensive opportunities in exploiting its highly roughened external surface and hierarchical crystal structure. A third objective of this thesis is to expand the range of morphologies and possible applications of such zeolitic materials. In Chapter 4, I describe a new type of hybrid zeolite material, composed of a layered zeolite material grown epitaxially on the surface of a bulk zeolite material. Specifically, layered (2-D) MFI sheets were grown on the surface of bulk MFI crystals of different sizes (300 nm and 10 μm), thereby resulting in a hybrid material containing a unique morphology of interconnected micropores (~0.55 nm) and mesopores (~4 nm). The structure and morphology of this material, referred to

as a 'Bulk MFI-Layered MFI' (BMLM) material, was elucidated by a combination of XRD, TEM, HRTEM, SEM, TGA, and N_2 physisorption techniques. It is conclusively shown that epitaxial growth of the 2-D layered MFI sheets occurs in at least two principal crystallographic directions of the bulk MFI crystal, and possibly in the third direction as well. The BMLM material combines the properties of bulk MFI (micropore network and mechanical support) and 2-D layered MFI (large surface roughness, external surface area, and mesoporosity). As an example of the uses of the BMLM material, it was incorporated into a polyimide and fabricated into a composite membrane with enhanced permeability for CO_2 and good CO_2/CH_4 selectivity for gas separations. SEM-EDX imaging and composition analysis showed that the polyimide and the BMLM interpenetrate into each other, thereby forming a well-adhered polymer/particle microstructure in contrast with the defective interfacial microstructure obtained using bare MFI particles. Analysis of the gas permeation data with the modified Maxwell model also allows the estimation of the effective volume of the BMLM particles, as well as the CO_2 and CH_4 gas permeabilities of the interpenetrated layer at the BMLM/polyimide interface.

The final objective of this thesis is to expand the repertoire of nanoporous layered materials synthesis (using the long-chain surfactant template approach pioneered for layered MFI synthesis) to small-pore zeolitic materials. This would allow us to expand the application areas of nanoporous layered materials to separation of small gas molecules (e.g., H_2) and membrane reactors for efficient separation of light components. Towards this end, I discuss the synthesis of a new layered silicoaluminophosphate (SAPO) material. Detailed structural analysis using XRD, NMR, HR-TEM, and SAED concluded

that the synthesized material has the highly crystalline structure of SAPO-16 with AST crystal topology within the layers. The exfoliated layered SAPO-16 materials could be formed into membranes by coating on porous substrates and may lead to the possibility of H_2 separations using their 6MR pore openings.

CHAPTER 1: INTRODUCTION

1.1 Membrane Separations

Advanced membrane separations have generated much interest in the last decade, owing to their potential for technological impact in the energy, fuels, petrochemical, and renewable chemical sectors.[1-4] The science and engineering of polymeric, inorganic, and polymer/ inorganic composite membranes have already attracted a great deal of interest.

1.1.1 Polymeric membranes

The polymers used for fabricating membranes can be classified as glassy polymers, such as polysulfone or polyimides, and rubbery polymers, like PDMS, depending on the chain length and relaxation time (chain rigidity). While diffusivity and solubility are the main factors that determine the permeability of gases, the permselectivity in glassy polymers is governed by diffusivity differences. Therefore, glassy polymers can separate gas molecules by exploiting size exclusion due to different kinetic diameters.[5,6] However, permselectivity in rubbery polymers is dominated by solubility, so the highly condensable large molecules, such as butanes or pentanes are more permeable than small gases like N_2 in rubbery polymers. This is called 'reverse-selectivity' due to the counter-intuitive separation result. Rubbery polymers are widely used to separate organic vapors from non-condensable gases such as air, N_2.[7,8]

The demand for developing high performance separation membranes in industry is emerging. However, biggest large obstacle to utilize the polymeric membranes in industrial applications is their unsatisfactory separation performance. Polymeric

membranes have a trade-off relationship between selectivity and permeability in gas phase separations as embodied in Robeson's plot.[9]

1.1.2. Inorganic (zeolite) membranes

Zeolites are 3-D nanoporous crystalline materials that can be fabricated into highly selective separation membranes utilizing their molecular sieving nanopores.[10,11] Membranes of various zeolites such as MFI, FAU and LTA are now being developed for separation applications.[12] Despite the two decades of development on zeolite membranes with its promising characteristics of molecular selectivity, and a few commercialized applications such as alcohol dehydration, zeolite membranes are presently not widely utilized in industry for gas separations due to the difficulties in economical synthesis of a defect-free continuous membrane on a large scale. The challenging issues in zeolite membranes, such as scale-up of membrane manufacture and control over defect formation are currently being addressed to realize the industrial applications of zeolite membranes.[13]

1.1.3. Polymer/Inorganic Composite ("Mixed Matrix") membranes

"Mixed matrix" membranes can be prepared by incorporating appropriately chosen inorganic particles in a polymeric membrane. By consisting of both the polymer matrix and inorganic fillers, mixed matrix membranes can combine the advantages of polymers, such as good processibility, and lower cost, as well as those of the inorganic materials, such as high selectivity and thermal/ mechanical stability.[14]

Many research groups have incorporated various kinds of inorganic materials such as zeolites, clays, and other molecular sieves into polymer matrices. Mahajan et al. incorporated zeolite 4A in Matrimid.[15] Carbon molecular sieve was also incorporated in Matrimid.[16] Merkel et al. fabricated fumed-silica nanoparticle/ PMP (4-methyl-2-pentyne) composite membranes to improve the selectivity and throughput of organic vapour.[17] Peinemann incorporated ZSM-5 in a PDMS membrane to improve selectivity using its molecular sieving effect.[18] Also, a MFI and carbon black/PDMS composite has been applied as a pervaporation membrane for alcohol water separation.[19-21] Another effort on mixed matrix membranes was to improve surface compatibility between polymer and zeolite particles. Grignard and solvothermal surface treatments have been developed for surface compatibility, and helped to improve membrane permselectivity.[22,23]

The above works on mixed matrix membranes are quite promising towards the goal of improving the selectivity and permeability of polymer-based membranes. However, the conventional isotropic inorganic fillers often require high particle loadings (>50 wt%) in composite membranes to obtain substantial improvement.[24] Also, the size (usually bigger than 200 nm) of the particles makes it challenging to fabricate the thin (sub-micron) membranes. Porous layered materials have been suggested to overcome the above limitations of isotropic inorganic fillers in mixed matrix membranes.[25-27] Figure 1-1 shows a schematic diagram of a composite membrane incorporating high aspect ratio layered materials. As shown in Figure 1-1, the high aspect ratio layered materials provides longer tortuous paths for larger molecules and effective to decrease the permeability of larger molecules.[28] The thinner shape of layered flakes may have lower

diffusion limitation and larger adsorptive surface area than isotropic particles and possibly result in faster permeation for smaller molecules by comparing it to the thicker isotropic particles.

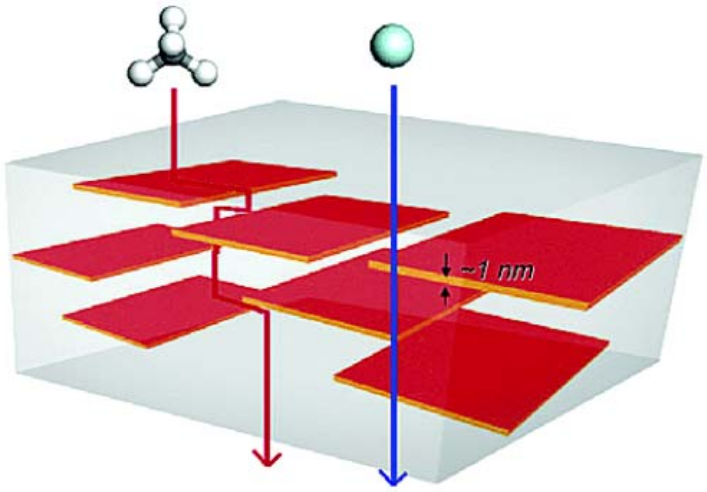

Figure 1-1. Schematic diagram of composite membranes including nanoporous platelets.[25]

More importantly, utilization of the thin layered flakes is interesting because they can be incorporated in ultra-thin membranes such as the skin layer of hollow fiber membranes.[29]

Beyond the utillization of layered materials in composite membranes, thin layered materials can potentially contribute to the formation of high quality inorganic membranes as well. As mentioned earlier, the current fabrication method for inorganic membrane using hydrothermal growth and calcination is having critical problems on defect formation and expensive pricings. So, direct deposition (coating) of layered

materials in porous support can be the alternative way to prevent defect formation during high temperature process. This fabrication method by coating process may have the advantage on control of the membrane thickness by different coating conditions.

1.2. Layered Oxide Materials

Porous layered materials have created recent interest as molecular sieves and heterogeneous catalysts, because they can be exfoliated/delaminated into single-layered (or few-layered) nanostructures, and can provide many acid sites with a large surface area.[30-32]

1.2.1. Clays

A clay is a representative nonporous layered material. The single sheet of clay has the thickness dimension of 1 nm and the crystal structure includes two tetrahedral sheets at the outer surface and 1 inner octahedral sheets. The valency difference between Al and Mg atoms in octrahedral layer creates negative charges as active sites for catalytic applications.[33] Pinnavaia et al. used it as a heterogeneous catalyst by intercalating it with a metal complex, and it shows significant improvements on catalytic properties.[34] Also the structure of clay had been modified to micro/ meso porous materials by a pillaring step[35] and the exfoliated clay had been incorporated in polymer matrix to improve the mechanical/ chemical properties of engineering plastics.[36,37] And lots of effort has also been made to improve barrier properties using the clay materials.[38] By combining it with fuel cell technology, there are active researches on DMFC membranes to decrease methanol crossover by putting exfoliated clay materials in Nafion® membranes.[39-41]

1.2.2. MCM-22

MCM-22 is a porous layered material with a 10-membered ring (MR) pore structures along 2 lateral direction and 6MR pores along the vertical direction[42]. Corma et al. reported the swelling methods for MCM-22 using surfactant intercalation and exfoliated it to single layers to obtain a new layered material named ITQ-2[43]. Different kinds of exfoliated materials such as ITQ-6 and ITQ-18 have been developed by diversifying the initial layered materials to Ferrierite and Nu-6, respectively.[44,45] Also, MCM-36 has been introduced by pillaring MCM-22 after swelling process.[43]

Exfoliated MCM-22 (ITQ-2) is quite attractive for high performance heterogeneous catalysis with its active sites in large surface area. Also, it is very useful as a molecular sieve for H_2 separations with its small pore openings of 6-membered ring perpendicular to the layers. The direct deposition of MCM-22 flakes has been used as the H_2 separation membranes.[46]

1.2.3. AMH-3

AMH-3 is the first 3-D porous layered silicate/layered zeolite, having 8MR pores in all three principal crystallographic directions.[47] Figure 1-2 shows a crystal and pore structure of AMH-3 materials. Single layers of AMH-3 (each of thickness ~ 1 nm) are spaced by charge-balancing Na^+ and Sr^{2+} cations.

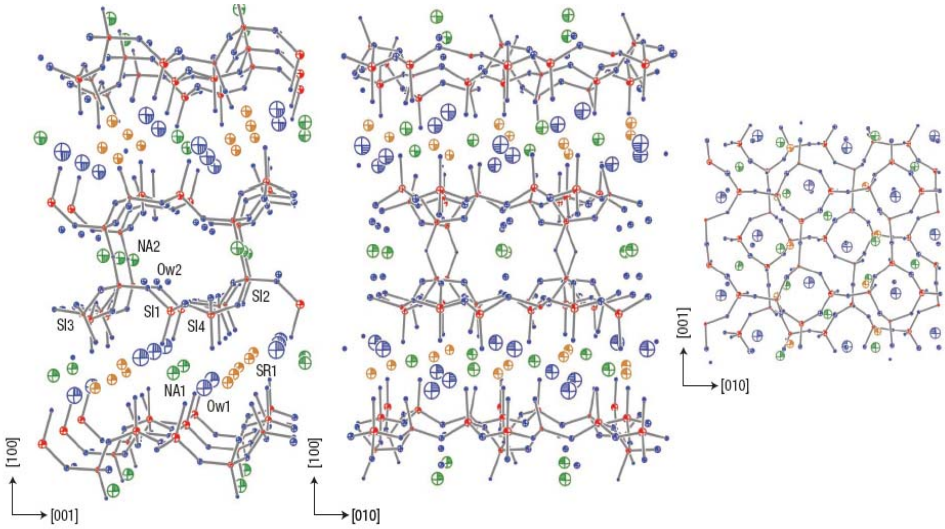

Figure 1-2. Structure of 3-D nanoporous layered silicate, AMH-3[47]

AMH-3 is an attractive candidate as selective flakes because the 8MR pore openings in AMH-3 crystals allow its application in various important gas separations. Table 1-1 shows the Lennard-Jones kinetic diameters of several gases. The nominally 3.4 Å sized pores of AMH-3 can be applied to various combinations of industrial gas separations such as H_2/CO_2 and CO_2/CH_4.

Table 1-1. Lennard-Jones kinetic diameters (in Ångstrom) of various gases[48]

Gas	**He**	**H_2**	**CO_2**	**O_2**	**N_2**	**CH_4**
Kinetic diameter (Å)	2.6	2.89	3.3	3.46	3.64	3.8

A number of challenges have been addressed to apply this novel material in actual gas separation membranes. To overcome the problems on AMH-3 swelling process caused by the strongly bound Na^+ and Sr^{2+} between layers, a sequential intercalation method has been developed and the structural changes occurring in swollen AMH-3 have been elucidated.[49,50]

1.2.4. Layered MFI

Layered MFI is the most recently proposed nanoporous layered material. Choi et al. invented this material by synthesizing a new-conceptual templating agent that has long alkyl chain (C22) in one side.[51] Figure 1-3 shows the synthesis mechanism of layered MFI and resulting layered MFI crystal structure. A long chain alkyl of the template prevents the crystal growth to the b-direction. So, a 2 nm thick layered MFI could be synthesized in one-step hydrothermal reaction. Layered MFI has the same pore size and local structure as conventional MFI. It has 10 MR pores with a nominal pore size of 5.5 Å.[52] This pore size is larger than that of AMH-3, and can be applied to the separation of larger molecules such as hydrocarbons or other organic molecules.

Moreover, as shown in Figure 1-3b, there are 2-3 nm interlayer spacings between each layers taken by micelle. This ‘already swollen’ status of layered MFI is excellent advantage for utilization of this material in actual applications (e.g. catalysis or separation membrane). Because swelling processes usually involve tricky chemical reaction processes such as an ion exchange, intercalation by ammonium, etc.

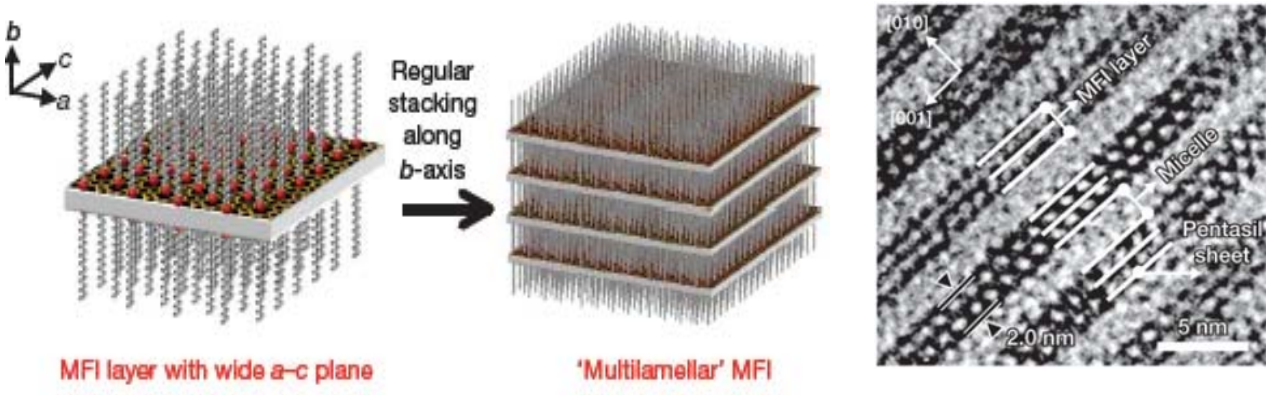

(a) (b)

Figure 1-3. (a) Schematics of Layered MFI assembly, and (b) Layered MFI structure visualized by High Resolution-Transmission Electron Microscopy (HR-TEM)[51]

By controlling the Na^+ content in the reaction gel, two different types of layered MFI, multilamellar and unilamellar, have been synthesized. The pillaring process for layered MFI has expanded its potential applications in heterogeneous catalysis.[53] My thesis research has contributed further advances on this subject by successful synthesis of a hybrid MFI zeolite by epitaxial growth of layered MFI on conventional MFI surfaces.[54]

1.2.5. Porous Alluminophosphates (AlPOs)

Layered aluminophosphate (AlPO) materials are a new class of synthetic AlPOs that have potential applications in catalysis[55] and in fabrication of nanocomposite materials and membranes.[25] By varying structure directing agent (SDA), the AlPO materials can be synthesized to the different forms such as, 1D (chain), 2D (layer), 3D open framework.[56-58] The dimensionality, pore structure, and composition of the AlPO are influenced by the size and shape of the organic (usually amine) SDAs.[56] Within those

varieties, the Layered AlPOs are anionic and their Al:P ratio are lower than unity while the 3-D microporous of AlPOs is having Al:P stoichiometry of 1. The anionic AlPOs contain AlO_4 tetrahedra and $O=PO_3$ (or PO_4) units, with corner-shared oxygen atoms, to form AlPO materials with varying Al/P ratios.[59-61]

Figure 1-4 shows the molecular structure of layered AlPO materials depending on different SDA placed between each layers. The SDA molecules (such as trimethyl-, triethyl-, isopropanolamine) interact with AlPO framework *via* non-covalent bonding, and hence the 2-D layer structures can potentially be delaminated to single layers and enable new applications as catalysts or fabrication of nanocomposite membranes with its large active surface area. I have also contributed to this area by successful synthesis of a a layered silicoaluminophosphate (SAPO) material that may be promising for hydrogen separations.

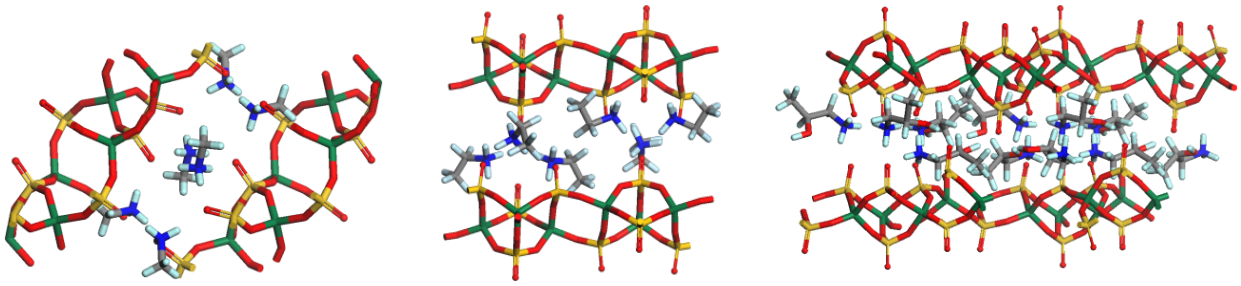

(a) (b) (c)

Figure 1-4. AlPO materials depending on different SDAs: (a) AlPO-trimethylamine (b) AlPO-triethylamine (c) AlPO-Isopropanolamine

1.2.6. Porous graphene

Graphene is a single-atom-thick 2D material with a carbon honeycomb structure. It has a network of sp^2 hybridized carbon atoms that leads to a zero bandgap and enables the fast transport of electrons. Since graphene was first isolated from graphite sheets by mechanical exfoliation methods,[62] scientific interest in the promising electrical, optical and mechanical properties of graphene has grown extremely fast.[63-65] HR-TEM (High Resolution-Transmission Electron Microscopy) visualizes the single and bilayer graphene sheet as shown in Figure 1-5a.[66]

Utilization of graphene as an additive material requires mass-production of graphene sheets. Tung et al obtained single-sheet graphene from graphite oxide by a reduction process using hydrazine.[67] The pore structure has been revealed in detail.[68] This large scale processing of graphene improved the availability of this material. Apart from the tremendous developments on utilizing graphene directly grown on substrates for electronic/ optical applications,[69,70] another important potential application of bulk-processed graphene is in separation membranes.[71] The one-atom-thin layer structure and strong mechanical properties are attractive for application in molecular separation. However, as shown in Figure 1-5a, graphene sheets do not have molecular sieving pores. Therefore, the introduction of sub-nanometer pores is required to obtain sufficient permeance and control the permselectivity. As a proof-of-concept, electron beam lithography has been used to create holes in suspended graphene sheets.[72] However, this 'top-down' fabrication method is hard to control and often not precise. 'Bottom-up' assembly processes are also being considered for the formation of porous 2D sheets of graphene.[73] As shown in the schematics of porous graphene (Figure 1-5b), phenylene

molecules can be the building units for porous graphene.[71] Computational studies have been performed to calculate the separation properties in porous graphenes, indicating interesting molecular sieving possibilities.[71,74,75]

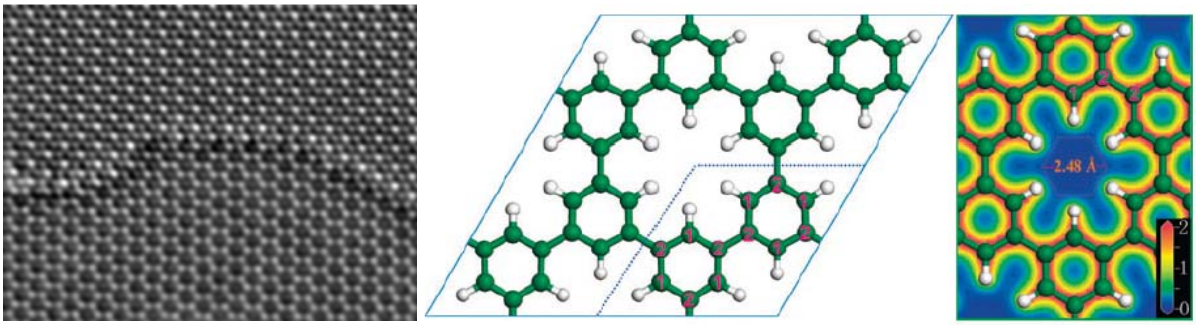

(a) (b)

Figure 1-5. (a) HRTEM image of single and bilayer of graphene[66]; and (b) schematics of porous graphene structure.[71]

1.3. Fabrication of Membranes Containing Layered Oxides

After the preparation of well-defined porous layered materials, there are several important issues in the formation of membranes utilizing layered materials. For both inorganic and nanocomposite membrane fabrication, controlling the exfoliation of the layers is important. As-synthesized or surfactant-swollen layered materials usually are stacks of 100-10,000 layers. So, proper exfoliation processes are key to the fabrication of membranes. Additionally, coating the exfoliated "flakes" on proper substrate or dispersing them in a polymer matrix are important challenges to determine the final performance of the separation membranes.

1.3.1. Exfoliation of Layered Materials

There are many previous studies on polymer/clay composite materials for applications to plastic reinforcement and barrier properties.[28,76-78] These studies contained considerable insight into exfoliation process for clay materials, which served as a useful starting point for my work on porous layered materials. Melt-blending is an attractive conventional method for exfoliative dispersion of layered materials in polymers, and has been used in the majority of studies on exfoliation of clay materials in polymer matrices. This method uses different types of screw extruders to blend molten polymers and layered materials at temperatures of ~400°C. The results depend strongly on the melt-blending conditions and the affinity between the polymer and clay. Depending on the degree of exfoliation, the status of the processed layered materials can be defined as 'immiscible', 'intercalated' and 'exfoliated', as shown in Figure 1-6.[33]

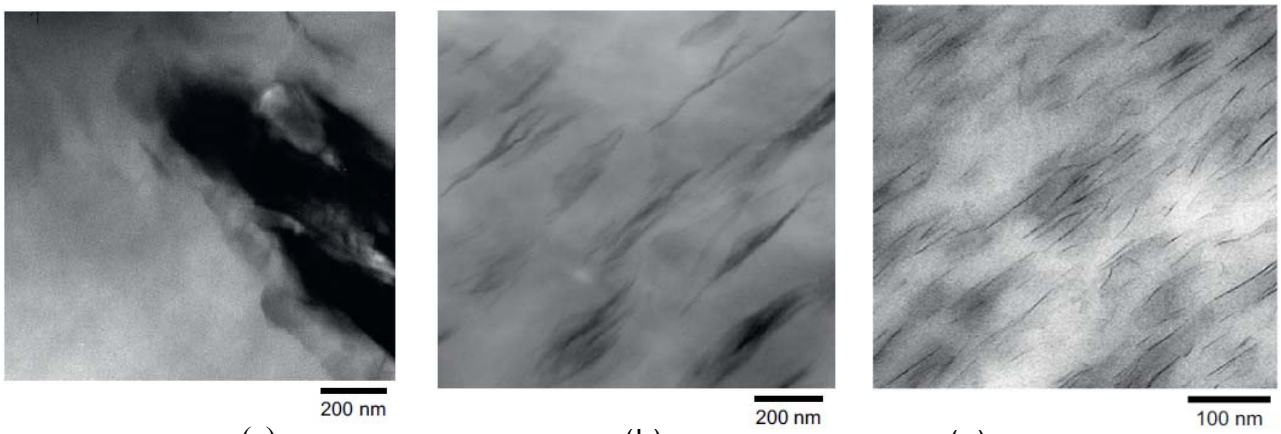

Figure 1-6. Dispersion of clay material depending on degree of exfoliation (a) immisible (b) intercalated (c) exfoliated.[33]

This approach has been applied to the exfoliation of porous layered materials. As shown in Figure 1-7, the layers of MWW and layered MFI have been completely exfoliated using melt blendin.[79] Specifically, the MWW and layered MFI powders have been incorporated in polystyrene and blended using a twin screw extruder.

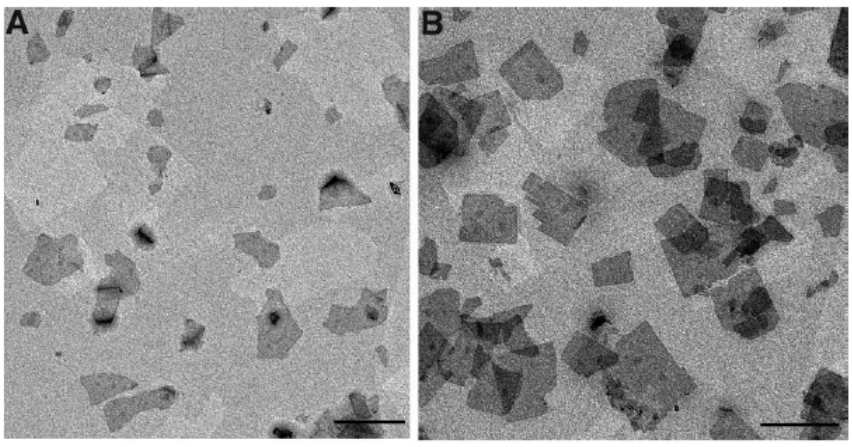

Figure 1-7. Complete exfoliation of (a) layered MWW and (b) layered MFI.[79]

However, processes such as melt-blending are not applicable to the fabrication of nanocomposite membranes for separations, since the polymers required for such applications are usually solution-processed (not melt-processable). Previous attempts to exfoliate porous layered materials have encountered problems such as strong aggregation of the layered materials.[78,80,81] As illustrated in Figure 1-8, this solution blending method includes 2 steps: intercalation of polymer chains between layers, followed by solvent evaporation and formation of nanocomposite membranes.

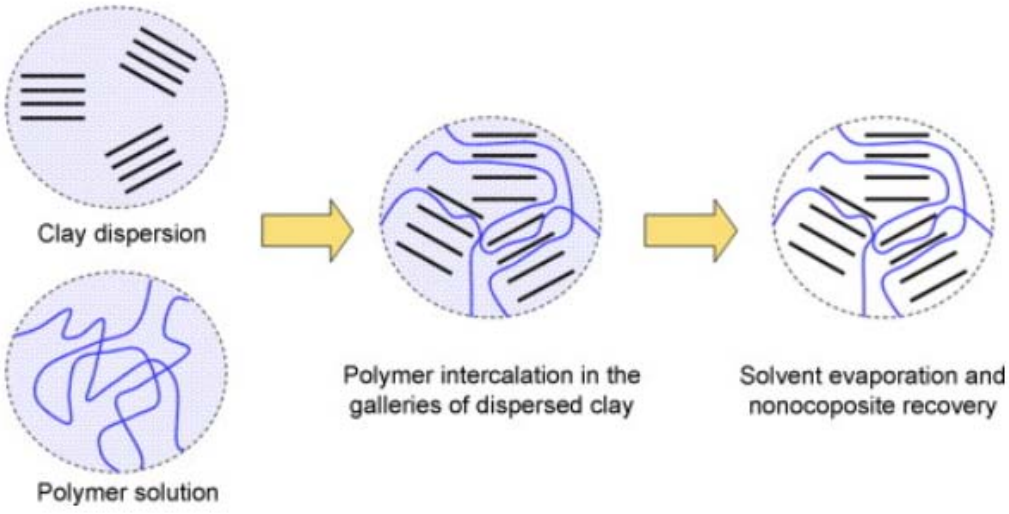

Figure 1-8. Schematics of solution blending process.[78]

Other methods for membrane fabrication with exfoliated layered materials include *in situ* polymerization, sol-gel processing, and solution blending. *In situ* polymerization was used to fabricate clay/Nylon-6 composite materials.[36] The basic idea is to polymerize the monomer in the gallery spaces of layered materials and expand their *d*-spacing, resulting in complete delamination. The advantage of this method is the capability to control the polymerization rate and exfoliation conditions. Using ring-opening polymerization of cyclic oligomers, the exfoliation of clay materials showed significant

improvements.[82] While *in situ* polymerization method involves only the polymerization of monomers, the sol-gel process includes both of the polymerization reaction and crystal growth reaction of inorganic particles at the same time.[78]

1.3.2. Fabrication of Purely Inorganic Membranes

Apart from their processing into nanocomposite membranes, porous layered materials after exfoliation can be directly applied to form inorganic membranes on porous substrates. Common methods for the fabrication of inorganic membranes using exfoliated layered flakes are layer-by-Layer dip coating, spray/spin coating, and vacuum filtration. Post-treatments such as TEOS vapor infiltration or hydrothermal treatment may be required to fill the microscopic gaps (defects) between coated layers. There are several examples of the formation of inorganic membranes from layered materials. As-synthesized MCM-22 flakes was coated on α-alumina using LBL dip coatings followed by TEOS vaporizations, as shown in Figure 1-9a.[46] Because MCM-22 has a high aspect ratio morphology, the pore structures of coated MCM-22 layers aligned through *c*-orientation. TEOS vaporization was required to fill the gaps between MCM-22 flakes, and it allowed H_2/N_2 separation with high selectivity of 120. Flakes of exfoliated MCM-22 and layered MFI were deposited on porous supports using vacuum filtration as shown in Figure 1-9b.[79] The initial membranes coated by exfoliated flakes were not selective due to the presence of gaps between layers. To improve the separation properties, the coated membranes were processed with the secondary growth to fill the gaps with silicate crystals.

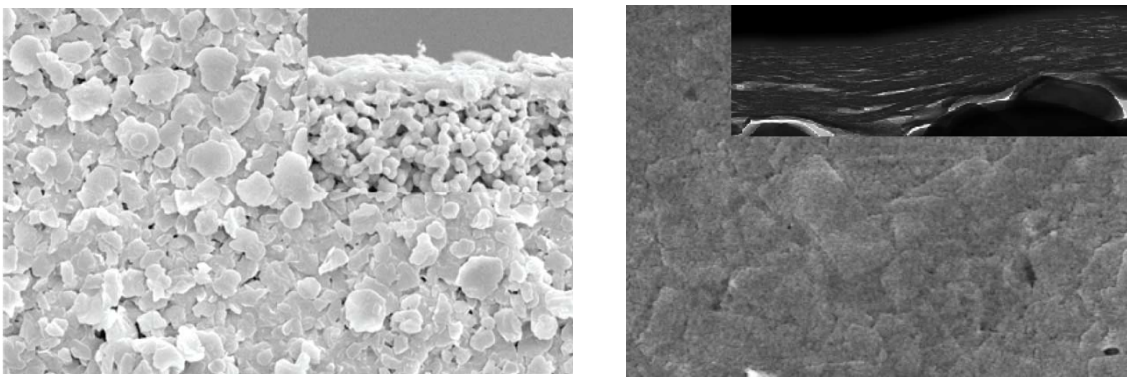

(a) (b)

Figure 1-9. Typical morphology of inorganic membranes fabricated by deposition of selective flakes.(a) MCM-22[46] (b) Exfoliated layered MFI[79] (inset of each figure shows the crossectional view)

Multilayer graphene membranes have been fabricated by spin/spray coatings of graphene oxide suspensions on copper substrates followed by etching using nitric acid.[83] Also, a prototype single-sheet porous graphene membrane has been fabricated by the combination of photolithography and mechanical exfoliation of graphene with a cellophane tape.[84] The following UV-oxidative etching introduced sub-nanometer pores in the graphene sheet.

1.3.3. Microstructural analysis of Nanocomposite Membranes

An important step after nanocomposite membrane fabrication is the microstructural analysis to determine its morphology. It should reveal the degree of exfoliation (partial or complete), dispersion quality of layered material in the polymer matrix, and the interface quality between the polymer and layered material. These characteristics are intimately connected to the separation performance of the nanocomposite membranes.[76,77]

Wide Angle X-ray Scattering (WAXS) can be used to determine the *d*-spacings of layered materials dispersed in polymers, and it can be a qualitative indication of the degree of exfoliation.[33] Also, the crystalinity of composite membrane can be determined by deconvolution of WAXS patterns to crystalline and amorphous phase. Crystalinity changes in the polymer matrix are related to the polymer chain packing and can lead to interesting separation properties.[85] However, the characteristic peaks seen in WAXS may depend strongly on measurement conditions such as scanning time, detector type etc. Misleading quantitative results can be obtained from WAXS patterns, and they should be considered as qualitative information.[33]

On the other hand, small angle X-ray and neutron scattering (SAXS/ SANS) can give detailed structural information. They have been widely used for analyzing the detailed microstructure and morphology of polymeric and composite materials. For example, SAXS analysis gave information on the structure of ionomers (size and orientation of water nanochannels) in Nafion® and sulfonated polyimides.[86,87] The structure and morphology of cellulose acetate membranes has also been studied by SANS, and the results have compared well to transmission electron microscopy (TEM) analysis.[88] Beyond these studies on revealing polymer morphology, SAXS/SANS analysis can give morphological information on polymer/inorganic composite materials. The slope of SAXS/SANS patterns in the lower momentum transfer (*Q)* regions can be a quantitative indication of the structural morphology of layered materials. Based on the Kratky-Porod model, the *Q*-dependence of single exfoliated layers is expected to have a

power law exponent of -2.[89] However, the completely exfoliated MMT/ PA66 composite (shown by TEM in inset of Figure 1-10a) has an exponent of -3 at low *Q* (Figure 1-10a), representing the presence of globular non-fractal clusters of exfoliated clay materials. The slope of -3.5 in Figure 1-10b is corresponding to the nanostructured domain of isolated multi-layer particles (10-100 nm size).

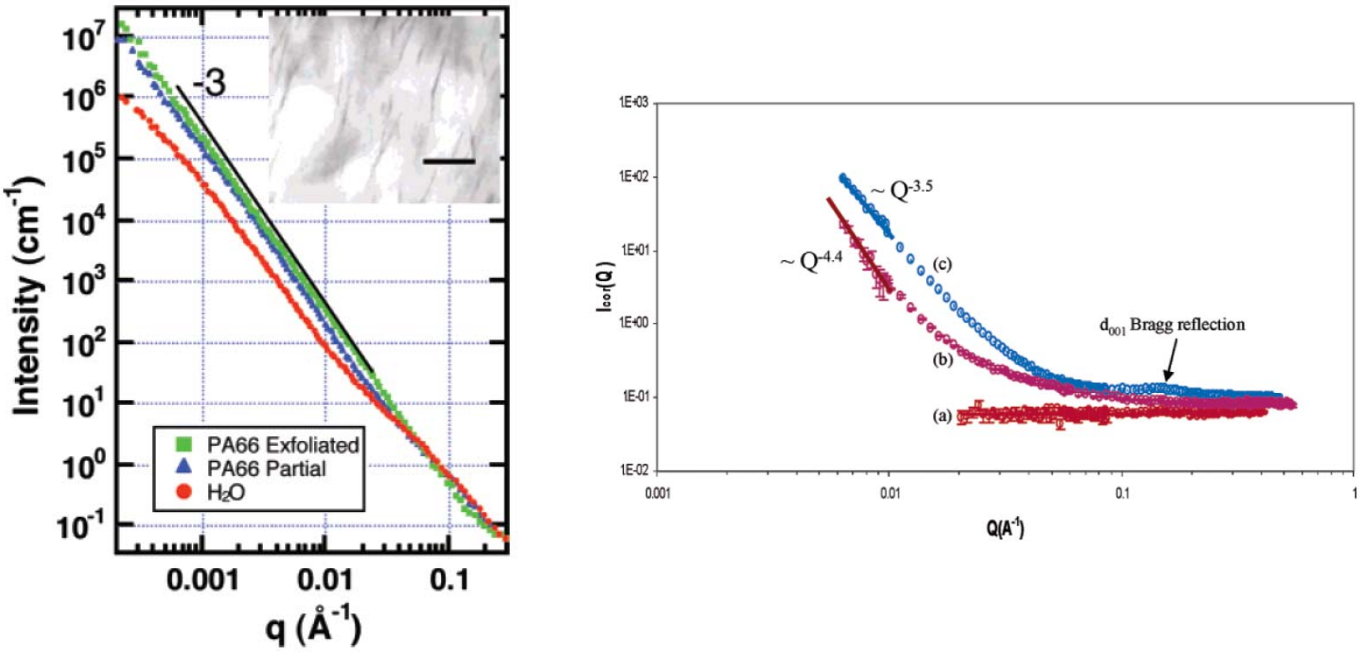

(a) (b)

Figure 1-10. SANS Analysis of (a) PA66/MMT composite materials[76] (b) polyamide/ layered AlPO composite materials.[25]

For detailed fitting simulations to obtain quantitative morphological information on polymer/inorganic composite materials, a variety of X-ray/neutron scattering model

equations have been developed based on the geometry of inorganic fillers (e.g., sphere, disk/layer, or rod).[89,90] The stacked-tactoid model is applicable to the present case of polymer/layered material composites.[91,92] The geometry of the stacked-tactoid model is illustrated in Figure 1-11a. The model equation consists of the form factor and structure factor. The form factor includes information on particle size and orientation, and the structure factor describes the internal structure of the stacks, such as the interlayer spacing and the average number (and Gaussian variance) of layers in the stacks. Figure 1-11b shows an example result of fitting simulations and the number of stacks in clay platelet has been calculated to 2. In the same way, the number of clay platelets stacked in nanocomposite membrane has been calculated properly.[93]

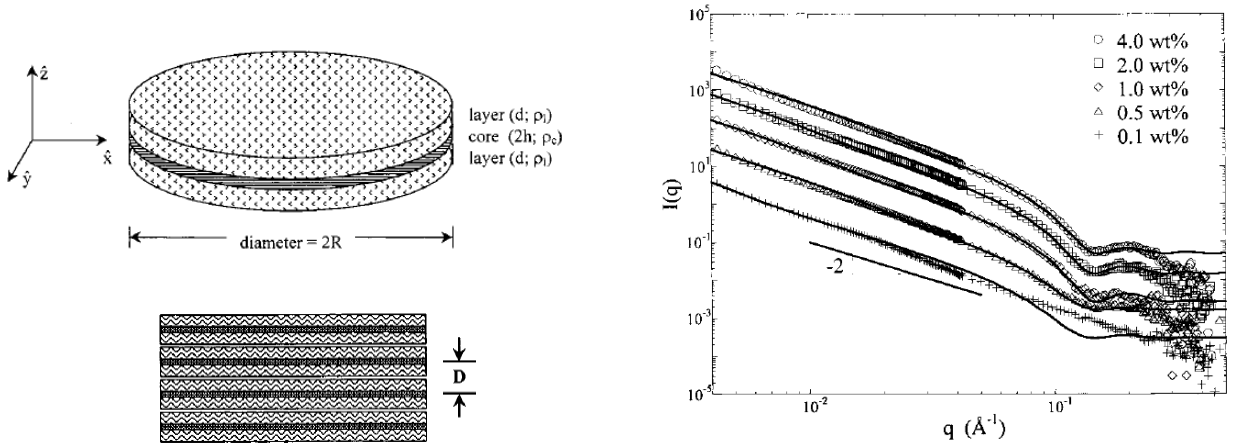

(a) (b)

Figure 1-11. (a) Schematics of Stacked Tactoid model (b) SANS fitting result to obtain the number of stack[91]

H^+-NMR can also be used to trace the degree of exfoliation and alignment of layered materials. Xu et al measured ^1H spin-lattice relaxation times of clay/ polypropylene composite materials and showed the evolution of clay morphology (exfoliation and alignment of montmorilonite) upon equibiaxial stretching of composite materials.[94]

HRTEM is also a viable method to examine the dispersion of layered materials in polymer matrix as shown in Figure 1-6c. Its main drawback is that it can only image very small portions of the sample at a time.[33] Hence, it should be combined with more macroscopic techniques like SAXS/SANS to develop a reliable picture of the nanocomposite structure. Such an approach is demonstrated in this thesis.

1.4. Applications

1.4.1. Gas separations

To rationalize the effect of layered materials in separation performance, Cussler et al. developed a theoretical model for the calculation of permeability and selectivity of gas molecules in polymer and selective-flake composite membranes.[95] And the applicability of the analytical model has been verified by Maxwell-stefan modelling for zeolite diffusion.[96,97]

The first gas separation application of polymer/selective flake composite membranes in molecular separation was reported for the case of porous layered AlPO/polyimide composite membranes.[25] The composite membrane showed substantial improvements on O_2 selectivity over N_2 attributed to the porous layered AlPO improved the overall gas separation performance as shown in Figure 1-12. Similarly, swollen AMH-3 had been incorporated in PBI and showed moderate improvements on overall CO_2/CH_4 selectivity by exploiting the molecular sieving effect of the AMH-3 pores.[98] The layered titanosilicate JDF-L1 has also been incorporated in a copolyimide and showed significant improvements in H_2/CH_4 separation utilizing its 3 Å pore openings.[27]

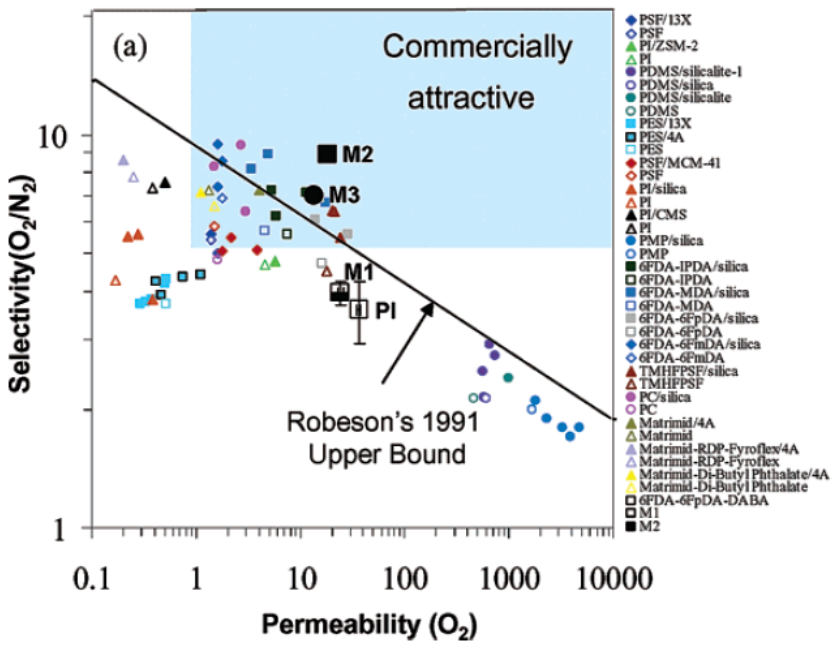

Figure 1-12. O_2/N_2 separation using AlPO/ polyamide composite membrane[25]

Inorganic membranes fabricated with layered zeolites have also been applied to various important separations. The *c*-oriented inorganic membrane film fabricated from MCM-22 flakes has been applied to H_2 separations utilizing its 6MR pore openings and showed significant improvements on H_2/N_2 selectivity.[46] The selective membrane fabricated by exfoliated MWW flakes showed highly improved selectivity in He/N_2 separation using its 6 MR pores, while exfoliated layered MFI has been applied to xylene separations utilizing its 10 MR pores.[79] The first experimental application of porous graphene in gas separation has been shown via a pressurized blister test.[84] Ultra-violet oxidative etching was used to introduce pores in fabricated non-porous graphene membranes. The deflection of the film surface due to gas pressure has been measured to

track the permeability. Porous graphene after etching process becomes H_2 and CO_2 selective by introduction of 3-4 Å pores as shown in Figure 1-13a and b.

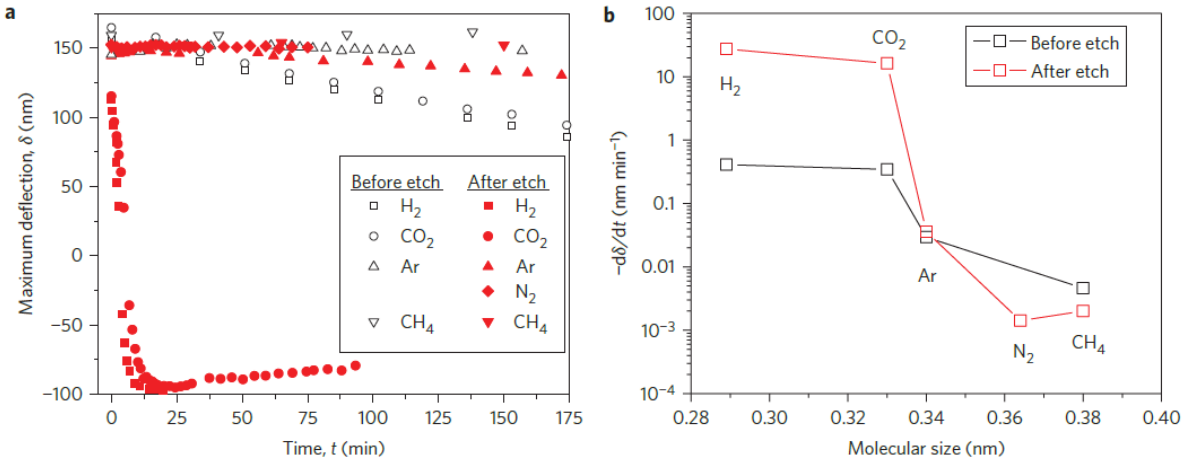

Figure 1-13. Comparison of leak rates of pristine and porous graphene membranes (a) Maximum deflection versus time before and after etching (b) Average-d/dt versus molecular size : It shows improved permeability of H_2 and CO_2 after etching.[84]

1.4.2. Liquid-phase Separations

Nair *et al* reported unimpeded permeation of water along the leak-tight graphene membranes.[83] The non-porous structure of graphene membrane shows significantly lower permeability for Helium gas than does PET (current commercial packaging material). A sub-micrometer graphene membrane showed higher He barrier properties than 1-mm-thick glass. However, water permeability of the graphene membrane is very high as shown in Figure 1-14a, and it allows 'unimpeded permeation of water'. This unusual separation property could be explained by the capillary effect of monolayer water molecules uptaken between graphene layers. Its effect has been demonstrated by atomistic simulations of water dynamics.

While graphene membranes are actively being developed, similar carbon-based membranes have been introduced and showed ultrafast viscous permeation of organic solvent.[99] Diamond-like carbon (DLC) nanosheets (10-40 nm thick) have been fabricated by plasma chemical vapor deposition and a highly cross-linked network of carbon atoms could lead to strong mechanical properties. The pore size (less than 1 nm) of the DLC membrane was used to perform organic solvent separation from bigger solute molecules. The ultrafast viscous permeation of organic solvent is shown in Figure 1-14b.

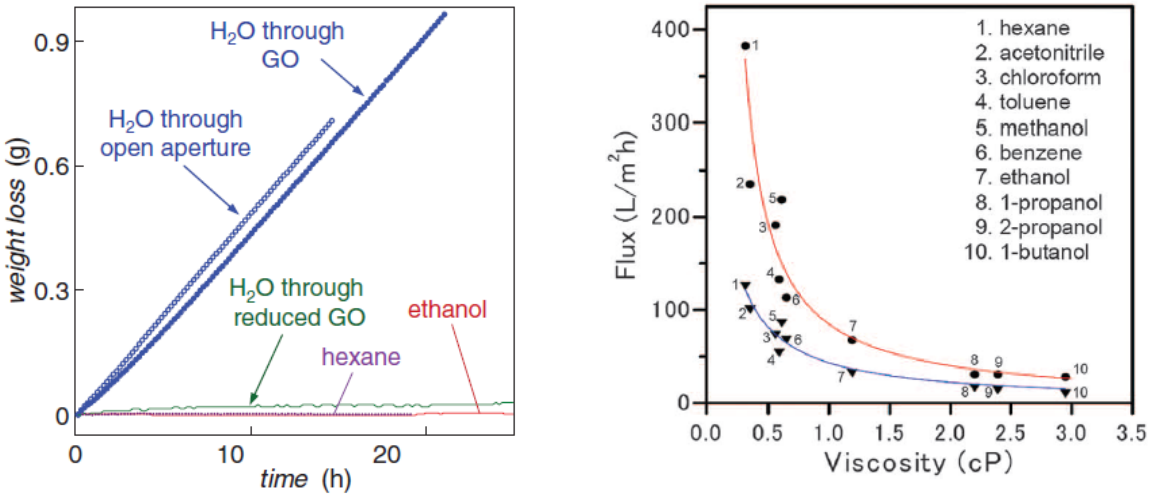

(a) (b)

Figure 1-14. The result on (a) Water permeation using graphene membrane (b) viscous permeation using DLC membranes (Red: Acetylene monomer; Blue: HMDS monomer)

While conventional carbon-based membranes produced by pyrolysis has large limitations due to their low permeability, higher cost, and fragility,[100] the above new developments on carbon membranes can be promising alternatives for the applications in

liquid-phase separations. Different mechanisms for molecular separations in these membranes have been illustrated by Paul as shown in Figure 1-15.[101]

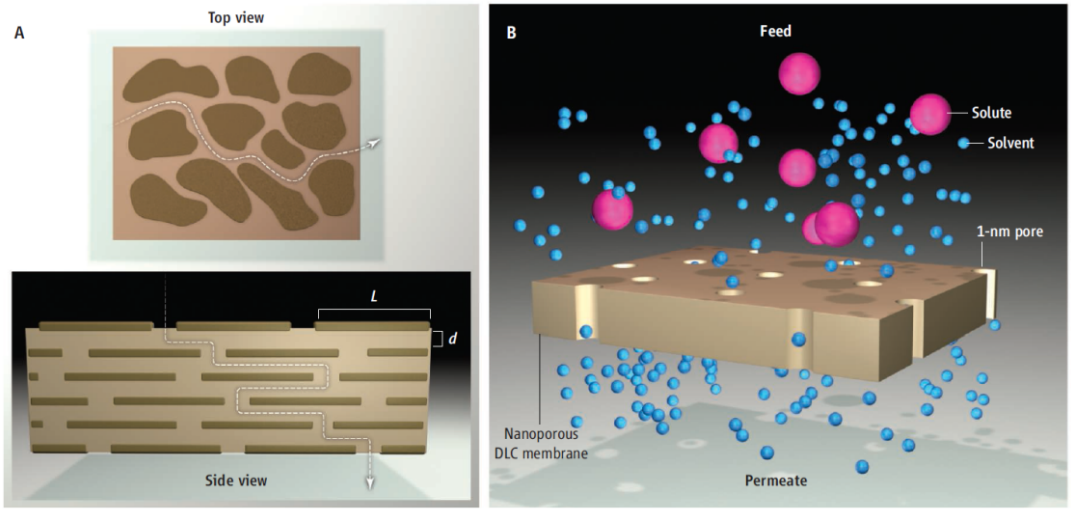

Figure 1-15. Schematics of transport mechanisms in (a) graphene membranes, and (b) DLC membranes.

1.4.3. Ion Transport Membranes

The active research on separation membranes utilizing porous layered materials has opportunities to be expanded to fuel cell membranes and related ion transport membranes. The major components of DMFC are the anode, cathode and the Proton Exchange Membrane (PEM). At the anode, methanol is oxidized and produces electrons, H^+ and CO_2 as a byproduct. The H^+ is transported through the PEM and reduced by oxygen to produce H_2O. The development of higher-performance PEMs is important to improve the overall fuel cell performance.[2] To be more specific, the requirements on the DMFC membrane are high H^+ conductivity and low methanol permeability (to prevent transport of the fuel through the PEM). The formation of water channels in PEMs is important for realizing

higher proton conductivity, but this also increases the methanol crossover as a side effect.

Several research groups have tried to incorporate (modified) clay materials in PEMs.[39,40,102] However, clays are non-porous layered materials and they act as barriers for both H^+ and methanol, resulting in large decreases of H^+ conductivity. Porous layered silicates can be alternative materials as they can permeate the protons through the sub-nanometer pore openings. For example, swollen AMH-3 flakes have been incorporated in Nafion® membranes by two groups, as summarized in Table 2.[103,104] Methanol permeability is significantly decreased while maintaining a high H^+ conductivity.

Table 1-2. Proton conductivity and Methanol permeability result utilizing AMH-3 flakes in Nafion® membrane.

	Hudiono et al[103]		**Kim et al[104]**	
	Nafion	**5% SAMH-3 composite membrane**	**Nafion115**	**Exfoliated AMH-3 coated membrane**
Proton condudtivity (S/cm)	7.5×10^{-2}	4.2×10^{-2}	4.09×10^{-2}	3.75×10^{-2}
Methanol Permeability (cm^2/s)	1.94×10^{-5}	0.57×10^{-5}	2.67×10^{-5}	1.7×10^{-5}
Selectivity ($S\ s/cm^3$)	3.86×10^4	7.37×10^4	1.53×10^4	2.21×10^4

1.5. Objectives and Aims of this Thesis

The overall objective of this thesis is to study and develop methods for fabricating new types of inorganic or nanocomposite membranes by utilizing high-aspect-ratio, thin, nanoporous flakes. This work includes detailed scientific investigations of the overall process, including the preparation of layered materials, chemical treatments of these materials, and the fabrication of membranes. The detailed research objectives and the scope of this thesis is as follows:

A. Effective chemical treatment methods for layered porous materials : Swelling and Functionalization methods for AMH-3 & MCM-22:

One important objective is to find an effective method to swell the interlayer space of AMH-3 while preserving the pore structure. Our approach is based upon the use of efficient swelling agents such as long-chain diamines, and optimizing the swelling process. ^{29}Si-NMR is used for the characterization of structural changes during the swelling process. Silane condensation reactions using octylmethyldimethoxysilane agent were investigated to functionalize AMH-3 and MCM-22 and improve their surface compatibility to hydrophobic polymer materials.

B. Active exfoliation process for the fabrication of polymer/ porous layered silicate composite membranes and microstructural analysis:

A major issue in the fabrication of membranes incorporating porous layered silicates is regarding how well the selective flakes can be exfoliated and dispersed

in polymer matrix. Our strategy for membrane fabrication is in the combination of active exfoliation processes with conventional solution blending methods for membrane casting. Swollen AMH-3/Cellulose Acetate nanocomposite membranes were fabricated and studied in detail. A high-shear mixing process using a high-speed mixer (operating at >7,000 rpm) was used to exfoliat the AMH-3 layers. Detailed microstructural analysis of the composite membranes are performed by SAXS and HRTEM techniques.

C. **Application of polymer/ porous layered silicate nanocomposite membranes to CO_2/CH_4 gas separations:**

Using a well exfoliated AMH-3/ polymer composite membrane, gas permeability and selectivity on CO_2/CH_4 separation are investigated. The results are compared to conventional models of transport in flake-contained membranes, and are used to hypothesize transport mechanisms occurring in the nanocomposite membrane system.

D. **Synthesis of novel hybrid layered materials by epitaxial growth**

The synthesis of "hybrid" zeolitic materials (containining two different morphologies in the same material or particle) is an expanding area of recent interest for a number of applications. We show the first example of synthesis of layered zeolites on the surface of conventional zeolites by epitaxial (i.e., lattice-matched) growth. In particular, we investigate the synthesis of layered MFI on different crystal surfaces of conventional MFI. The structure and morphology of

this new hybrid zeolite material is investigated and elucidated in detail via a combination of XRD, TEM, HRTEM, SEM, TGA, and N_2 physisorption methods.

E. Extending the synthesis of layered silicates to layered SAPO Materials: Small-pore Layered SAPO materials for gas separations.

Our objective is to adapt the synthesis methods for layered MFI to synthesize small-pore layered materials, which will expand its applications toward small-gas separations such as H_2 and CO_2/CH_4 separations. A small-pore 3D material is SAPO-34. We hypothesized that by design of an appropriate long-chain template, the synthesis of layered MFI can be extended to synthesize layered SAPO-34 (or another similar small-pore SAPO layered material). We describe in detail the deisgn and synthesis of the template, synthesis of a layered SAPO material, and characterization of its structure.

1.6. Potential Impact of this Work

A new generation of membrane architectures utilizing nanoporous layered materials is emerging in the literature. Because these materials can be processed as very thin separating layers (~100 nm) using both conventional and novel processing methods, they show substantial promise for use in high-performance separations applications. This high performance membrane can significantly reduce the energy consumption for molecular separations by replacing current thermally-driven separation methods such as distillation and gas absorption. Our work is significant in developing the science and technology of such materials and membranes. Our work on several layered materials

(AMH-3, Layered MFI, and MCM-22) enables the potential of layered silicate/polymer membranes for a fairly wide range of industrial separations (from light gases to hydrocarbon molecules). We have also expanded the scope of these materials to hybrid epitaxial materials with new morphologies, and to the synthesis of layered SAPO materials. The developments described in this thesis are expected to play a significant role in the emergence of membrane science and technology based upon porous layered oxide materials.

CHAPTER 2: SWELLING, FUNCTIONALIZATION, AND STRUCTURAL CHANGES OF THE NANOPOROUS LAYERED SILICATES AMH-3 AND MCM-22

2.1. Introduction

The assembly of crystalline inorganic nanoporous materials such as zeolites into thin films has attracted a great deal of interest in recent years, owing to their molecular sieving properties and potential function as highly selective separation membranes[10-12]. Despite their attractive molecular transport properties and a few commercialized applications such as alcohol dehydration, zeolite membranes are presently difficult to utilize in industry for gas separations. This is primarily due to the difficulties in economical synthesis of defect-free continuous zeolite membranes on a large scale. ó □ ó □ ó □ ó ing molecular sieving inorganic nanoporous particles in a polymeric membrane, can combine the advantages of polymers (such as processibility and lower cost) with those of inorganic materials, (such as high selectivity, throughput, and thermal stability)[14-18,105,106]. However, conventional "isotropic" inorganic molecular sieve particles require high loadings in composite membranes to increase the selectivity substantially. Also, it is challenging to scale down the membrane thickness to ~100 nm levels for high throughput.

Nanoporous layered materials can potentially overcome the above limitations of isotropic inorganic materials[25,28]. Such materials would retain the molecular sieving

characteristics of zeolites. Furthermore, the interlayer spaces can be swollen by the use of appropriate long-chain organic molecules, and the layers can subsequently be delaminated or exfoliated into 'flakes' of nanoscale thickness and a large aspect ratio[34-37]. A membrane containing such flakes could be scaled down to ~ 100 nm levels of thickness, as well as provide higher selectivity (at relatively low flake loading) for smaller molecules due to the highly tortuous permeation path for large molecules[95]. The layered silicate AMH-3[47] is an attractive candidate for preparing selective flakes, because it is the first 3-D porous layered silicate with 8-membered rings (8MRs) in all three principal crystallographic directions. The nominal 3.4 Å pores defined by the 8MRs in AMH-3 can be applied to various gas separations such as H_2/CO_2 and CO_2/CH_4. Choi *et al* reported a process for swelling of AMH-3 interlayer spaces, and the incorporation of swollen AMH-3 into polybenzimidazole (PBI), leading to an improvement in gas separation selectivity.[49,50,98] Hudiono *et al* incorporated swollen AMH-3 in Nafion® to fabricate membranes for direct methanol fuel cell (DMFC) applications, and showed decreased methanol permeability while maintaining significantly high proton conductivity[107]. The layered silicate MCM-22 has 2D 10MR pore channels in the plane of the layers, and 6MR openings perpendicular to the layers[42]. Corma *et al* reported the swelling and exfoliation of MCM-22 to obtain a new layered material (ITQ-2) with a high external surface area ($>700 m^2g^{-1}$)[43]. Other exfoliated materials such as ITQ-6 and ITQ-18 have been synthesized by changing the layer structure to that of the zeolites ferrierite and NU-6, respectively[44,45]. MCM-22 is also attractive for the fabrication of certain types of gas separation (e.g., H_2) membranes[108].

However, a number of challenges exist along the path to applying these materials in gas separation membranes. The swelling of AMH-3 interlayer spaces is considerably more difficult than for conventional layered materials (such as clays), due to the existence of strongly bound Na^+ and Sr^{2+} cations between the layers. Choi *et al* demonstrated a sequential intercalation method for swelling of AMH-3[50]. However, they reported that the pore structure of AMH-3 was altered and disordered to a significant extent during the swelling process[49]. A second important challenge is that of making the layer surfaces of swollen AMH-3 and MCM-22 materials compatible with hydrophobic polymers that are used in the fabrication of gas separation membranes. Surface incompatibility problems between layered clay materials and polymers have been addressed by several methods, such as direct synthesis of inorganic-organic composites by sol-gel processes[109,110] and introduction of long-chain quaternary ammonium surfactants between the layers[37,111]. The grafting of organosilanes on clay and Kanemite/ Magadiite surfaces has also been studied[112-115]. The modified materials produced by the latter covalent functionalization method have greater chemical stability, and additional surface modifications are possible by incorporating reactive end groups on the grafted organosilane. However, the extension of these methods to nanoporous layered silicates is non-trivial and has not been explored.

In this chapter of thesis, we investigate in detail the related issues of interlayer swelling, structural changes, and layer surface modification. We first describe a modified swelling method using diamine swelling agents that preserve the pore structure of AMH-3 to a greater extent during the swelling process. We then demonstrate a method for organic functionalization of AMH-3 and MCM-22 layer surfaces *via* siloxane

condensation reactions. These processes, and the structures of the resulting swollen and organic-functionalized materials, are characterized in detail by a combination of techniques.

2.2. Experimental Methods

2.2.1. Synthesis of AMH-3 and MCM-22(P)

Hydrothermal synthesis was performed for 3 days at 200°C to prepare AMH-3 crystals[50]. The molar composition of the reactant gel was 1 TiO_2 : 10 SiO_2: 2 $SrCl_2$: 14 NaOH : 675 H_2O. To prepare the reactant gel, 1.38 g of sodium hydroxide (Aldrich) was dissolved in 55.85 g of DI water, and 2.94 g of strontium chloride (99%, Aldrich) was added followed by 30 minutes of stirring at 80°C. Then, 12.52 g of sodium silicate (26.5% SiO_2, Aldrich) as a silica source was added. After 30 minutes of stirring, 4.25g of titanium chloride (Fisher Scientific, 20%, HCl stabilized) was added and mixed for another 1 hour. The prepared gel was poured into a 45ml Teflon lined autoclave, and the reaction was carried out under 60 rpm rotation and a temperature of 200 °C. MCM-22(P) was prepared by 11 days of hydrothermal synthesis at 130°C, as described in previous works[43]. To prepare the reactant gel, 0.36 g of sodium aluminate (MP Biomedicals, USA) and 1.24 g of Sodium hydroxide (Aldrich) were dissolved in 155.5 g of DI H_2O. Then, 9.55 g of Hexamethylenimine(HMI) (Aldrich) and 11.8 g of fumed silica (Cab-o-sil M5®) were added to the mixture. The mixture was allowed to stir for 6hrs before transferring to 45ml Teflon lined autoclave to start synthesis.

2.2.2. Swelling of AMH-3 and MCM-22(P)

The sequential intercalation method reported by Choi *et al*[50] was taken as a starting point for the swelling of AMH-3. Typically, 0.776 g of DL-histidine (≥99%, Aldrich) was dissolved in 25 ml of DI H_2O at 60°C until it became transparent. Then the solution was cooled down to room temperature while stirring it. The pH value of the buffer solution for H^+-exchange was controlled to 6.0 by adding several drops of concentrated hydrochloric acid. Then 0.2 g of as-made AMH-3 was added to start H^+-exchange. The swelling agent solution was prepared by dissolving 2.061 g of dodecylamine (Aldrich) or 2.228 g of dodecyldiamine (Aldrich) in 50 ml of DI H_2O at 60°C followed by stirring for 30 min. After 1 hr from the starting of the proton exchange step, the swelling agent solution was added drop-wise. After 12 hr of swelling, the swollen AMH-3 product was obtained and purified by three cycles of washing with DI water and centrifugation. The swelling procedure for MCM-22 is reported in the previous works[108]. Typically, 1.8 g of MCM-22 (P) was added to 7.2 g of DI H_2O then mixed to 29 wt % CTAB aqueous solution including 10.15 g of CTAB (Aldrich) and 24.85 g of DI H_2O. Then 11 g of TPAOH (Alfa Aesar, 40%) was added to the reactant followed by room temperature swelling reaction for 16 hrs. The swollen MCM-22 product was recovered by repeated cycles (typically ~10) of washing with DI H_2O and centrifugation.

2.2.3. Functionalization of AMH-3 and MCM-22

A step-wise functionalization method for AMH-3 and MCM-22 was developed to covalently functionalize the surface with hydrocarbon groups. A 0.2 g quantity of swollen AMH-3 or swollen MCM-22 was dried in a vacuum oven for 12 hrs at 150 °C. The dried

powder was added to a mixture of 4 g anhydrous toluene (Aldrich) and 0.4 g octyl(methyl)dimethoxysilane (Aldrich) in a glove box to prevent contamination by H_2O. The functionalization reaction was then carried out under reflux conditions at 110 °C for 16 hrs.

2.2.4. Characterization Methods

Scanning Electron Microscopy (SEM) images were obtained with a JEOL LEO-1530 SEM at a landing energy of 10 kV using the 'In Lens' mode detector. Transmission electron microscopy (TEM) images were taken with a Hitachi HF-2000 TEM operating at 200 kV accelerating voltage. The samples were prepared for TEM by dispersing the material in epoxy resin and then microtoming slices of 80-100 nm thickness using a diamond knife. Powder XRD patterns were obtained with a PAnalytical Xpert Pro diffractometer operating with a Cu source (λ=1.5418Å) and an RTMS detector. For accurate measurements at low diffraction angles, a narrow divergence slit (1/32°) and anti-scattering slit (1/16°) were used. Solid state ^{29}Si-NMR spectra were obtained with a Bruker AV3-400 spectrometer operating at 400 MHz, and with a 10 kHz spinning frequency. Samples were prepared in a 4 mm ZrO_2 rotor. For ^{29}Si-NMR, high-power proton decoupling (DP-NMR) was measured with a 45° pulse of 1 μs duration and 10 s recycle delay. For ^{13}C-NMR, cross polarization (CP-NMR) was measured with a 45° pulse of 5 μs duration and 4 s recycle delay. FT-IR spectra were measured with a Bruker Equinox 55, at a resolution of 8 cm^{-1} and 256 scans. Samples were prepared with a high-pressure pelletizer, and a KBr pellet was used as background sample. Thermogravimetric analysis (TGA) and DSC were performed with a Netzsch STA409. Temperature was

scanned from 30°C to 900°C with a ramping rate of 10°C/min. N_2 and O_2 purging flow rates were 90 ml/min and 50 ml/min, respectively. N_2 physisorption isotherms and BET surface areas were measured with a Micrometritics® Tristar II. Samples were degassed *in situ* at 150°C for 12 hrs before the measurement. Water sorption isotherms were obtained with an IGASorp instrument. Powders were degassed *in situ* at 100°C for 5 hrs.

2.3. Results and Discussion

2.3.1. Swelling of AMH-3

A sequential intercalation method was used for the swelling of AMH-3[50]. The first step of this method is a proton exchange using an amino acid. Specifically, DL-histidine was used as a buffer to provide protons while preventing abrupt changes of pH during the proton exchange step. The second step is the intercalation of the AMH-3 layers by a primary amine. This step involves hydrogen bond formation between hydroxyl groups on the AMH-3 layer surface and the primary amine. An "optimal time" is necessary to begin the intercalation step. If the swelling agent is added before the optimum point, then sufficient exchange of the metal cations with protons would not have occurred and intercalation therefore does not occur. If the addition of the swelling agent is too late, complete proton exchange of AMH-3 occurs, leading to interlayer condensation and collapse of the AMH-3 layered structure. In this work, the optimum time for accomplishing H^+ exchange and thereafter introducing the swelling agent was found to be 1 hr. Intercalation of AMH-3 was investigated using a diamine (dodecyl-diamine), as well as the monoamine (dodecylamine) used in a previous work[50].

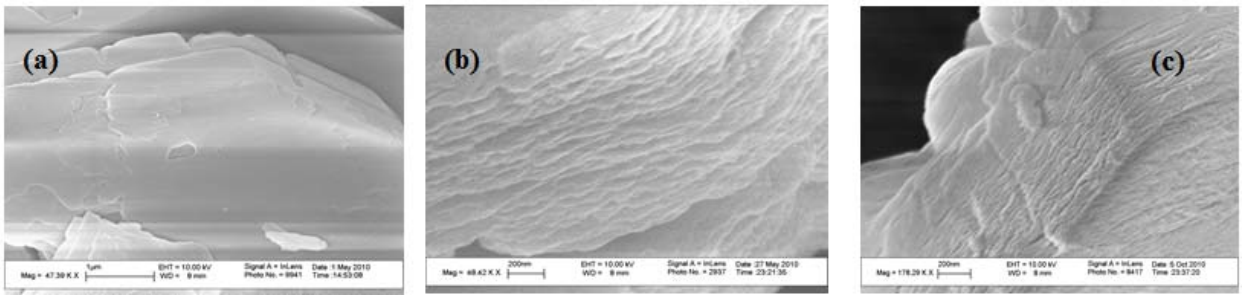

Figure 2-1. Morphologies of (a) as-synthesized AMH-3, (b) dodecyl-diamine Swollen AMH-3 (DD-SAMH-3), and (c) dodecyl-amine Swollen AMH-3 (DA-SAMH-3).

Figure 2-1 shows SEM images of as-made (synthesized) AMH-3, dodecyl-diamine swollen AMH-3 (DD-SAMH-3), and dodecyl-amine swollen AMH-3 (DA-SAMH-3). A roughened, layered morphology of both the DD-SAMH3 and DA-SAMH-3 materials was observed due to the intercalation by the primary amines between layers.

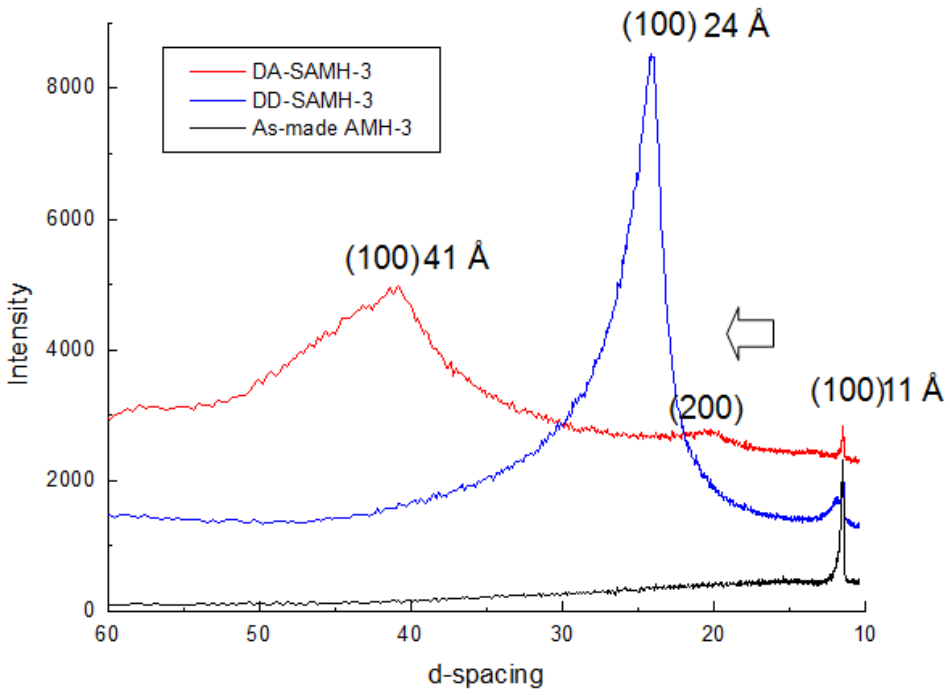

Figure 2-2. XRD patterns of as-made AMH-3, DD-SAMH-3, and DA-SAMH-3

Figure 2-2 shows the XRD patterns of the three materials. The intensity of the (100) peak in DD-SAMH-3 is much more well-defined than in DA-SAMH-3. The use of a diamine intercalating agent has the effect of producing a more ordered swollen material with a narrower distribution of interlayer spacings. The (100) peak represents the interlayer spacing, which is initially 11 Å in as-synthesized AMH-3 and increases to 24 Å and 41 Å for DD- and DA-SAMH-3 respectively. The TEM images in Figure 2-3 also corroborate the 24 Å and 41 Å interlayer spacings for DD-SAMH-3 and DA-SAMH-3, respectively. The interlayer spacing of 41 Å in DA-SAMH-3 is also consistent with previous work, and is due to the existence of bilayers of the swelling agent between the AMH-3 layers.[50] Considering the carbon chain length of C_{12} (~15 Å) and the thickness of

an AMH-3 layer (~10 Å), the observed interlayer spacing 24 Å in DD-SAMH-3 is consistent with a single layer of dodecyl-diamine molecules between the AMH-3 layers. The two amine groups on opposite ends of the molecule are expected to bind to adjacent AMH-3 layers. Scheme 2-1 summarizes the arrangements of the intercalating molecules in the two swollen materials.

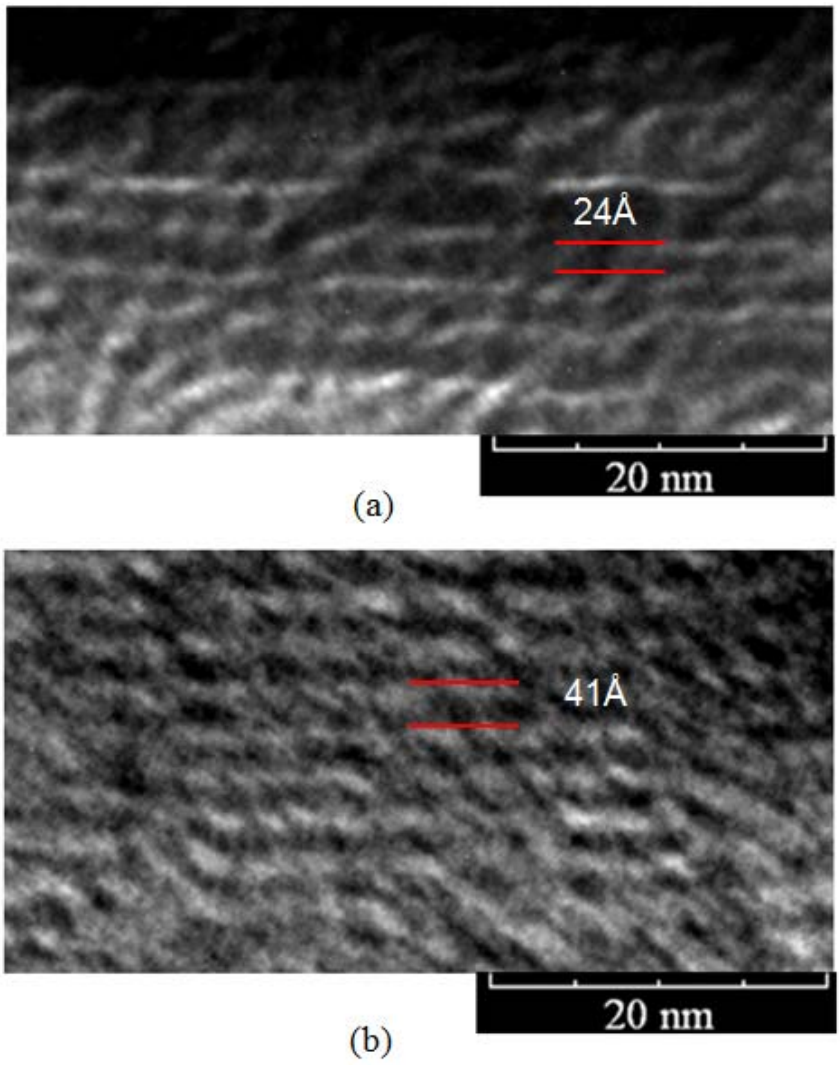

Figure 2-3. TEM images of (a) DD-SAMH-3 and (b) DA-SAMH-3.

Scheme 2-1. Arrangements of intercalating molecules in DD-AMH-3 (left) and DA-AMH-3 (right)

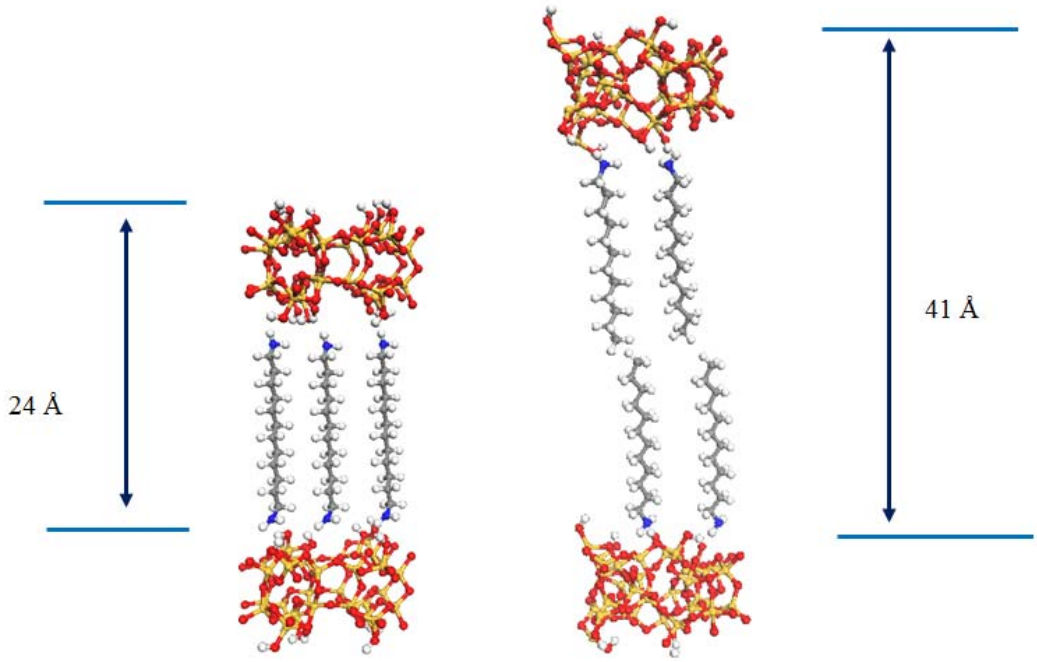

Figure 2-4 shows ^{1}H-NMR and ^{13}C-NMR spectra from the as-synthesized and swollen AMH-3 materials to analyze the presence of swelling agent between AMH-3 layers. In the ^{1}H-NMR spectrum, the chemical shift at 5 ppm is assigned to water and hydroxyl groups and -1 ppm is assigned to the protons in the hydrocarbon chains. The ^{1}H-NMR spectra show that the amount of water and hydroxyl groups in AMH-3 increased significantly during the proton exchange step, since Na^{+}, Sr^{2+} cations were exchanged to protons and hydroxyl groups have been formed by protonating the siloxy ($Si\text{-}O^{-}$) groups lining the AMH-3 layers. Comparing the ^{1}H-NMR spectra of DD-SAMH-3 and DA-SAMH-3, it is seen that the relative peak intensity of the hydrocarbon chains over hydroxyl groups in DD-SAMH-3 is smaller than that in DA-SAMH-3, because of

the smaller amount of swelling agent required for the preparation of DD-AMH-3 (also see TGA results later in this report). The ^{13}C-NMR spectra show chemical shifts characteristic of the two swelling agents. The chemical shift at 41 ppm is assigned to the carbon atom adjacent to the primary amine, and the peak at 30 ppm is assigned to the hydrocarbon chain. As expected, the relative intensity of the 41 ppm peak over the 30 ppm peak is higher in DD-AMH-3, because of the presence of two primary amine groups in one molecule.

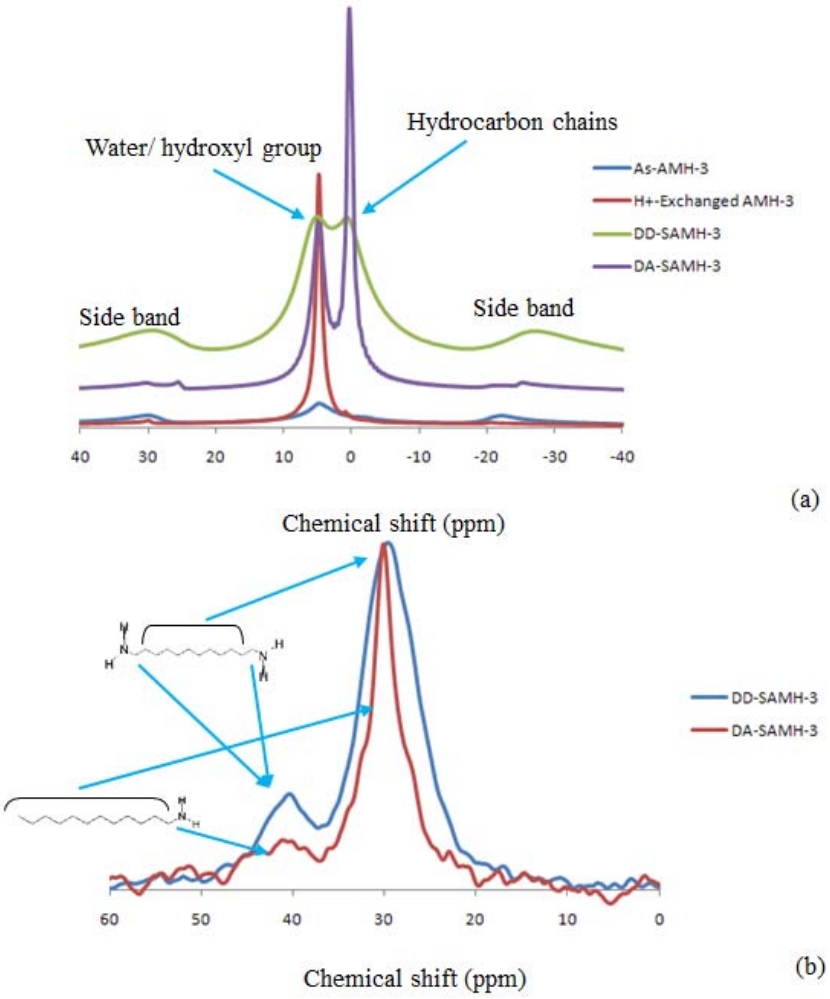

Figure 2-4. (a) ^{1}H-NMR and (b) ^{13}C-NMR spectra for as-made AMH-3, H^{+}-exchanged AMH-3, DD-SAMH-3, and DA-SAMH-3.

Figure 2-5 shows N_2 physisorption isotherms for as-made AMH-3, DA-SAMH-3 and DD-SAMH-3. Both the swollen materials show significantly higher BET surface areas than as-made AMH-3, as well as more prominent hysteresis, reflecting the interlayer mesoporosity caused by intercalation of long-chain amine and diamine molecules. However, DD-SAMH-3 shows a smaller estimated BET surface area than DA-SAMH-3, since it has a smaller interlayer spacing and the diamine molecules are bound more strongly to the AMH-3 surfaces *via* hydrogen bonds to two adjacent layers. The latter fact also prevents the extraction/evaporation of the interlayer amines (as occurs in the case of DA-SAMH-3) during degassing at 150°C before the start of the N_2 physisorption isotherm measurement.[49]

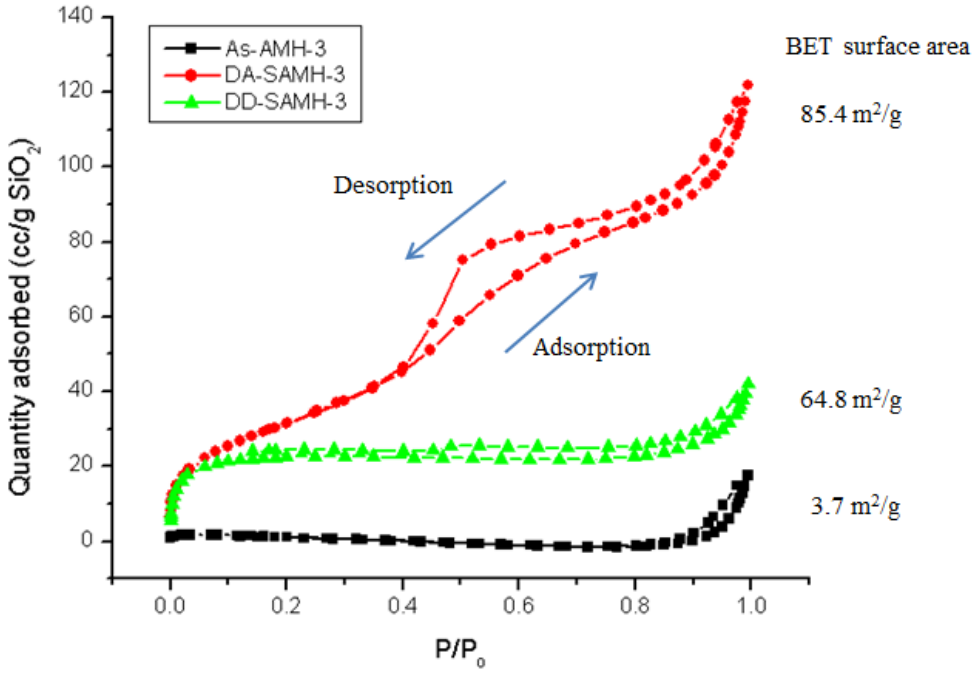

Figure 2-5. N_2 physisorption isotherms for as-made AMH-3, DA-SAMH-3, and DD-SAMH-3.

The two swelling agents also cause significant changes in the structure of the AMH-3 layers. Figure 2-6 shows FT-IR spectra of the as-made and intercalated materials. The analysis of the FT-IR spectrum of DA-SAMH-3 was carried out in a previous work[50]. The absorption bands between 3700-3400 cm^{-1}, 3000-2700 cm^{-1}, and 1300-400 cm^{-1} represent different types of interlayer water, the organic swelling agent, and silicate bands respectively. In Figure 2-6a, the water bands disappear after the swelling step, and only a broad, weak hydroxyl band remains. The organic swelling agent bands are presented after swelling, with the characteristic signatures of the hydrocarbon chains of the diamine and amine molecules. The DA-SAMH-3 and DD-SAMH-3 materials also did not show the "hydroxyl dimer" peak at 3440 cm^{-1}, which originates from the close proximity of hydroxyl groups from adjacent silicate layers. The Q3:Q4 ratio of the silicate layer in swollen AMH-3 is also in good agreement with the simulated structure after intralayer tetrahedral inversion,[49] further corroborating the lack of significant interlayer condensation. In the silicate bond region at Figure 2-6b, the bands representing vibrations of Q^3 silicon atoms (around 1100 cm^{-1}) are broadened for both of the DD-SAMH-3 and DA-SAMH-3. Also, bands representing fully condensed (Q^4) silicon vibrations (around 1250 cm^{-1}) became stronger, reflecting the occurrence of intralayer condensation within the individual layers. The broadening and disappearance of silicate "framework" bands in the 700-500 cm^{-1} region represent significant structural disorder occurring during swelling process.

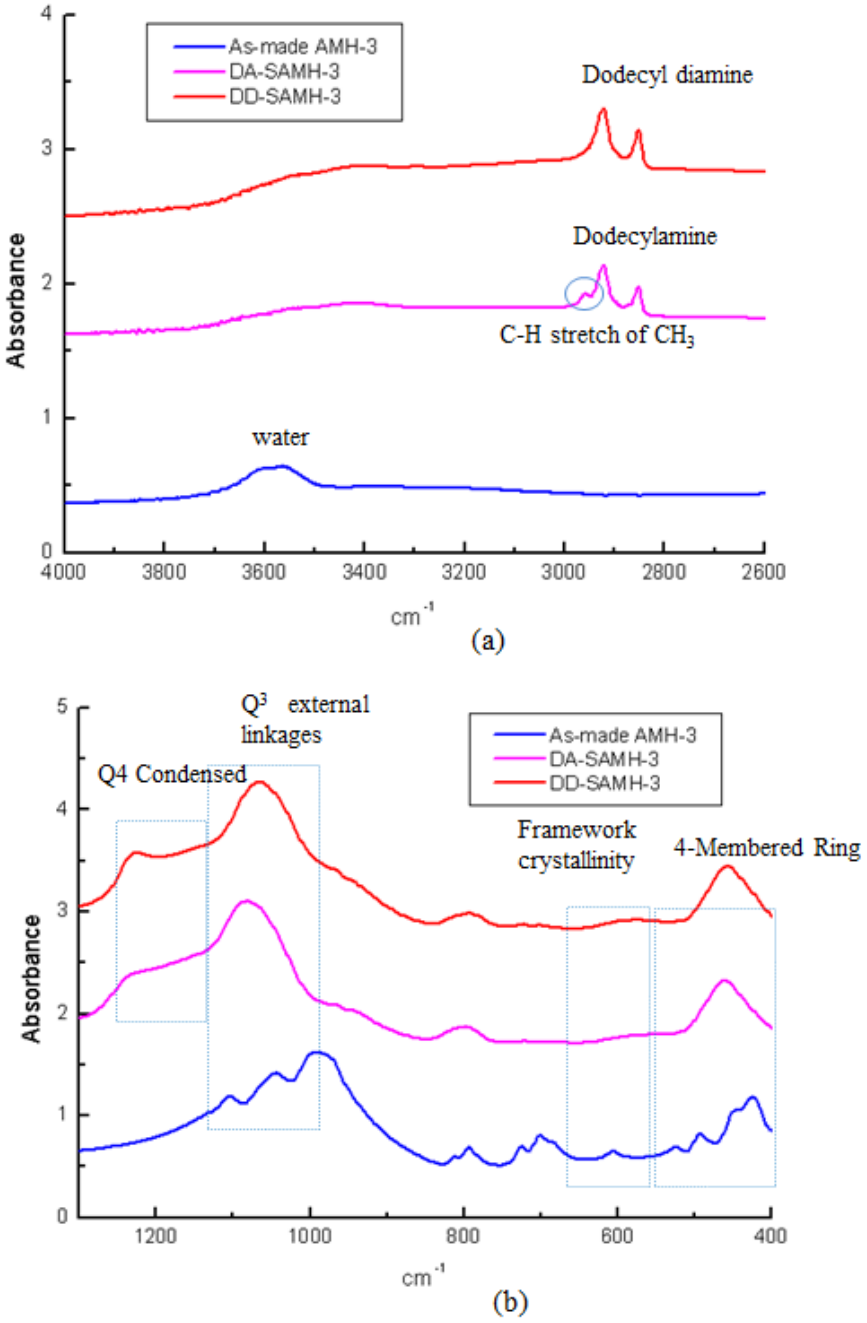

Figure 2-6. FT-IR spectra of as-made and swollen AMH-3 materials.

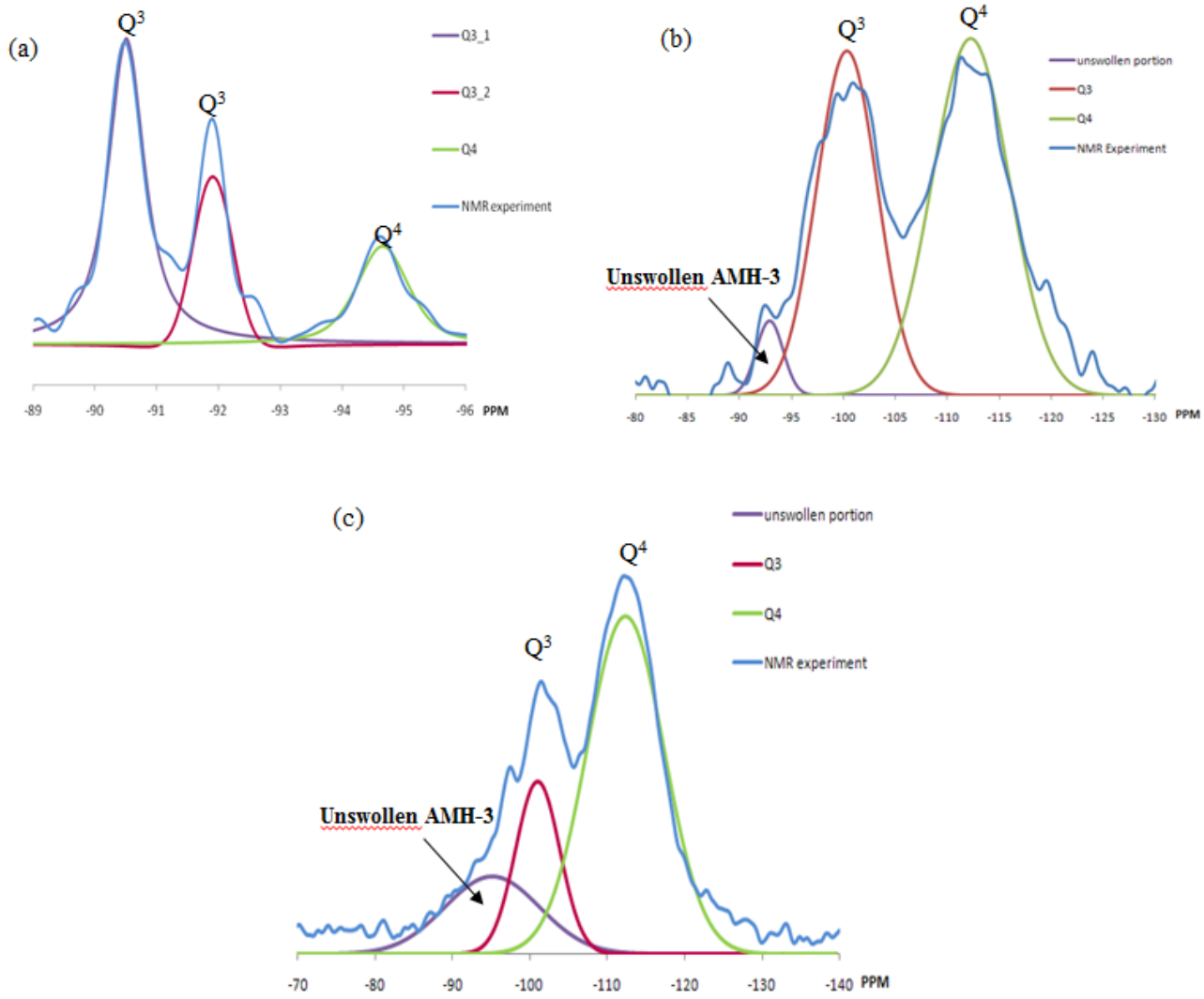

Figure 2-7. ^{29}Si-NMR spectrum of (a) as-made AMH-3, (b) DD-SAMH-3, and (c) DA-SAMH-3.

Structural changes of AMH-3 during swelling step occur by inversion (rotation) of the Q^3 SiO_4 tetrahedra, followed by intralayer condensation of these tetrahedra with each other.[49] Therefore, the structure of swollen AMH-3 can be approximately determined by measuring the Q^3: Q^4 silicon ratio after the swelling process. Figure 2-7

shows ^{29}Si MAS NMR spectra of as-made AMH-3, DD-SAMH-3 and DA-SAMH-3. The NMR spectra were deconvoluted to Gaussian curves using FITYK® curve fitting program. The Q^3:Q^4 ratio (calculated by the ratio of integrated intensities for these peaks) changed from 3:1 for the as-made AMH-3, to 1:1 and 1:3 for DD-SAMH-3 and DA-SAMH-3, respectively. The unswollen portion of AMH-3 was calculated to be 4 % in DD-SAMH-3 and 18 % in DA-SAMH-3. The relatively small amount of partially unswollen AMH-3 in the DD-SAMH-3 sample also indicates improved uniformity of swelling due to the use of dodecyldiamine as a swelling agent.

Figure 2-8 shows molecular models of the layers of as-made AMH-3 and the two swollen materials. The latter two models are obtained by starting from the model of as-made AMH-3 and performing tetrahedral inversion and intralayer condensation, to obtain Q^3:Q^4 ratios corresponding with those obtained from ^{29}Si-NMR measurements[49]. Forcefield-based energy minimization techniques incorporated in the Materials Studio molecular modeling package (Accelrys, Inc.) were used to produce physically realistic models[49]. Comparing these probable structures of the two swollen materials in Figure 2-8, we conclude that the DD-SAMH-3 maintains a more ordered pore structure in the AMH-3 layers, whereas the structure of DA-AMH-3 involves a substantial change in the pore size and shape accompanied by a larger degree of disorder. The structure of DD-SAMH-3 shown in Figure 2-8b is the result of intralayer condensation of 1 out of every 3 Q^3 silicate tetrahedra after tetrahedral inversion, whereas it was previously shown that the DA-SAMH-3 structure in Figure 2-8c is obtained by the intralayer condensation of 2 out of every 3 Q^3 silicate tetrahedra[49]. From these molecular models, the average pore size of

the original AMH-3 was calculated to 3.4±0.2 Å, and decreased to 2.8±0.4 Å in DA-SAMH-3, whereas DD-SAMH-3 showed an increased pore size of 4.1±0.4 Å. The increased pore size of DD-SAMH-3 is possibly due to an alignment of 4-membered silicate rings during intralayer condensation of certain silicate tetrahedra. Control of pore structure and disorder in AMH-3 (and other layered porous materials) during the swelling process is a challenging issue, and it appears that the problem can be addressed by selecting an appropriate swelling agent.

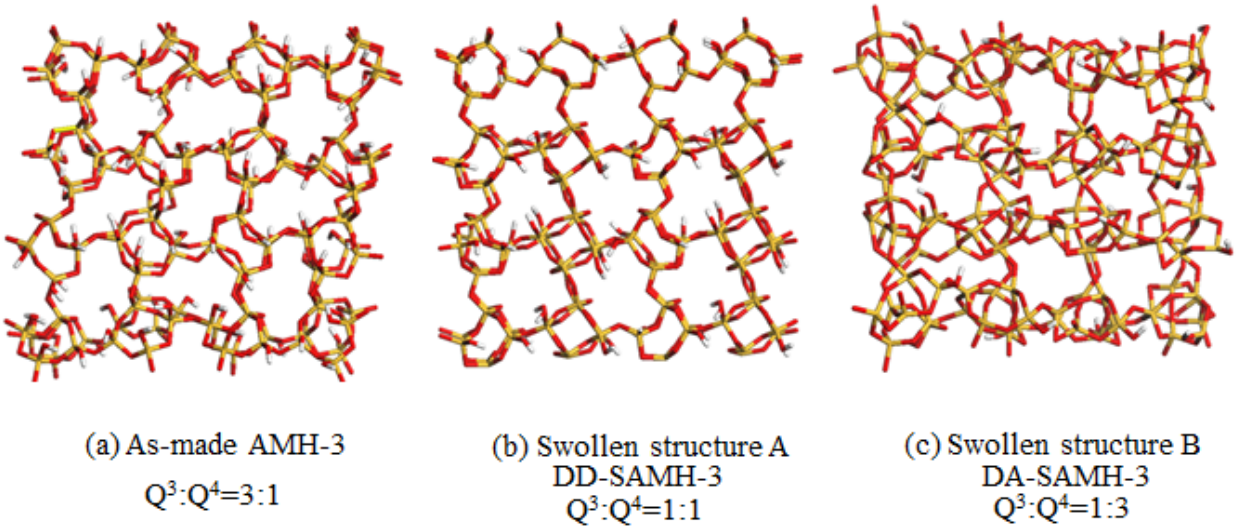

Figure 2-8. Simulated structural changes in AMH-3 during the swelling process. (The figures show top views of a single layer of AMH-3.)

Figure 2-9 shows TGA traces for the three AMH-3 materials. As-made AMH-3 shows about 9 % weight loss between 200-350°C, due to the desorption of strongly-bound water molecules from their binding sites in and between the porous layers[50]. In the swollen materials, the initial mass loss up to 100°C is from residual solvent, and the mass loss in the 110°C-550°C region is due to decomposition of the swelling agent. DD-

SAMH-3 and DA-SAMH-3 contain 13 wt % and 18 wt % of swelling agent respectively. The maximum loading of swelling agent was estimated from the chemical formula of the AMH-3 unit cell ($Na_8Sr_8Si_{32}O_{76}\cdot 16H_2O$) and the surface density of hydroxyl groups. The calculated maximum organic loadings are 44 wt % for DD-SAMH-3 and 43 wt % DA-SAMH-3. Hence, we can estimate that 31% and 52% of the hydroxyl groups in DD-AMH-3 and DA-AMH-3 participate in hydrogen bonding with the swelling agent.

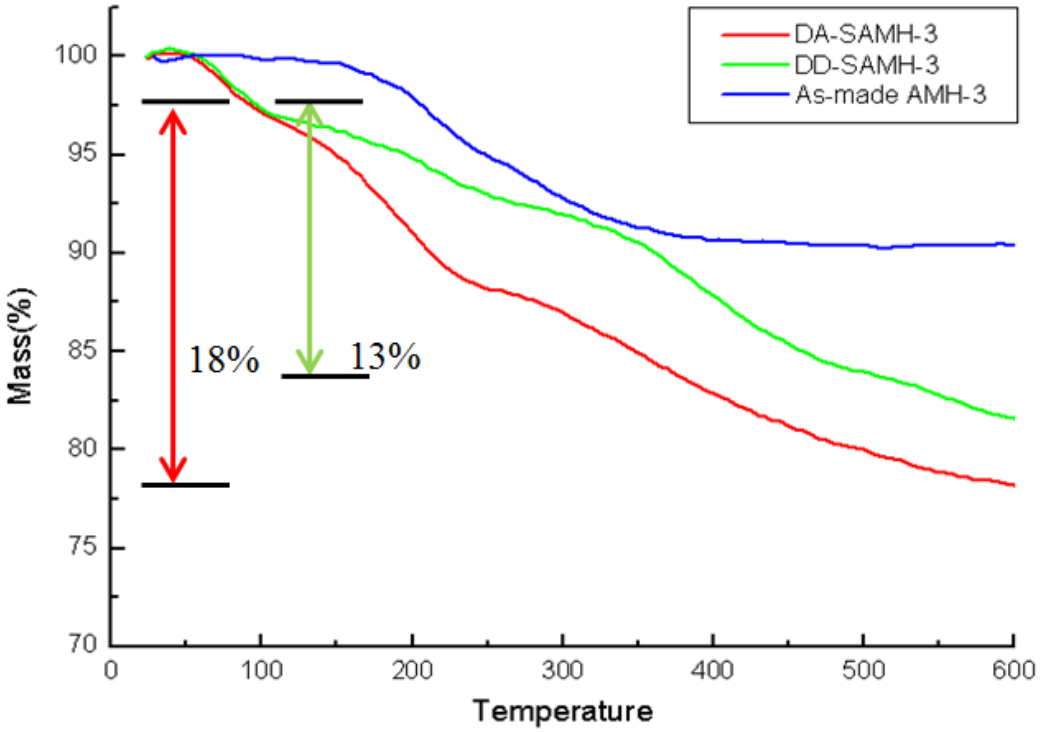

Figure 2-9. TGA traces for as-made and swollen AMH-3 materials.

2.3.2. Functionalization of AMH-3 Layer Surfaces

Next, we investigated techniques for covalent functionalization of the AMH-3 layer surfaces, which may allow better compatibility between the AMH-3 layers and

polymeric matrix materials. The first method explored was a sequential intercalation and functionalization route using alkoxysilane reagents. ^{29}Si-NMR, ^{13}C-NMR, and XRD analysis indicated surface-attached alkoxysilane groups. However, this route was hindered by the formation of self-condensed polysiloxane byproducts between layers. Thereafter, another technique, namely a "step-wise functionalization", was developed. Scheme 2-2 shows the hypothesized mechanism of this process. DA-SAMH-3 was selected as a starting material. The method includes a functionalization step and an extraction step. In the first step, octyl(methyl)dimethoxysilane as a functionalization agent is condensed with the available hydroxyl groups on the AMH-3 layer surface that were previously produced in the proton exchange step. Then, the dodecylamine swelling agent is extracted using a 1N HCl/EtOH solution. Depending on the positions of available hydroxyl groups and steric hindrance during the transport of the functionalization agent, alkoxysilane molecules are expected to be attached to the layers in both D^1 and D^2 forms.

Scheme 2-2. Hypothesized mechanism for functionalization of AMH-3 Layer Surfaces

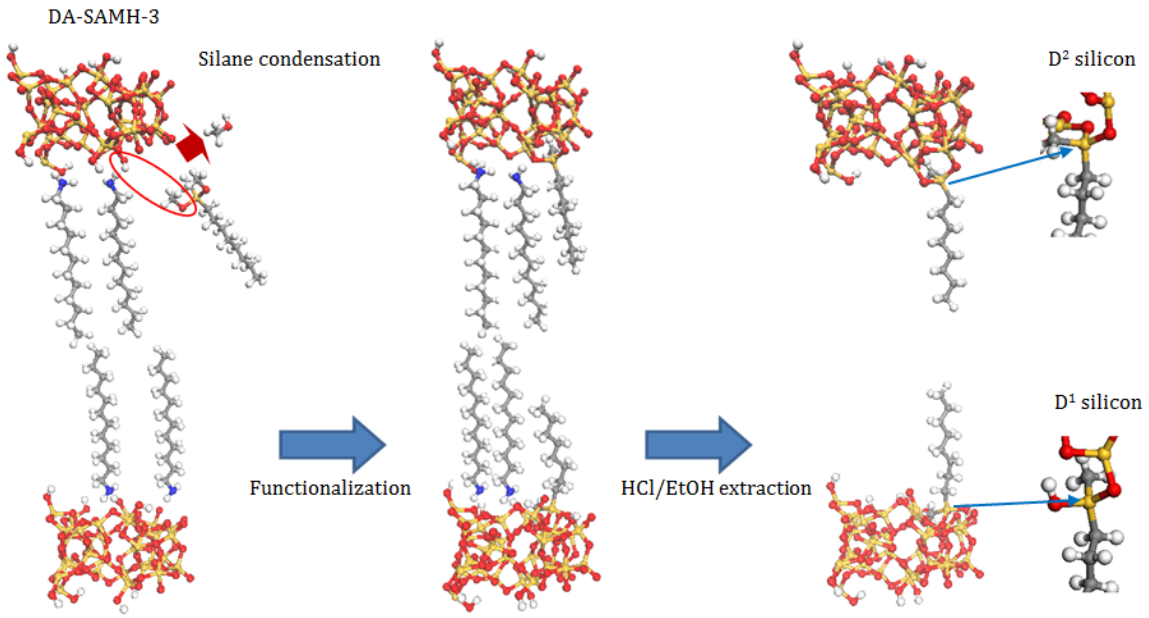

Figure 2-10 shows ^{29}Si-NMR and ^{13}C-NMR spectra of AMH-3 after completion of the step-wise functionalization process. The ^{29}Si-NMR showed both D^1 and D^2 silane attachments on the AMH-3 surface. The ^{13}C-NMR spectrum was also successfully assigned to the carbon atoms of the surface-attached functionalization agent. Water sorption experiments were performed to characterize the hydrophilicity changes in AMH-3 after functionalization. In Figure 2-11, the water sorption loading of DA-SAMH-3 is seen to decrease after the functionalization reaction, due to the presence of hydrocarbon chains.

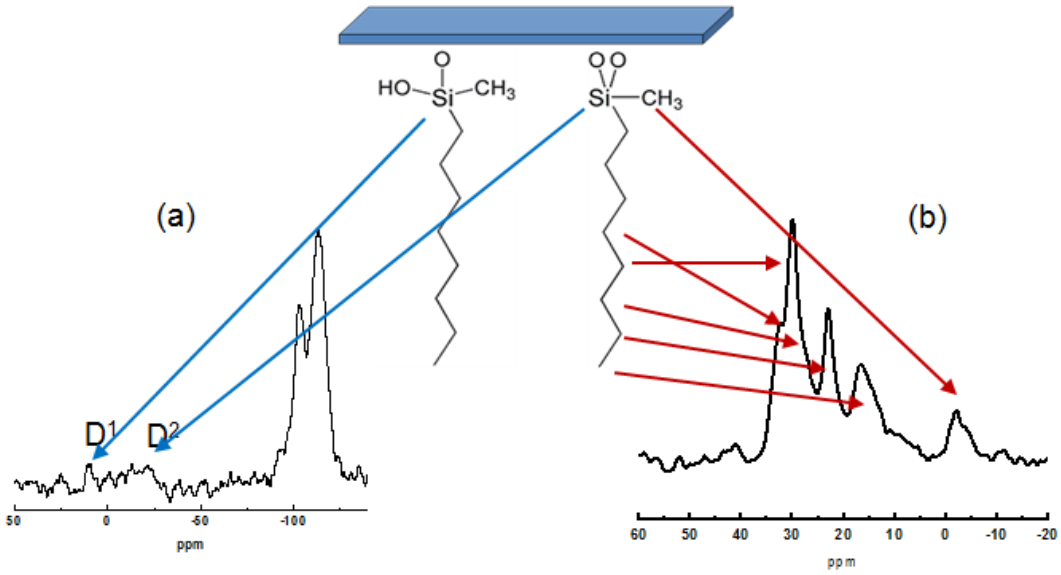

Figure 2-10. (a) ^{29}Si-NMR and (b) ^{13}C-NMR spectra for step-wise functionalized AMH-3.

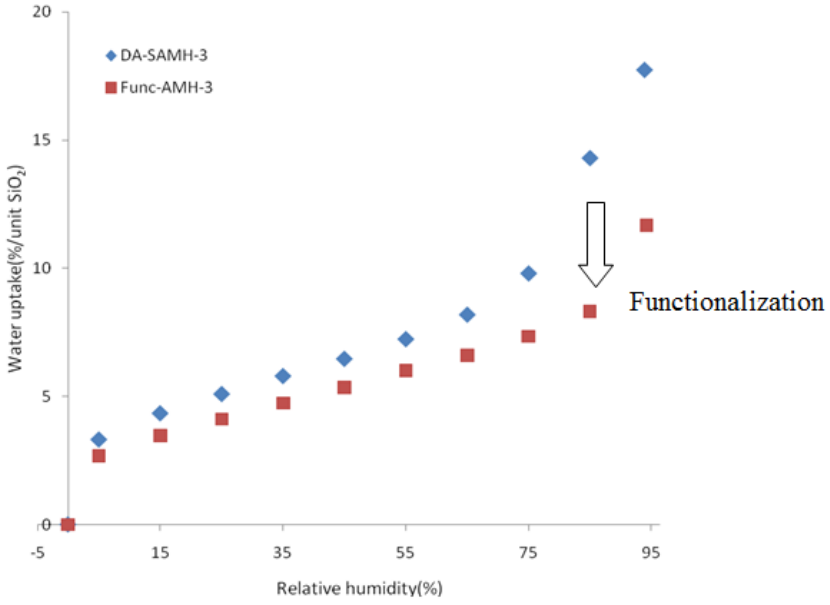

Figure 2-11. Water sorption isotherms of DA-SAMH-3, and functionalized AMH-3 at 25°C.

Figure 2-12 shows DSC and TGA curves that allow quantification of the loading of the swelling agent and functionalization agent during the process of functionalization and extraction. The initial endothermic peak in the DSC trace of DA-SAMH-3 is due to the loss of residual solvent. The broad and weak exothermic peak is due to the loss of hydrogen bond during the thermal decomposition of the swelling agent.

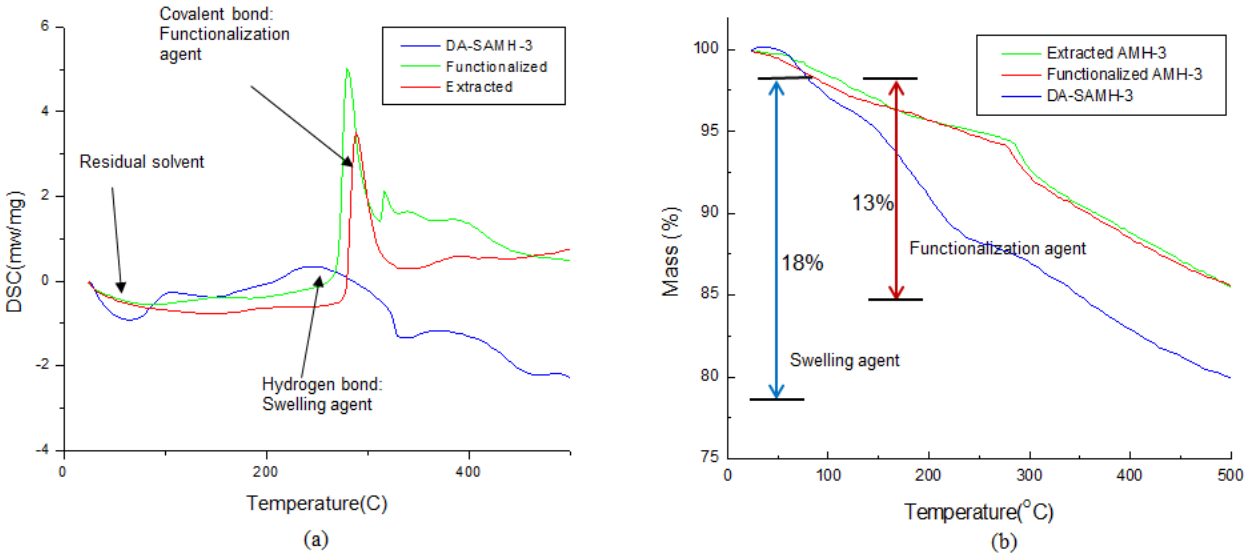

Figure 2-12. (a) DSC, and (b) TGA traces for swollen, functionalized, and extracted AMH-3.

The DSC curves of the functionalized and extracted AMH-3 show a sharp exothermic peak at 280 °C due to the decomposition of the organic groups of the functionalized silanes. Interpretation of the TGA data based on the DSC curve explains the changes in organic loadings during each steps of functionalization and extraction process. There are no hydrogen bonding (swelling agent) peaks in the DSC curves for both the functionalized and the subsequently extracted AMH-3, and correspondingly

there is no further mass losses in the TGA traces after extraction. These results demonstrate that most of the swelling agent was in fact substituted by the functionalization agent. The mass losses of 18% and 13% in swollen and functionalized AMH-3 represent comparable molar amounts of swelling agent and functionalization agent in the two materials (after normalization with the molecular weights of these agents).

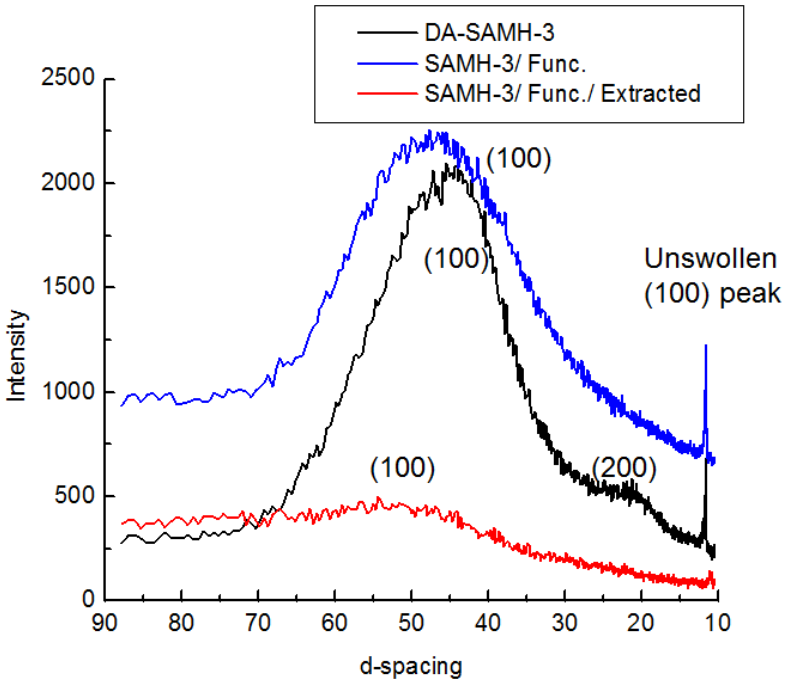

Figure 2-13. XRD patterns of AMH-3 after DA-swelling, functionalization, and extraction.

Figure 2-13 shows the changes in the XRD patterns during the process of functionalization and extraction. After the functionalization step, the (100) peak reflecting the interlayer spacing did not change significantly in relation to DA-SAMH-3, but the (200) peak was eliminated. Thus, the distribution of interlayer spacings was

broadened while maintaining the average interlayer spacing. However, the intensity of the (100) peak was mostly demolished after extraction. This clearly indicates significant delamination/exfoliation of AMH-3 layers during the extraction step. Based upon all the foregoing characterizations, the actual mechanism of step-wise functionalization of AMH-3 is suggested in Scheme 2-3. Unlike the hypothesized mechanism of Scheme 2-2, the swelling agent is in fact substituted by the functionalization agent during the first step of the functionalization reaction. During the process of step-wise functionalization reaction, the swollen AMH-3 is partially exfoliated to single layers.

Scheme 2-3. Proposed mechanism for covalent functionalization of swollen AMH-3 layers.

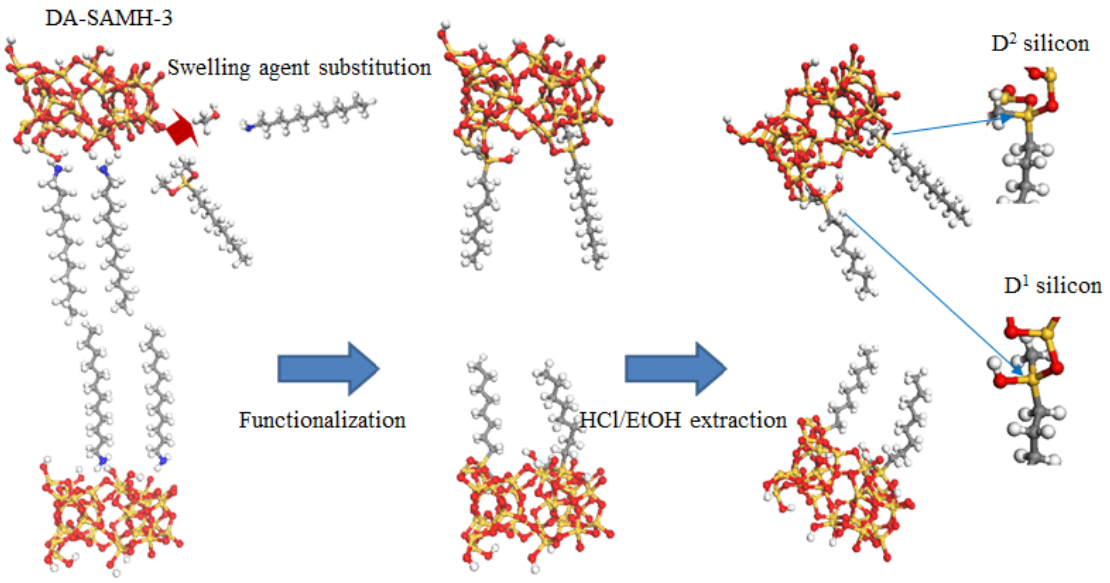

The SEM image in Figure 2-14a shows the morphology of functionalized AMH-3 after the extraction step. The material displays a partially exfoliated morphology, which is corroborated by the TEM image in Figure 2-14b. This exfoliation occurs without the application of mechanical high-shear exfoliation techniques such as melt blending or homogenization. Although outside the scope of the present study, it is proposed that the partially-exfoliated functionalized AMH-3 will improve the dispersion of AMH-3 layers when incorporated in a polymer matrix. Also, the improved surface compatibility between functionalized AMH-3 and hydrophobic polymers could benefit the adhesion and dispersion of AMH-3 layers in the polymer matrix.

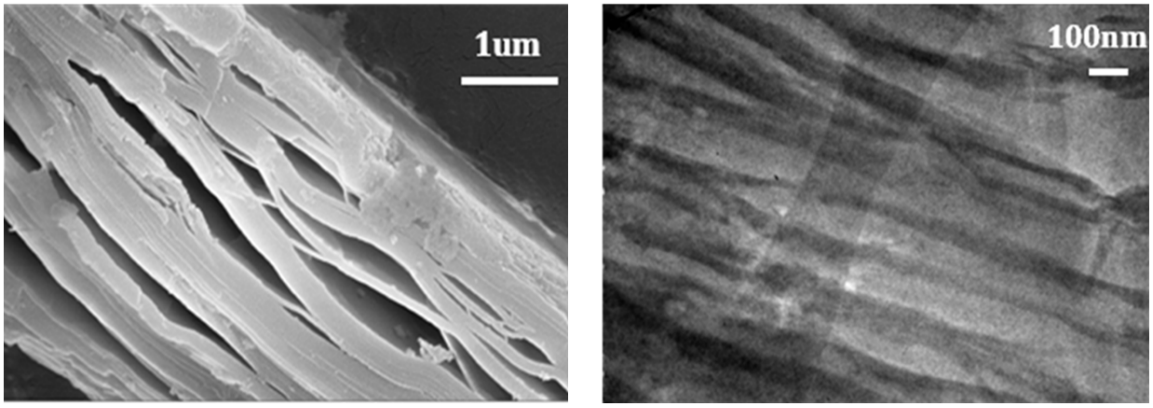

(a) (b)

Figure 2-14. (a) SEM, and (b) TEM images of functionalized AMH-3.

The figure 2-15 shows WAXS patterns for as-made AMH-3, DA-SAMH-3, and functionalized AMH-3. During the swelling process, the intensity of characteristic AMH-3 Bragg peaks is decreased due to the increased distribution in basal spacing as well as decreased uniformity of the layer structure and alignment. However, functionalized AMH-3 shows almost the same XRD pattern as DA-SAMH-3, thereby

lending further support to our conclusion that the structure of DA-SAMH-3 is preserved during functionalization reaction using reflux conditions at 110°C.

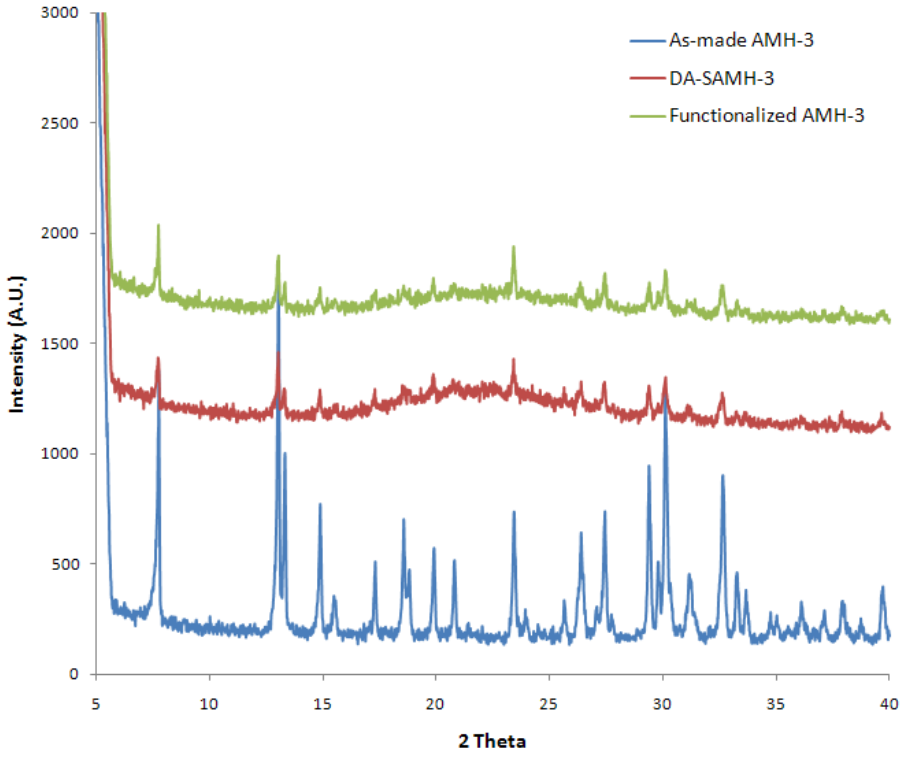

Figure 2-15. WAXS patterns of AMH-3, DA-SAMH-3, and Functionalized AMH-3

Figure 2-16 shows N_2 physisorption isotherms for DA-SAMH-3 and functionalized/extracted AMH-3. The reliability of the BET surface area for swollen AMH-3 is unclear. As shown earlier, the BET surface area of swollen AMH-3 is highly affected by the amount of interlayer amines extracted/evaporated during the degassing step prior to the physisorption measurements[19]. However, the covalently

bound functionalization agent is not subject to this limitation, and indeed shows a high BET surface area (82 m^2/g). Furthermore, the increased degree of exfoliation of functionalized/extracted AMH-3 is confirmed by complementary techniques such as XRD, SEM, and TEM.

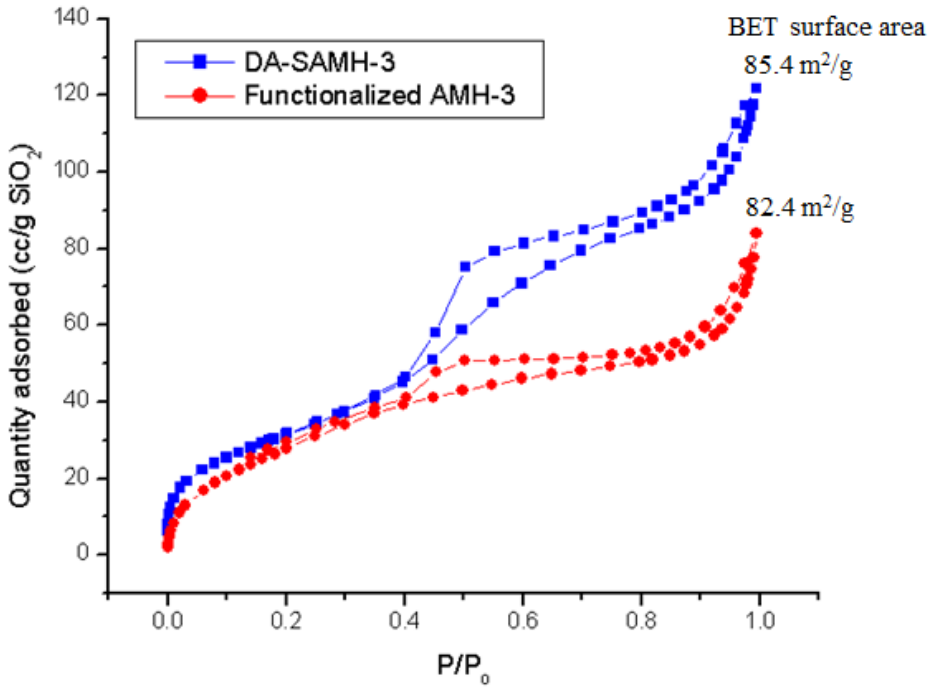

Figure 2-16. N_2 physisorption isotherms for DA-SAMH-3 and functionalized AMH-3.

2.3.3. Swelling/Functionalization of MCM-22

The methodology of step-wise functionalization was applied to functionalize the layered silicate MCM-22. A previous study reports that delaminated MCM-22 (referred to as ITQ-2) has a high density of hydroxyl groups at the layer surface[43]. The functionalization of MCM-22 will therefore effectively improve the hydrophobicity of

layer surface by substituting the hydroxyl groups with covalently bound hydrocarbon chains. Figure 2-17 shows SEM images of MCM-22(P), swollen MCM-22, and functionalized MCM-22. Starting from the well-defined MCM-22 (P) crystal morphology, swollen MCM-22 shows a serrated morphology after swelling and partial exfoliation. However, the functionalized MCM-22 also shows a small amount of particulate material. This is possibly due to the partial decomposition of MCM-22 crystals in the harsh conditions under reflux reaction at 110°C, as well as the acidification process via low pH HCl solution during extraction step.

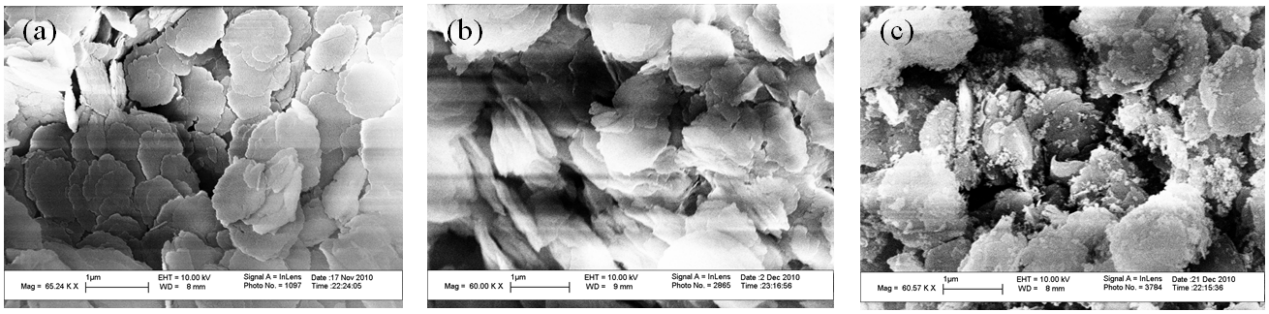

Figure 2-17. SEM images of (a) MCM-22(P), (b) Swollen MCM-22, and (c) Functionalized MCM-22.

Figure 2-18 shows the changes in the XRD patterns of MCM-22 after swelling, functionalization and extraction steps. The initial 27 Å interlayer spacing of MCM-22(P) increased to 45 Å after swelling by intercalation with CTAB molecules, and it decreased to 39 Å after functionalization because the swelling agent (CTAB) was partially substituted by the functionalization agent. The final interlayer spacing after extraction of CTAB molecules was 32 Å, representing a single layer of MCM-22 (~25 Å) with slightly twisted octylsilane chains (~7-10 Å).

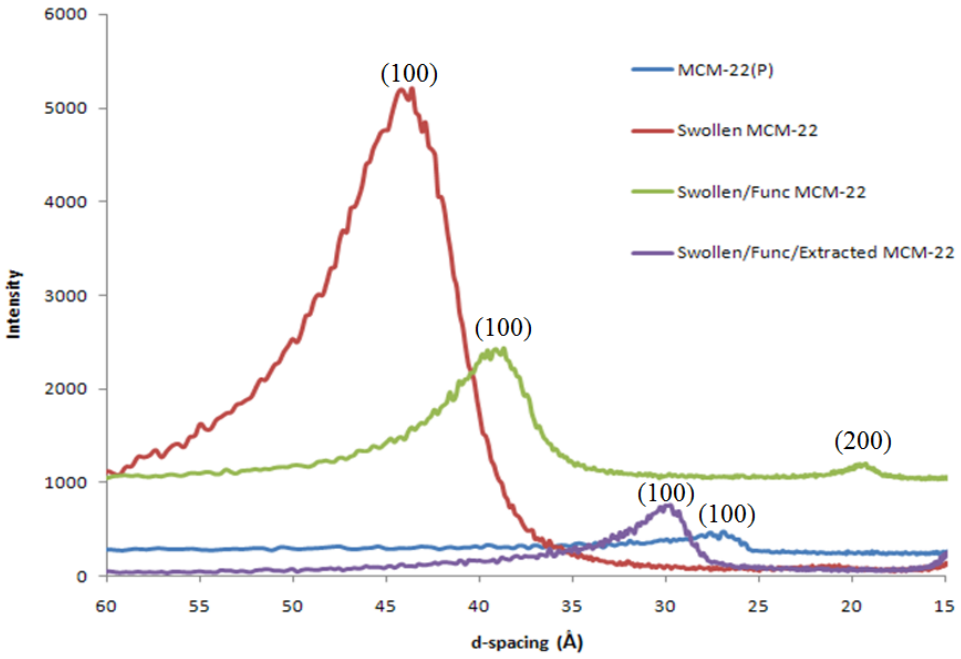

Figure 2-18. XRD patterns of MCM-22 during the step-wise functionalization process.

The ^{13}C-NMR spectra shown in Figure 2-19 were assigned to the different organic species existing between MCM-22 layers. The MCM-22 (P) interlayer space includes hexamethylenimine (HMI) as a templating agent, and quarternary ammonium (CTAB) ions were added after the swelling reaction. Then, octyl(methyl) dimethoxysilane was attached to the layers during the functionalization reaction. During extraction, the swelling agent was eliminated while HMI and the functionalization agent remained in the interlayer space.

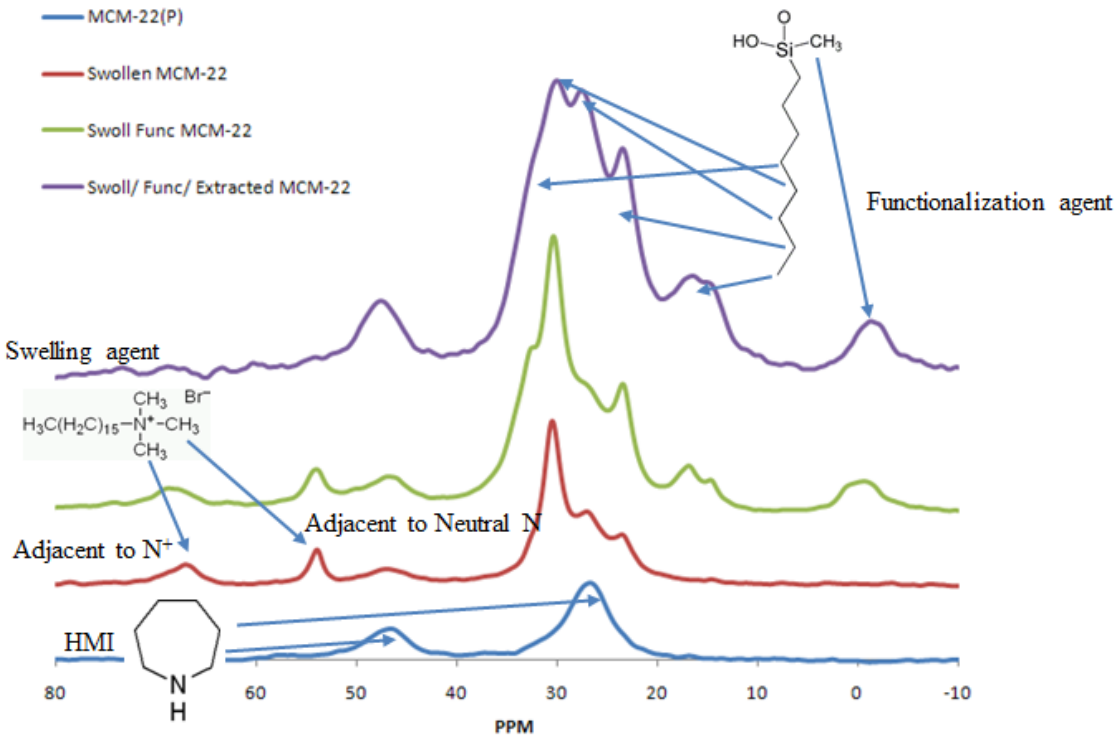

Figure 2-19. ^{13}C-NMR spectra of MCM-22 during the step-wise functionalization process.

The ^{29}Si-NMR spectra in Figure 2-20 show the presence of surface-attached silane and the structural changes during swelling, functionalization and extraction step. After functionalization, the D^2 silicon peak is present, corresponding to surface-condensed functionalization agent. The D^2 silicons are largely converted to D^1 silicons during the extraction step, likely due to acid hydrolysis[116]. The structural changes can be analyzed by examining the Q^n (n = 2-4) peak changes. Starting from MCM-22 (P), the Q^2 peak intensity increased after the swelling step, reflecting the breaking of Si-O bonds of Q^3 silicate tetrahedra[108]. Functionalization steps increased the Q^4 peak intensity relative to Q^2 and Q^3, because the functionalization reaction converts Q^2 and Q^3 tetrahedra to Q^4.

The extraction step further increases the Q^4 silicon peak significantly, due to partial demolition of the MCM-22 structure during acidification.

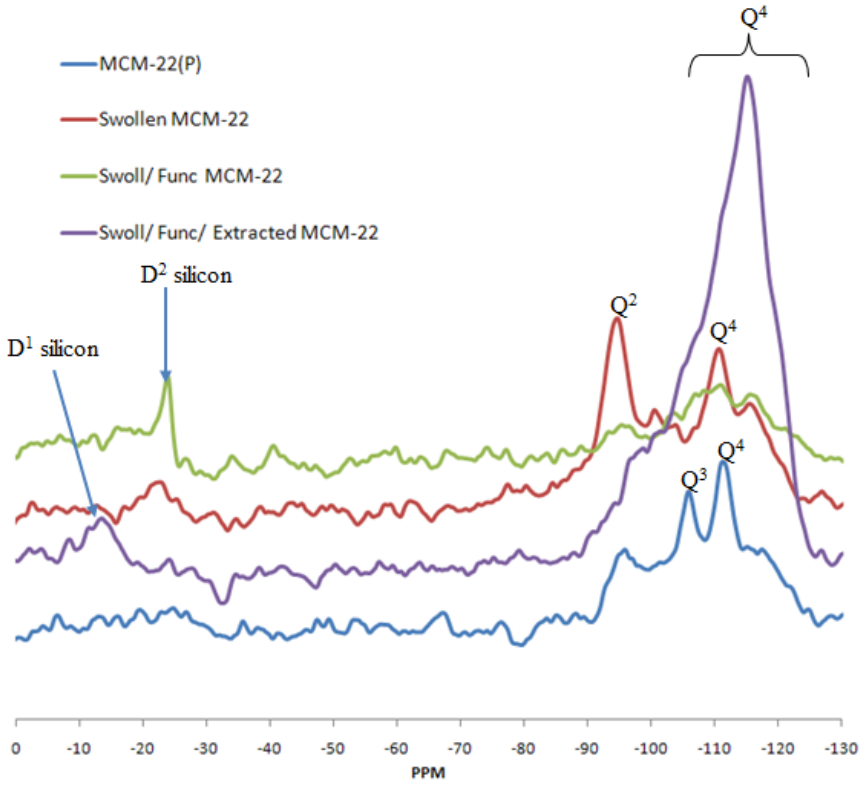

Figure 2-20. ^{29}Si-NMR spectra of MCM-22 during step-wise functionalization process.

Figure 2-21 shows water sorption isotherms for swollen and functionalized MCM-22, to determine the changes in surface hydrophobicity of MCM-22 particles after functionalization. Water sorption decreased after the functionalization process, due to the presence of hydrocarbon chains. As in the case of AMH-3, this improved hydrophobicity may be beneficial for improving compatibility of MCM-22 layers with hydrophobic polymer matrices.

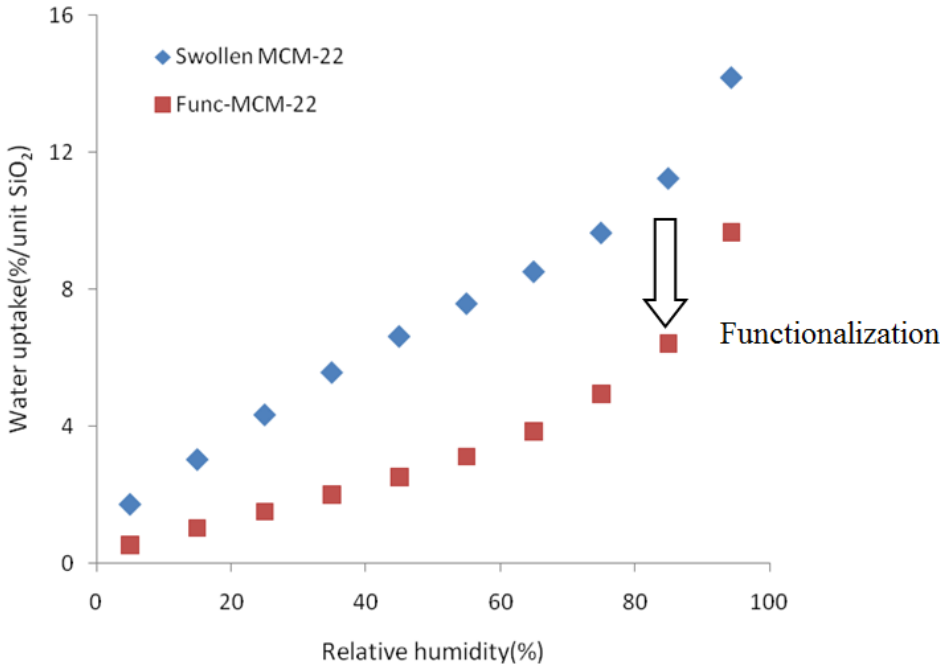

Figure 2-21. Water sorption isotherms for swollen MCM-22, and functionalized MCM-22. The % water loadings are calculated based upon the amount of SiO2 in the initial MCM-22 structure.

Figure 2-22 shows DSC and TGA traces of MCM-22 during swelling, functionalization and extraction processes. All the materials show similar DSC curves that have sharp exothermic peaks around 400°C. These peaks correspond to the decomposition of HMI and functionalization agent between MCM-22 layers. The TGA traces show that MCM-22(P) includes 15 wt% of templating agent (HMI) between layers. After the swelling reaction, the organic loading increased to 40 % due to uptake of the swelling agent (CTAB). During the functionalization reaction, some portion of swelling agent and HMI are substituted by the functionalization agent, resulting in a decreased organic loading of 28 wt%. The remaining CTAB was eliminated during the extraction step to yield a 15 wt% organic loading comprising both functionalization agent and remaining HMI.

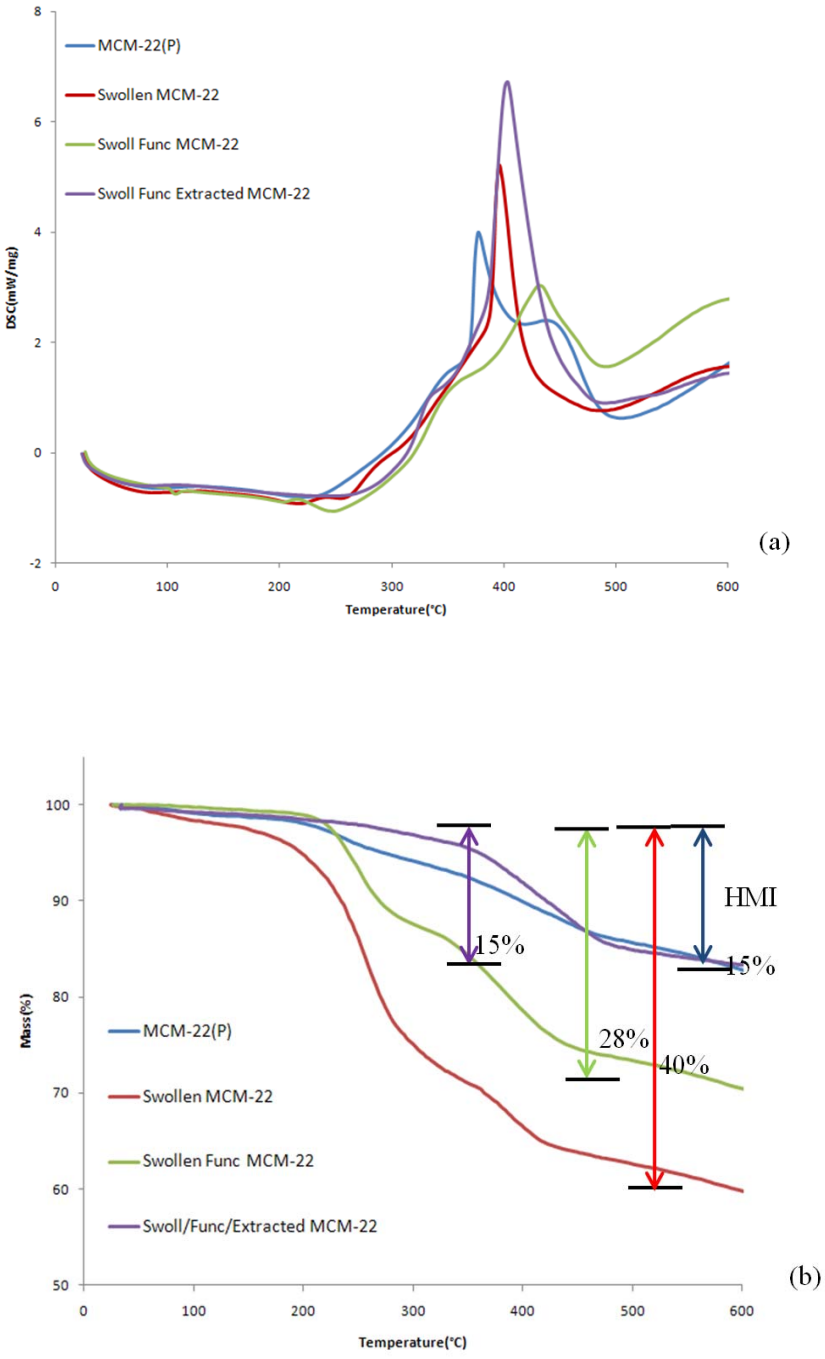

Figure 2-22. DSC (a) and TGA (b) traces of MCM-22 during step-wise functionalization process.

Based on the above characterization data, the likely mechanism of step-wise functionalization of MCM-22 is shown in Scheme 4. Na^+ cations in as-synthesized

MCM-22 are exchanged to CTAB molecules at alkaline conditions after swelling step. During the functionalization reaction, some portion of both the hexamethylenimine (HMI) templating agent and CTAB swelling agent are substituted by functionalization agent. The remaining swelling agent is eliminated by HCl/EtOH solution during extraction step. Also, the D^2 silicon atoms are converted to D^1 silicons by acid hydrolysis[116] during the extraction step.

Scheme 4. Step-wise functionalization mechanism for MCM-22.

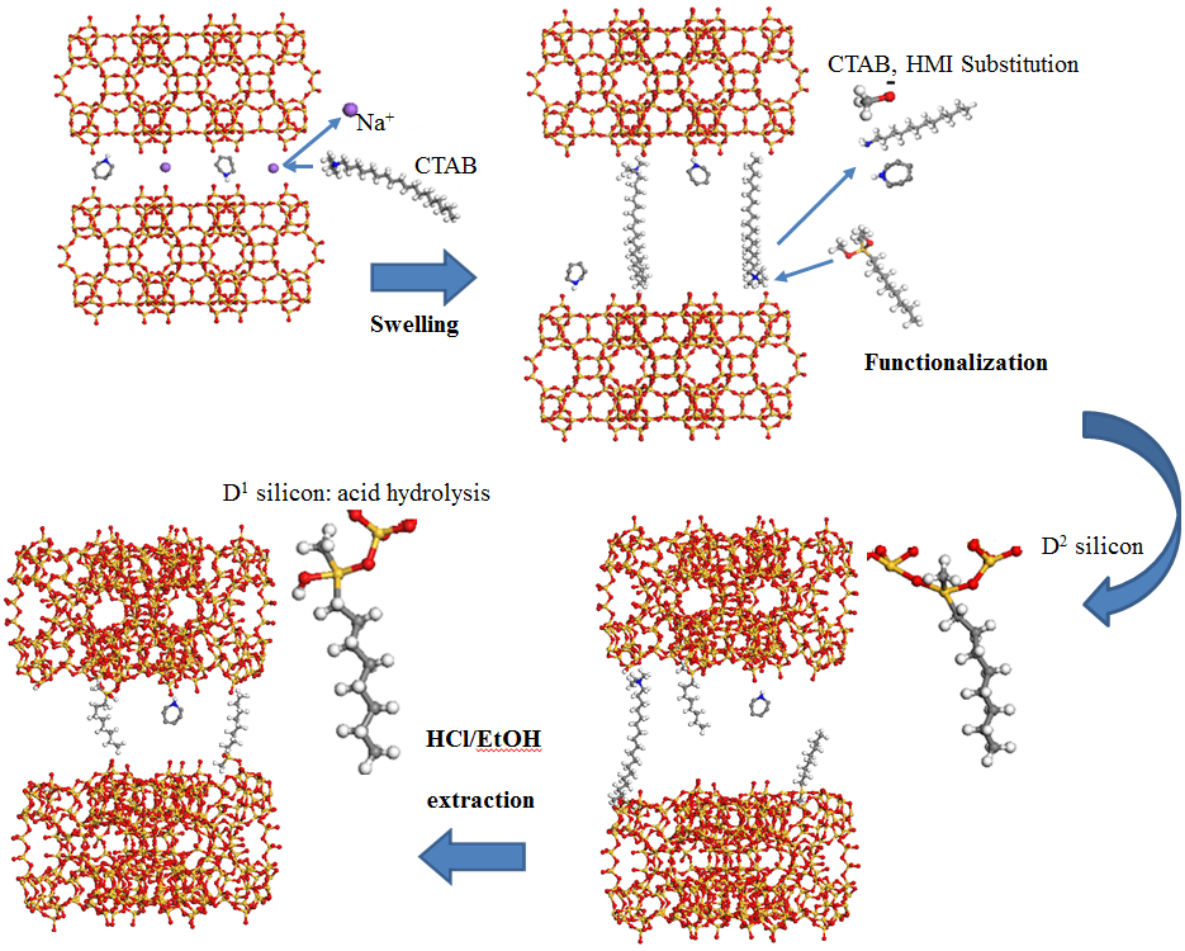

In summary, the step-wise functionalization method developed in this work was also successfully applied to MCM-22. The formation of covalent bonds between the functionalization agent and MCM-22 layer surfaces was confirmed by ^{29}Si-NMR, ^{13}C-NMR, XRD, and TGA/DSC characterization. As in the case of AMH-3, the surface-functionalized MCM-22 showed higher hydrophobicity (as confirmed by water sorption analysis), that is expected to allow better compatibility with hydrophobic polymer matrices. However, the possible formation of amorphous silicate materials induced by structure demolition during the functionalization and extraction processes is unclear, and is an issue to be further explored. It may be possible to use milder conditions of low temperature and more moderate pH for these steps.

2.4. Conclusion

This chapter reports the development and detailed analysis of surface modification techniques for layered materials with nanoporous layers, such as AMH-3 and MCM-22. Firstly, a modified swelling method for AMH-3, based upon the use of diamine swelling agents, was developed. The use of dodecyldiamine as a swelling agent led to a swollen AMH-3 material with a well-defined XRD pattern, a lower unswollen AMH-3 fraction, and a better-preserved layer structure than AMH-3 swollen with a monoamine swelling agent. Then, a step-wise covalent functionalization method for AMH-3 and MCM-22 was developed. Detailed characterization confirmed the incorporation of covalently-bonded surface functionalization agent at the layer surfaces of AMH-3 and MCM-22. The functionalization process also yields an AMH-3 material with partially exfoliated layers and improved hydrophobicity. The present set of swollen

and functionalized AMH-3 and MCM-22 materials are proposed for further investigation and use in the fabrication of molecular sieving nanocomposite membranes.

CHAPTER 3: NANOPOROUS LAYERED SILICATE AMH-3/CELLULOSE ACETATE NANOCOMPOSITE MEMBRANES FOR GAS SEPARATIONS

3.1. Introduction

The demand for higher-performance gas separation membranes is rapidly emerging because of their potential to reduce energy consumption in chemical processing. Polymeric membranes possess the limitation of a trade-off between selectivity and productivity.[9] Inorganic molecular sieve (e.g., zeolite) membranes are being developed as an alternative due to their highly selectivity and permeability.[11,117] Despite their promising characteristics in gas separation, defect-free zeolite membranes are presently difficult to synthesize economically on large scale. Hence, composite/hybrid ('mixed matrix') membranes are widely being studied to overcome the limitations of polymeric and zeolite membranes and best combine the advantages of each type of material.[118] Various inorganic porous materials such as zeolite, metal oxide nanotubes, and metal organic frameworks (MOFs) have been incorporated in polymers, and show varying degrees of enhancement in separation performance.[23,119-121] However, control over the interfaces between the inorganic and polymeric materials is found to be a critical but difficult issue. Moreover, it is found that high (30-60 wt%) loadings of the inorganic materials are often necessary to produce substantial improvements in membrane performance.[24,122] While recent progress has been made towards resolving these issues,[85,123] it remains unclear whether such membranes can be reliably fabricated on a large scale with high loadings of inorganic

materials and a low density of defects.

Another approach towards hybrid membranes involves the use of the 'selective flake' concept, utilizing nanoporous layered silicates incorporated in polymer membranes.[25,26] This relatively recent concept is illustrated in Figure 3-1. The distinctive geometrical features of layered materials, *i.e*., small thickness and high aspect ratio, are hypothesized to provide large increases in separation performance with the presence of only a small amount of inorganic material. For example, the high aspect ratio can decrease permeability of larger gas molecules (too large to pass through the nanopores) by requiring a highly tortuous path around the layers. At the same time, the small thickness of layered materials could improve the permeability of smaller gases due to a much lower diffusion resistance than thicker bulk filler particles.[25] These combined effects are expected to lead to highly permeable and selective gas separation membranes with only small loadings of the layered material. Furthermore, nanometer-thin layered materials are more amenable to the fabrication of submicron membranes (e.g., the incorporation of layered materials in skin layers of hollow fiber membranes).[29]

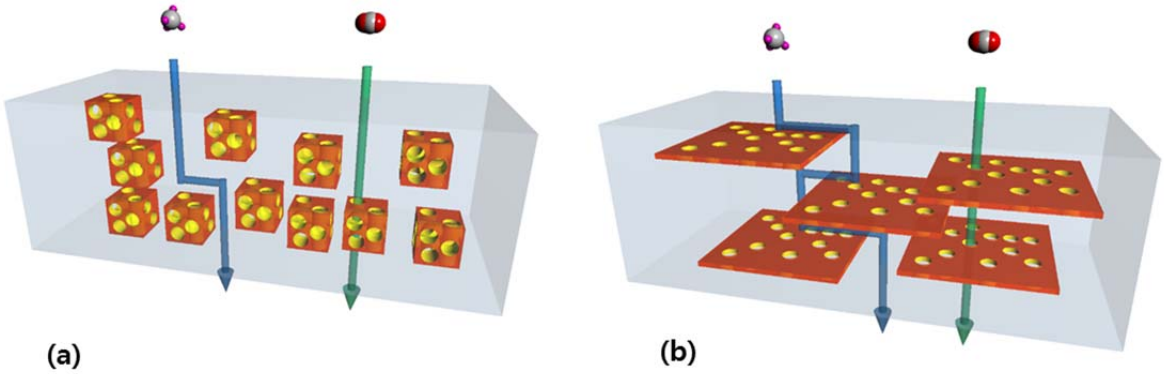

Figure 3-1. Schematic diagrams of (a) conventional composite membrane, and (b) composite membrane containing high-aspect-ratio layered materials. The concept of sieving of one type of molecule while providing a highly tortuous path for the other using a high-aspect-ratio layered material is illustrated.

Several types of nanoporous layered materials are now known, such as the layered silicates MCM-22, UZAR-S1, and Nu-6,[124-126] layered aluminophosphates (AlPOs)[25], and layered borogermanates.[127] The nanoporous layered silicate AMH-3 was chosen for this study.[47] AMH-3 is a 3-D porous layered silicate with 8 membered ring (MR) pores, and its crystallographic pore size of 3.4 Å can potentially be useful for several important gas separations such as CO_2/CH_4 and H_2/N_2. AMH-3 was first synthesized and characterized in 2003.[47] Several challenging issues must be overcome before the fabrication of AMH-3/polymer composite membranes with high separation performance can be achieved. The first hurdle was regarding the swelling of the material to increase the interlayer spacing. Unlike conventional nonporous clay materials, AMH-3 has ordered silanol groups on the layer surfaces, accompanied by charge-balancing cations in the interlayer spaces.[128] These Sr^{2+} and Na^{+} cations form

strong ionic bonds. Furthermore, interlayer condensation may occur during exchange of these cations with protons. Conventional swelling processes used for clays were not successful for AMH-3. Hence, a new swelling process for AMH-3 was first developed by Choi *et al.*[49] The swollen AMH-3 (SAMH-3) material was incorporated in polybenzimidazole (PBI) membranes for H_2/N_2 separation[98] and into Nafion® proton exchange membranes to reduce methanol crossover.[107] Recently, we reported more detailed processes for swelling and silylation of AMH-3 while preserving its pore structure to a greater extent.[129] However, none of the above reports showed clear increases in the performance of polymeric membranes upon incorporation of SAMH-3. Furthermore, no clear evidence existed regarding the exfoliation and dispersion of SAMH-3 as high-aspect-ratio layers.

In the present work, we address the challenge of exfoliating SAMH-3 and processing it into a hybrid membrane with higher performance than a polymeric membrane. The previous studies on SAMH-3/polymer composite membranes used conventional dispersion techniques such as ultrasonication and mixing *via* stirring with a magnetic bar. These mild shearing processes cannot guarantee a high degree of exfoliation of SAMH-3 layers in the polymer matrix. Here, we fabricate SAMH-3/cellulose acetate (CA) membranes by a different route. CA is a polymeric material currently used to fabricate hollow fiber membranes for natural gas separation.[130,131] We show that a high-shear mixer with a high-speed rotating impeller can effectively exfoliate SAMH-3. The angular speed of the impeller is 7000 rpm, thereby generating a high shear rate estimated at 733 s^{-1}. We conduct a microstructural

analysis of the SAMH-3/CA composite membrane by small-angle X-ray scattering (SAXS) and transmission electron microscopy (TEM), and demonstrate that a high degree of exfoliation has occurred. We then show that the CO_2/CH_4 gas separation properties of the hybrid membranes, in particular an enhancement in the CO_2 permeability while maintaining the CO_2/CH_4 selectivity, are substantially enhanced over pure CA membranes. These unambiguous results represent a demonstration of the concept of 'high-aspect-ratio, low-loading, flakes' in the formation of composite membranes.

3.2. Experimental Section

3.2.1. Synthesis of swollen AMH-3 (SAMH-3)

Dodecylamine-swollen AMH-3 (DA-SAMH-3) was prepared as reported by us elsewhere.[129] Typically, AMH-3 crystals were synthesized by hydrothermal synthesis for 3 days. The molar composition of the reactant gel was 1 TiO_2 : 10 SiO_2: 2 $SrCl_2$: 14 NaOH : 675 H_2O. To prepare this gel, 1.38 g of sodium hydroxide (Aldrich) was dissolved in 55.85 g of DI water. After 30 minutes of stirring, 2.94 g of strontium chloride (99%, Aldrich) was added. The reactant sol became clear after 30 min stirring at 80°C. Then, 12.52 g of sodium silicate (26.5% SiO_2, Aldrich) was added. After 30 min stirring, 4.25g of titanium chloride (Fisher Scientific, 20%, HCl stabilized) was added drop-wise, and stirred for 1 hr. After 3 days of hydrothermal reaction at 200°C, the AMH-3 crystals were separated by sedimentation and decantation. To swell AMH-3, the sequential intercalation method was used. Typically, 0.776 g of DL-histidine (≥99%, Aldrich) was dissolved in 25 ml of DI H_2O

at 60°C. Then the clear solution was cooled to room temperature and the pH was regulated to 6.0 by adding several drops of HCl (36.5%, Aldrich). This clear solution acts as a buffer to provide protons for entry between the AMH-3 layers. Then, 0.2 g of as-made AMH-3 was added to the buffer solution to start proton-exchange of the metal cations present between the AMH-3 layers. In the meantime, the swelling agent solution was prepared by dissolving 2.061 g of dodecylamine (Aldrich) in 50 ml of DI H_2O at 60°C followed by 30 min stirring. After 1 hr from the start of proton exchange, the swelling agent solution was added drop-wise. After 10 hrs of stirring, swollen DA-SAMH-3 was obtained. It was purified by washing and centrifuging with DI water several times.

3.2.2. Fabrication of SAMH-3/ Cellulose Acetate (CA) composite membranes

Tetrahydrofuran (THF) was chosen as the solvent for CA. Its evaporation rate is sufficiently slow to allow time for uniform formation of the polymer after casting on a glass plate. A certain amount (e.g., 62.5 mg for 4 wt% SAMH-3/CA composite) of SAMH-3 particles was added to 8.5 g THF followed by 30 min ultrasonication. Then, 1.5 g of CA powder (Aldrich, M_w=50,000, no dehydration) was added and dissolved for 24 hrs using a rotation bar. The DA-SAMH-3/CA polymer solution was placed in a high-shear mixer (Silverson Machines LTD, L4RT-A) operating at 7000 rpm. The mixing process was carried out in a water bath maintained at 25°C. After 1 hr of high-speed mixing, the solution was sonicated for 30 min to remove any bubbles, and then cast on a glass plate using a ‘doctor’s blade’. After 24 hrs of drying, the membrane was annealed at 180°C for 24 hrs in a vacuum

oven.

3.2.3. Characterization

Wide angle X-ray Scattering (WAXS)/ Small angle X-ray Scattering (SAXS) patterns were measured from the membranes using the synchrotron X-ray beamline 5ID-D at the Advanced Photon Source (Argonne National Laboratory). The beamline energy was set at 17 KeV (λ =0.73 Å). The distance between sample and detector was set to 4,064 mm and 235 mm for SAXS and WAXS, respectively. Powder XRD patterns were obtained with a PAnalytical X'Pert Pro diffractometer operating with a Cu source (λ=1.5418 Å) and an RTMS detector. A narrow divergence slit (1/32°) and anti-scattering slit (1/16°) were used. Scanning Electron Microscopy (SEM) images were obtained by a JEOL LEO-1530 SEM at a landing energy of 10 kV with the 'In Lens' mode detector. Transmission electron microscopy (TEM) images were taken with a Hitachi HF-2000 operating at an accelerating voltage of 200 kV. For high-resolution TEM images, a JEOL 4000 EX was used at an accelerating voltage of 380 kV. To obtain cross-sectional images of composite membranes that shows the presence of AMH-3 flakes in CA composite membrane, the DA-SAMH-3/CA composite membrane was embeded in epoxy resin and cured for 1 day. The cured epoxy mould was microtomed to 80-100 nm thickness with a 35°-angled diamond knife.

3.2.4. Gas permeation

The CO_2/CH_4 separation performance for each sample was evaluated using an equimolar feed mixture of CO_2/CH_4 based on a standard isochoric (constant-

volume, variable pressure) technique.[132] Mixed gas permeation results are more practical than the corresponding single gas data since they include possible non-ideal effects such as competitive diffusion and adsorption. The upstream pressure was monitored using a 1000 psia Sensotec SC Series pressure transducer. The pressure in the downstream volume was measured using a 10 torr MKS Baratron® (Type 127) pressure transducer, and the permeate was sent to a gas chromatograph (Varian 450) for analysis. The output from the downstream pressure transducer was interfaced with a personal computer using LabView® data acquisition software for real-time data recording. The entire permeation system was maintained to within ±0.1 ºC using a proportional controller (Cole Parmer, BA-2155-54). Several measurements were performed for the thickness of each sample by using a micrometer (Ames, Waltham MA, Model #56212) and their arithmetic averages were used for permeation data analysis. Three independent membrane samples were fabricated at each SAMH-3 loading, and the permeation data from these samples was averaged.

3.3. Results and Discussion

3.3.1. SAMH-3 Exfoliation

Swollen AMH-3 (SAMH-3) was prepared by hydrothermal synthesis and the sequential intercalation method, as explained in the Experimental Section. For the preparation of exfoliated and dispersed layered silicates, procedures such as high-shear melt blending using a twin screw extruder,[79,108] or direct intercalation of polymer chain between layers using in-situ polymerization,[133,134] have been reported. However, these processes are not easily applied to the fabrication of CA/SAMH-3

composite membranes due to the rigidity and poor melt-processibility of cellulose acetate. For effective exfoliation of SAMH-3 particles, a high-shear mixing process was adopted. For comparison, we also performed conventional vortex mixing of SAMH-3 in water. Figure 3-2a shows an SEM image of the morphology of SAMH-3, which consists of collections of swollen layers into sheets, with mesoscopic spacing between the sheets. The approximate molecular structure (deduced from XRD, NMR, and IR) of SAMH-3 was previously reported elsewhere.[129] In vortex mixing, 10 mg of SAMH-3 particle was added to 1g of water and placed in the vortex mixer for 15 min. Figure 3-2b shows the surface morphology changes in SAMH-3 after vortex mixing in water. The spacing between some of the sheets of SAMH-3 was significantly increased and the onset of exfoliation is seen. Figure 2c shows the result of the vortex mixing process for SAMH-3 in tetrahydrofuran (THF), which is the solvent used in this study for fabrication of nanocomposite membranes. The result is similar to that obtained in water. One difference between the two cases is the observation of small clusters of material on the SAMH-3 surface after vortex mixing in THF. This is believed to be due to the extraction of the swelling agent by THF and deposition on the SAMH-3 external surface. The degree of exfoliation is dominated by the shear stress acting on the SAMH-3 layers rather than chemical affinity between the solvent and the layers. The two solvents used for vortex mixing were DI water and THF, both of which have low viscosities (~10^{-3} Pa-sec). The results in Figures 3-2b and 3-2c also suggest that if a high-viscosity polymer solution is used instead of water, further exfoliation might occur to the large increase in shear stress on the sheets.

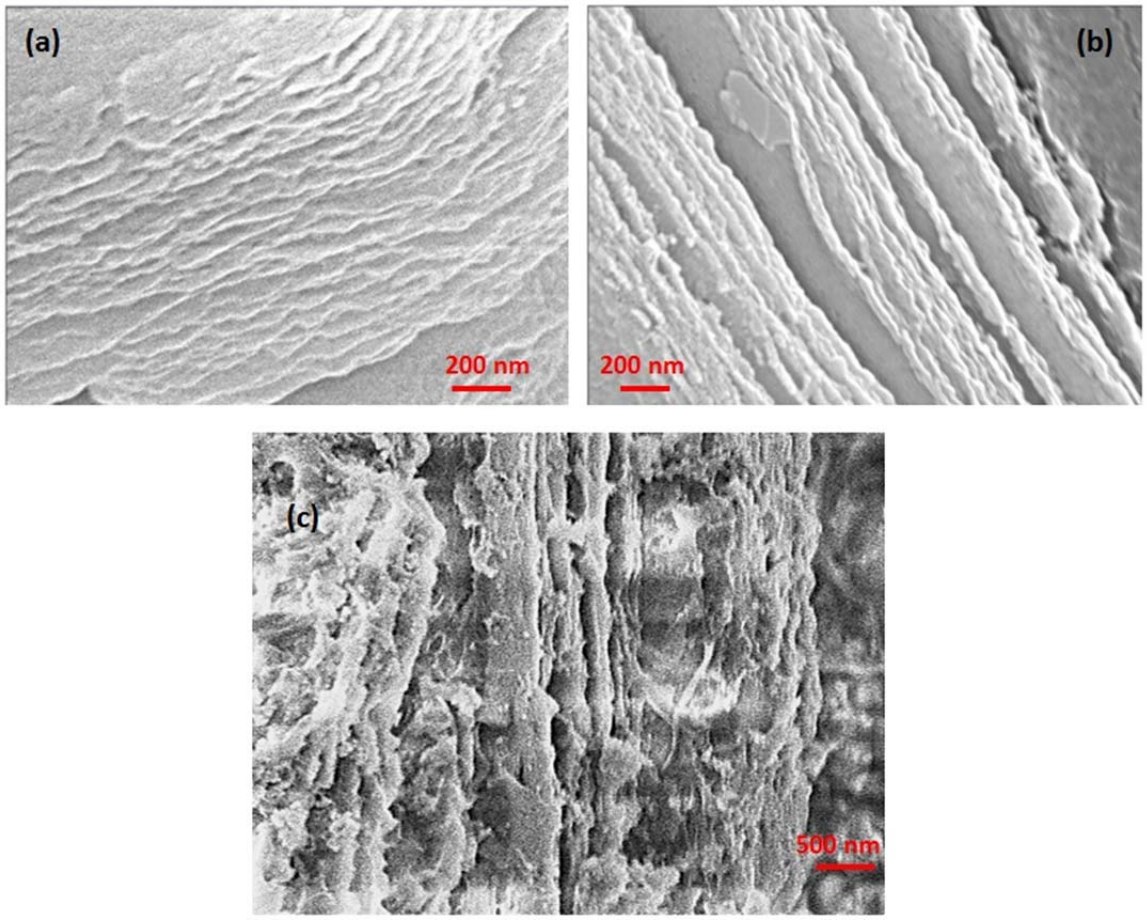

Figure 3-2. Surface morphology of (a) SAMH-3, and vortex-agitated SAMH-3 (b) in water (c) in Tetrahydrofuran (THF) organic solvent.

3.3.2. DA-SAMH-3/ CA Composite Membranes

SAMH-3/CA composite membranes were fabricated using a high shear mixer at 7,000 rpm, as described in the Experimental Section. The viscosity of the SAMH-3/polymer dispersion was about 30 Pa-sec.[135] Figure 3-3a shows the XRD pattern of

SAMH-3 particle, and Figures 3-3b~3-3e show the wide angle X-ray scattering (WAXS) patterns of membranes with different SAMH-3 loadings (0-6 wt%). Characteristic high-*hkl*, low-intensity, Bragg peaks of SAMH-3 particles (marked with asterisks) are still visible after their incorporation in CA membranes, indicating that the internal structure of the SAMH-3 layers was preserved in the mechanical exfoliation process. The present WAXS and XRD patterns do not cover the low-*hkl* Bragg peaks. Due to the low intensity of the high-*hkl* peaks, they cannot be quantitatively analyzed. Quantitative information on the exfoliation of SAMH-3 stacks can only be determined by analyzing the lower *Q*-region (0.005-0.2 $Å^{-1}$). Small angle X-ray and neutron scattering (SAXS/SANS) have been widely used for analyzing microstructure and morphology of polymeric materials. For example, they give detailed information regarding the structure of ionomers such as Nafion® and sulfonated polyimides, such as the size and orientation of water nanochannels.[86,87] The structure and morphology of cellulose acetate membranes has also been studied by SANS, and results comparable to transmission electron microscopy (TEM) are obtained.[88]

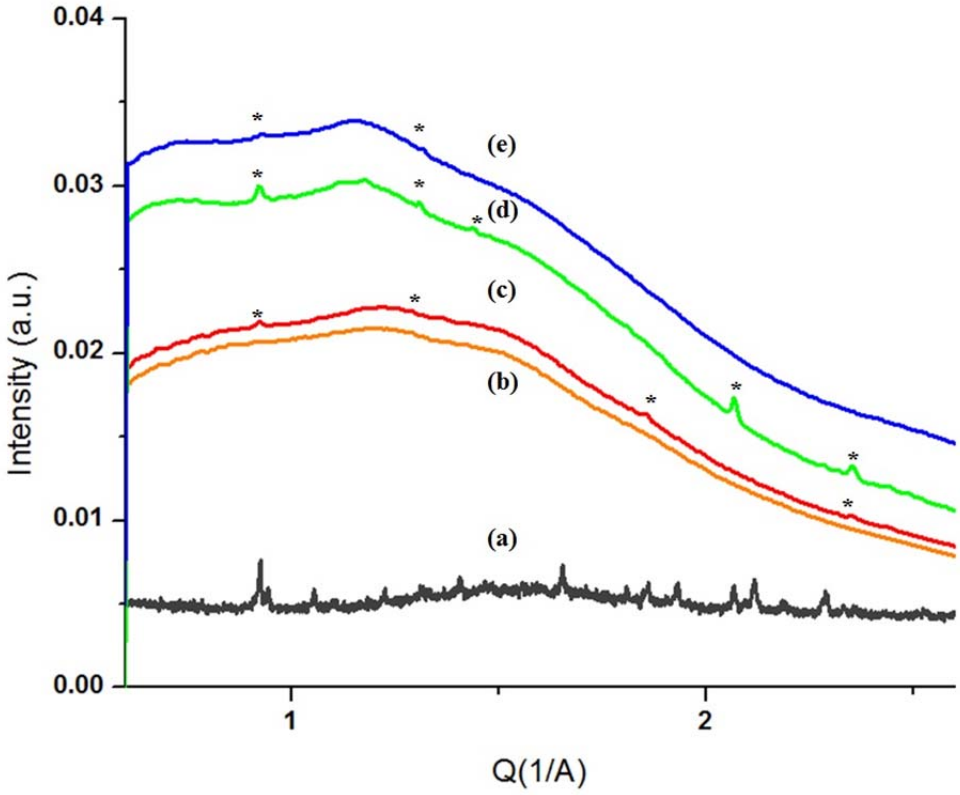

Figure 3-3. WAXS patterns of (a) DA-SAMH-3 powder (In-house XRD), (b) bare CA membrane, and (c) 2 wt%, (d) 4 wt % , and (e) 6 wt % SAMH-3/CA nanocomposite membranes (Synchrotron XRD).

Based on the geometry of inorganic fillers (e.g., sphere, disk, or rod), different X-ray/neutron scattering models have been developed to fit experimental intensity data and obtain morphological information on the inorganic fillers.[89,90] We measured SAXS patterns of SAMH-3/CA composite membranes with different loadings of SAMH-3, and performed detailed fitting simulations to obtain the morphological parameters of the dispersed SAMH-3 layers. The simulations were performed with the IGOR Pro program containing the scattering model packages (obtained from the NIST Center for Neutron Research).[136] The stacked-tactoid model was adopted for the membranes.[91] The governing SAXS intensity equation, and the

form factor/ structure factor models, are given in Equations 1-5.[38,39] The form factor *P(Q)* includes the particle size and orientation, and the structure factor *S(Q)* describes the structure of the stacks *via* the interlayer spacing and the average number (and Gaussian variance) of layers in the stacks. The SAXS intensity also depends on the number density of AMH-3 plates and the electron density difference between the silicate, interlayer space, and the polymer matrix.

$$I_{total}^{SAMH3}(Q) = N_{SAMH3} \int_0^{\pi/2} \left[\Delta\rho_l\left(V_t f_t(Q) - V_c f_c(Q)\right) + \Delta\rho_c V_c f_c(Q)\right] S_S(Q) \sin\varphi d\varphi$$

(3-1)

$$S_S(Q) = 1 + \frac{2}{N}\sum_{k=1}^{N}(N-k)\cos(kDQ\cos\varphi) \times \exp[-k(Q\cos\varphi)^2{\sigma_D}^2/2]$$

(3-2)

$$P_c(Q) = \int_0^{\pi/2}\left[\frac{\sin(Qh\cos\varphi)}{Qh\cos\varphi} \times \frac{2J_1(QR\sin\varphi)}{QR\sin\varphi}\right]^2 \sin\varphi d\varphi \quad ; \; P_c(Q) = f_c(Q)^2$$

(3-3)

$$P_t(Q) = \int_0^{\pi/2}\left[\frac{\sin(Q(d+h)\cos\varphi)}{Q(d+h)\cos\varphi} \times \frac{2J_1(QR\sin\varphi)}{QR\sin\varphi}\right]^2 \sin\varphi d\varphi \quad ; \; P_t(Q) = f_t(Q)^2$$

(3-4)

$$\rho(SLD) = \sum \frac{Zr_e}{v_m} \; , \; r_e = 2.81 \times 10^{-13} cm$$

(3-5)

In these equations, R = tactoid radius, h = silicate layer thickness, ρ_c = silicate layer electron density, ρ_1 = interlayer electron density, ρ_p = polymer electron density, $\Delta\rho_c = \rho_c - \rho_p$, $\Delta\rho_1 = \rho_1 - \rho_p$, N = number of silicate layers in stack, d = average thickness of surfactant layers, D = interlayer distance (center-to-center), σ_D = standard deviation of interlayer distance, N_{SAMH3}= scale factor: number of platelets in unit volume × membrane thickness, Z_i = atomic number of i-th atom, v_m= molecular volume. We classify the structural parameters in Equations 3-1~3-5 into fixed parameters (whose values are pre-calculated and fixed during fitting), global parameters (whose values are fitted but remain the same across all the membrane samples), and sample parameters (whose values are fitted and change from sample to sample). These parameters are listed in Table 3-1. Specifically, the flake radius R was set as 10,000 Å as obtained from the TEM analysis (discussed later in this report), and the AMH-3 layer thickness h is known to be 10 Å.[47] The electron density of AMH-3 layers ρ_c was calculated as 1.862×10^{-5} Å^{-2} using Equation 5. The electron density of the interlayer swelling agent ρ_1 and the polymer matrix ρ_p were fitted globally for all the samples since they are independent of the AMH-3 loading. These parameters were constrained to have maximum values corresponding to the bulk density and composition of the swelling agent and the polymer.

Table 3-1. Structural parameters in stacked-tactoid model for global fitting of SAXS data.

Fixed parameters	**Global fit parameters**	**Material fit parameters**
R = 10,000 Å (TEM)	ρ_1 : maximum value = 7.80×10^{-6} Å^{-2}	N
		d
		σ_D
h = 10 Å (AMH-3 structure)	ρ_p : maximum value = 1.14×10^{-5} Å^{-2}	N_{SAMH3}
ρ_c : 1.86×10^{-5} Å^{-2} (AMH-3 layer composition)		

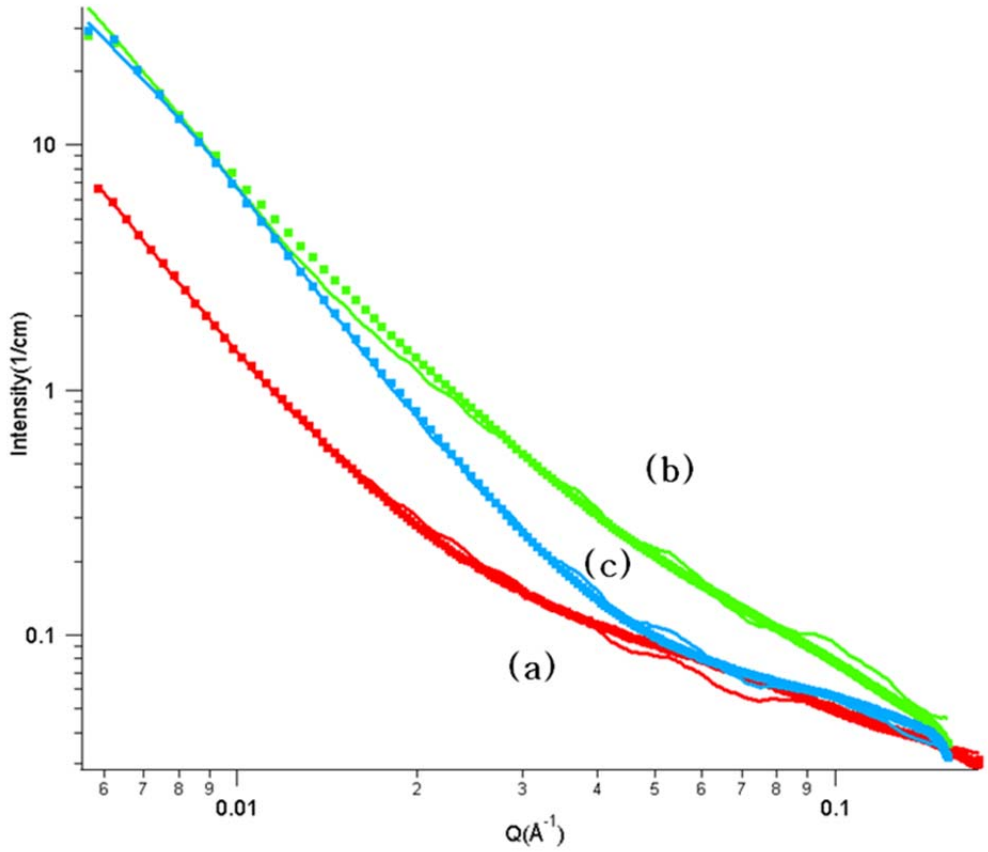

Figure 3-4. Measured SAXS patterns (points) and model fits (continuous curves) for (a) 2 wt%, (b) 4 wt % , and (c) 6 wt % SAMH-3/CA nanocomposite membranes.

Figure 3-4 and Table 3-2 show the SAXS data and the results of the fitting simulations for SAMH-3/CA composite membranes with 3 different particle loadings (2-6%). Good fits of the experimental spectra were obtained. Table 3-2 shows the structural parameters obtained for SAMH-3 stacks in the composite membranes. The average number of stacks of AMH-3 layers in each composite membrane was found to be in the range of N = 4-8, thereby demonstrating a high degree of exfoliation of

the SAMH-3 particles from the original swollen material. The surfactant layer thickness between AMH-3 layers in the composite membranes was found to be in the range of 12-20 Å. This is about a factor-of-two decrease in comparison to the original 30 Å surfactant layer distance[129] of SAMH-3. The large forces acting on the particles during high-speed mixing may also induce normal (in addition to shear) forces on the SAMH-3 layers, thereby resulting in compression of the interlayer spaces. Additionally, it is likely that some of the dodecylamine molecules may be extracted from the interlayer spaces during high-shear mixing, thereby shrinking the interlayer spaces. The final layer thickness is comparable to the length of one dodecylamine molecule (~15 Å), and hence it is likely that the initial bilayers of the swelling agent between the AMH-3 layers have converted to monolayers due to the extraction of the swelling agent and/or compressive forces. As for the global parameters, fitting gives the electron density of the interlayer spaces (ρ_l) as 7.24×10^{-6} $Å^{-2}$, slightly lower than the maximum allowed value in Table 3-1. This implies a pretty packed arrangement of swelling agent between the silicate layers after converted to monolayers. However, the fitted value of the electron density of the cellulose acetate matrix equals 8.1×10^{-6} $Å^{-2}$ - a decrease of about 30% from the calculated maximum - indicating a potential decrease in density of the CA packing due to the presence of the AMH-3 layers. The fitted scale factor ($N_{SAMH\text{-}3}$) is also shown in Table 2 after normalization by the membrane sample thickness. Because SAXS absolute intensity is a function of membrane thickness and the number density of AMH-3 (single) layers, the normalized scale factor $N_{SAMH\text{-}3}$ has the physical meaning of the number of AMH-3(single) layers per unit volume. From the data in Table 3-2, it is seen that the

normalized scale factor linearly increases with AMH-3 loading (R^2 of linear regression = 0.95). This result further corroborates the validity of the SAXS global fitting simulations and the reliability of the obtained structural parameters shown in Table 3-2.

Table 3-2. Structural parameters from SAXS fitting simulations.

SAMH-3 wt %	**# of stacks *N***	**Surfactant layer thickness *d* (Å)**	**Distance standard deviation σ_D (Å)**	**Normalized Scale factor N_{SAMH-3}**
2%	3.7	20	3.4	2.7×10^{-4}
4%	4.0	12	4.7	5.6×10^{-4}
6%	8.1	14	1.7	6.9×10^{-4}

TEM characterization was used to visualize dispersed AMH-3 flakes in SAMH-3/CA composite membranes. Figure 3-5 shows representative cross-sectional images of microtomed composite membrane samples. As seen from the low-magnification image in Figure 3-5a, intact exfoliated AMH-3 layers/ flakes as well as some broken AMH-3 layers are observed together in the CA polymer matrix. Figures 3-5b~3-5d show higher-resolution images of typical flakes. The small thickness and high aspect ratio of the AMH-3 flakes was uniformly seen. The thickness of

exfoliated AMH-3 tactoids varies from 15-30 nm, and they are typically hundreds of nanometers to microns in length. Since the thickness of a combined silicate-swelling agent pair is ~ 3 nm, the thicknesses observed in TEM correspond to 5-10 silicate layers in the dispersed tactoids, which agrees well with the SAXS fitting results. The interfacial adhesion between the polymer matrix and the AMH-3 flakes was found to be of good quality, and no 'leaky' regions or voids were found. In addition to highly exfoliated AMH-3 flakes shown in Figures 3-5a~3-5d, a few partially exfoliated AMH-3 regions were also found as shown in Figure 5e. These regions reveal details about the state of the interlayer spaces in the middle stages of high-shear exfoliation. Delaminated single layers of AMH-3 are also seen in Figure 5e (marked with red arrows).

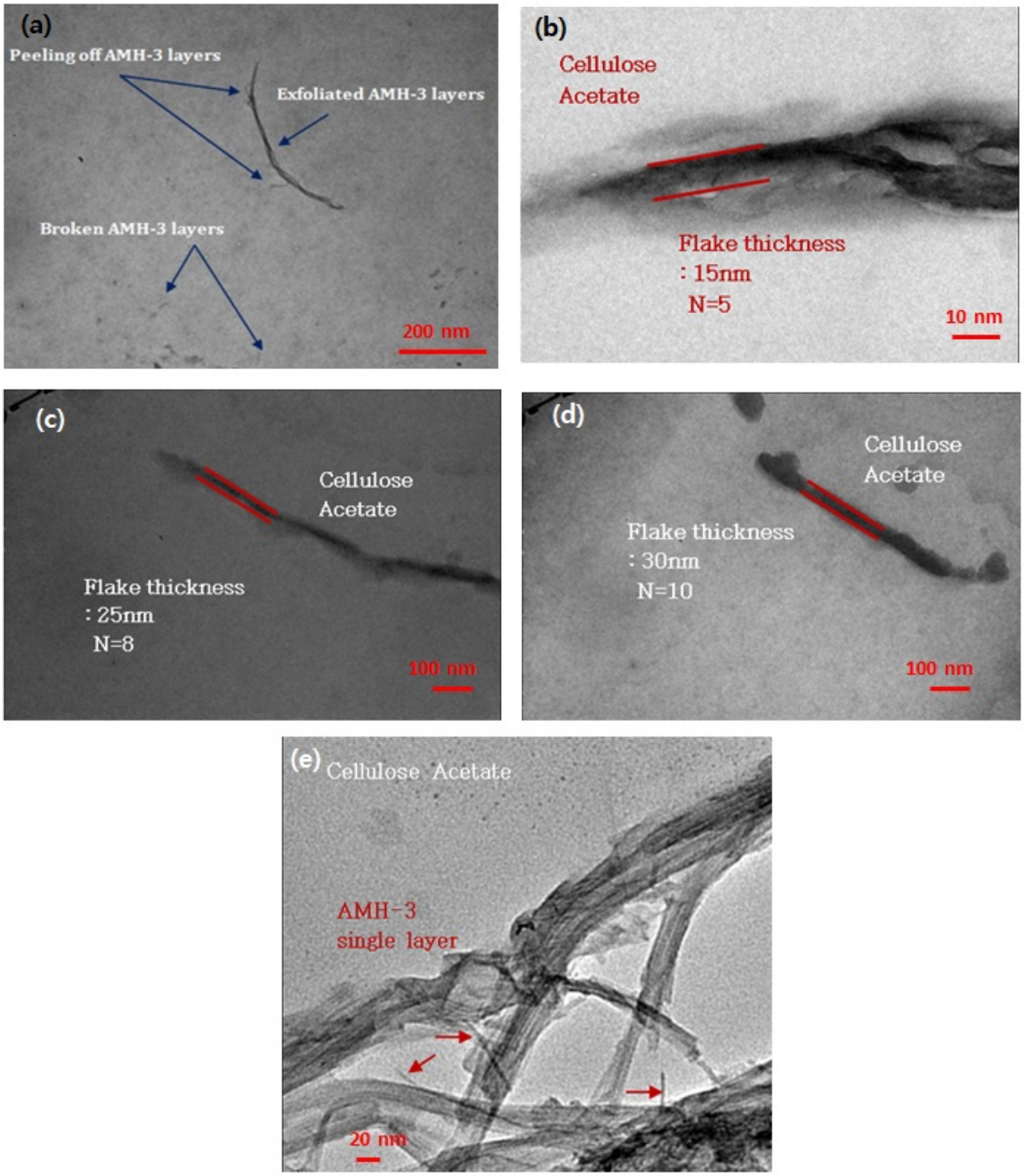

Figure 3-5. TEM images of exfoliated AMH-3 in 6% SAMH-3/CA composite membranes: (a) low-magnification image, (b)-(d) high resolution images to show typical flake thicknesses, and (e) partially exfoliated SAMH-3 flakes.

After the fabrication and microstructural analysis of SAMH-3/CA composite membranes, we measured their CO_2 and CH_4 gas permeability and selectivity using a 50:50 mixture gas. Table 3-3 and Figure 3-6a show the CO_2/CH_4 permeation results as a function of flake loadings. The separation performance is substantially enhanced by incorporating only 2, 4, or 6 wt% of SAMH-3 particles. Specifically, the CO_2 permeability increased by almost 54% and CO_2/CH_4 selectivity has been maintained at the same level as the pure CA membrane. This is a clear demonstration of the 'nanoporous flake/polymer hybrid membrane' concept that shows significant improvement on gas permeability while maintaining selectivity.

Table 3-3. CO_2 and CH_4 permeabilities, and CO_2/CH_4 selectivities, of CA/SAMH-3 composite membranes.

	Bare CA	**2 wt % SAMH-3**	**4 wt % SAMH-3**	**6 wt % SAMH-3**
P_{CO2} (Barrer)	7.55±0.29	9.65±0.02	10.36±0.25	11.59±0.39
P_{CH4} (Barrer)	0.26±0.01	0.33±0.01	0.35±0.01	0.39±0.01
$\alpha_{CO2/CH4}=P_{CO2}/P_{CH4}$	29.61±0.29	29.24±0.80	30.03±0.34	29.71±0.17

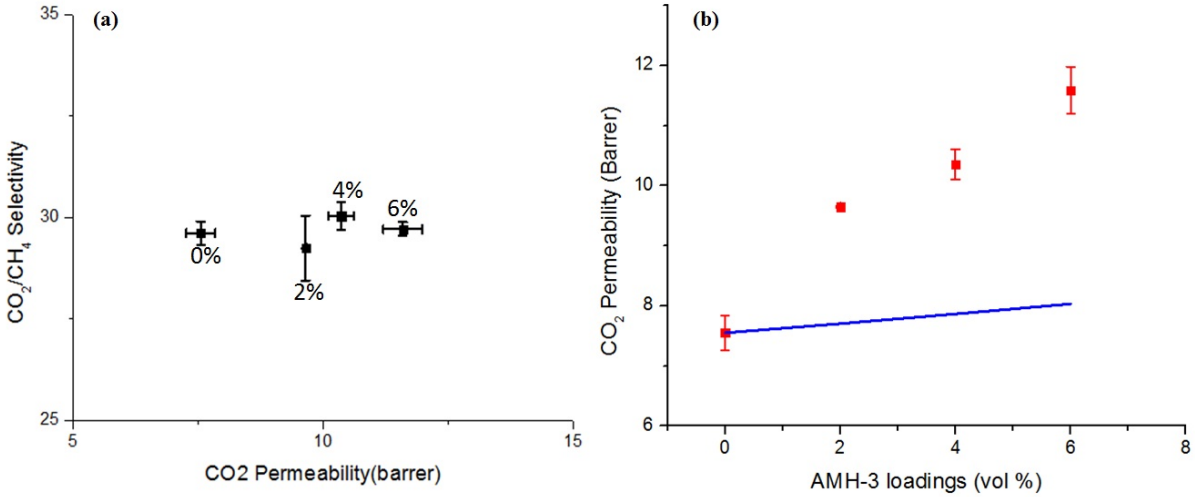

Figure 3-6. (a) Gas permeation in SAMH-3/Cellulose Acetate (CA) composite membranes at a pressure differential of 65 psi: Error bars were calculated from multiple measurements with independent samples (b) Measured CO_2 permeability (symbols) of SAMH-3/CA composite membranes and comparison to the limit (solid line) predicted by the Cussler model.

The enhancement of CO_2 permeation (as shown in Figure 3-6a) with only a small loading of porous flakes cannot be explained by conventional permeation models for membranes containing high-aspect-ratio flakes. To illustrate this, the Cussler model[95] (Equation 3-6) was applied to fit our experimental data of CO_2/CH_4 gas separation and to estimate the permeability of gases through AMH-3 layers. The Cussler model estimates the flux (J) of a component in a membrane containing porous flakes in relation to the flux (J_0) in a bare membrane:

$$\frac{J_0}{J} = 1 - \varphi + \left[\frac{1}{\frac{1}{\delta\varphi} + \frac{1-\varphi}{\alpha^2\varphi^2}}\right]$$

(3-6)

Here φ is the particle loading, α is the particle aspect ratio, and δ is the ratio of diffusivities of the component in the matrix and the flakes. In the present case, the aspect ratio α ~30 based on TEM analysis, and the only fitting parameter is δ. Figure 6b shows our experimental data for CO_2 permeability of composite membranes as a function of flake loading (0, 2, 4, 6 %) and the highest possible permeability predicted by the Cussler model (when $\delta \to 0$, i.e., CO_2 diffusion through the filler is infinitely faster than through the polymer). It is seen that the model cannot describe the experimental permeation data from the SAMH-3/CA composite membrane. A similar result was previously predicted by Konduri,[137] who calculated the diffusivity of H_2, N_2, and O_2 in the AMH-3/PDMS nanocomposite system by molecular dynamics simulations and showed that the Cussler equation cannot explain the H_2/O_2 and H_2/N_2 selectivities obtained from atomistic simulation. The incorporation of nanoscale flakes in the CA matrix results in a new material with its own characteristic molecular transport properties that cannot necessarily be understood as a combination of the bulk properties of the two constituent materials.

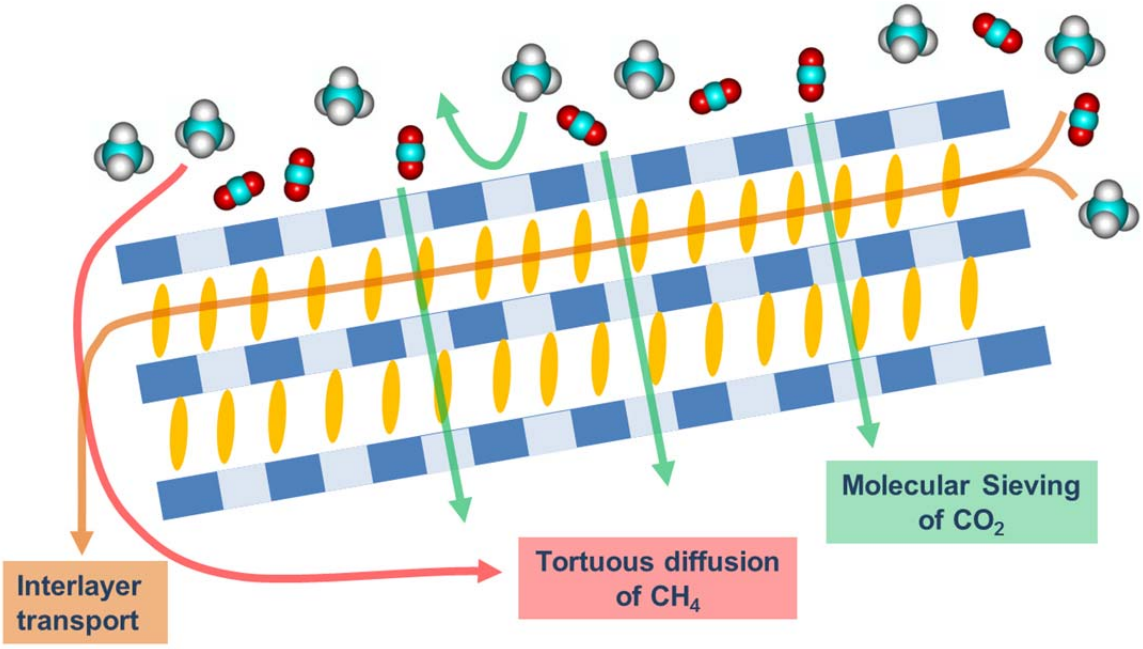

Figure 3-7. Schematic diagram of composite membrane containing high-aspect-ratio SAMH-3 flakes. Possible transport mechanisms are illustrated, including CO_2 molecular sieving through the SAMH-3 layers, tortuous diffusion of CH_4 around the flakes, and Knudsen transport of both gases through the interlayer spaces.

Figure 3-7 illustrates possible mechanisms that explain the gas permeation enhancement in this system. Based on SAXS/TEM analysis, the exfoliated AMH-3 is stacked in flakes of 4-8 layers, with interlayer spaces of size ~ 2 nm containing the swelling agent. The molecular sieving effect and high aspect ratio (~ 30) of the exfoliated AMH-3 tactoids may increase the CO_2 permeability and the CO_2/CH_4 selectivity.[98,104,107] At the same time, transport through the mesopores that are known to exist in the interlayer spaces[129], may also result in enhanced gas permeability for both CO_2 and CH_4. In a limiting case, transport through the interlayer spaces could

be governed by Knudsen diffusion, wherein CH_4 is transported ~1.7 times faster than CO_2. This may tend to lower the overall CO_2/CH_4 selectivity in the composite membrane. This complex transport mechanism operating within the SAMH-3 flakes can also be interpreted as increasing the effective volume fraction of the inorganic material. It is of future interest to control the permeability and selectivity of the interlayer spaces, by further increasing the degree of exfoliation of the AMH-3 layers or introducing other materials (e.g., silica or polymers) to substitute the swelling agent in the mesoporous interlayer spaces. In comparison to composite membranes using isotropic molecular sieve particles that conventionally require incorporation of up to 50 wt% of molecular sieve particles,[24] the enhancement of separation performance using small quantities of nanoporous layered oxides such as SAMH-3 may find important applications in reducing the required membrane area, as well as avoiding problems associated with high particle loadings such as agglomeration, leaky interfaces, and loss of mechanical strength.

The above proposed mechanism does not include the effects of possible changes in the polymer packing[15] caused by incorporation of the AMH-3 flakes, although these effects may be small for the low flake loadings. As mentioned earlier, the fitted electron density of the CA matrix in the SAXS analysis indicates a possible lowering of the CA matrix density. This may have the effect of increasing the permeability of the CA matrix (*i.e.*, the value of J_0 in the Cussler equation could increase with AMH-3 loading). The maintenance of CO_2/CH_4 selectivity in such a situation could be explained as being due to a competing effect of the SAMH-3 flakes (which increase the selectivity) and the expanded CA matrix (which lowers the

selectivity). More detailed characterization of the CA matrix phase is required to validate this hypothesis.

3.4. Conclusions

SAMH-3/Cellulose Acetate (CA) nanocomposite membranes were fabricated with the use of a high-shear mixer, and the microstructure and properties of the resulting membranes was investigated by a range of experimental techniques. From our detailed SAXS study, the numbers of SAMH-3 layers in an exfoliated stack are found to be 4-8, in good agreement with the SAMH-3 flake thickness measured by TEM. The SAMH-3/CA composite membranes were investigated for their CO_2 and CH_4 gas permeation characteristics. Significant improvements in mixed-gas separation performance were attained with only 2-6 wt% of AMH-3 loading. This effect cannot be predicted by conventional models, and indicates a complex combination of transport phenomena occurring in such membrane systems. Such transport phenomena include competing effects of transport through the SAMH-3 pores, the interlayer spaces, and potentially through a lower-density CA matrix phase. The present approach could be practically useful in mitigating effects of particle aggregation and poor polymer-particle adhesion encountered in fabricating composite membranes with higher volume fractions of inorganic materials.

CHAPTER 4: EPITAXIALLY GROWN LAYERED MFI-BULK MFI HYBRID ZEOLITIC MATERIALS

4.1. Introduction

Zeolites are aluminosilicate materials with shape/size-selective nanopores, and are widely applied in separations and catalysis.[138,139] Recent works have led to new ways of controlling molecular diffusion limitations in zeolite materials. These include the synthesis of nano-sized zeolites,[140] and layered and exfoliated (i.e., 2-D) zeolites.[42,43,45] Hierarchical zeolite-mesoporous hybrid materials have also been developed to expand the applications of zeolites to handling bulky molecules such as heavy hydrocarbons and biomolecules.[141,142] The interconnected microporous and mesoporous components have complementary features: acid sites in the micropores and fast diffusion paths in the mesopores.[143,144] For example, such structures were recently obtained from ultrathin layered MFI materials.[145] Long-chain diquaternary ammonium cations (C_{22}-N^+-C_6-N^+-C_6) were used as templating agents to form a 2-D lamellar MFI-type material. This material was further pillared to prevent interlayer condensation during calcination.[53] Another method of preventing interlayer condensation is the synthesis of hexagonally ordered MFI/mesoporous hybrids.[146] This complex material showed interesting catalytic properties related to the existence of both micropores and mesopores. Exfoliated layered MFI was also exploited in the formation of zeolitic membranes for hydrocarbon separations.[79]

In this work, we introduce a different approach to the construction of hybrid microporous/mesoporous materials, via epitaxial (lattice-matched) growth of a 2-D layered zeolite on the surface of a bulk (3-D) zeolite material. There are a few demonstrations of epitaxial growth between two conventional zeolite materials, such as the growth of Zeolite-β on SSZ-31 nanofibers[147] and the growth of cancrinite (CAN) on sodalite (SOD).[148] Here we report the first example of epitaxial growth of a 2-D layered zeolite (layered MFI) at the surface of a conventional zeolite (MFI). In this hybrid material, referred to as "Bulk MFI-Layered MFI" (BMLM), the conventional MFI provides shape/size-selective micropores as well as condensed acid sites, and acts as a support to prevent interlayer condensation and disordering of the layered MFI that otherwise occurs upon calcination. The layered component provides a combined mesoporous/microporous network and surface acid sites of controlled structure. Furthermore, control over the size of both domains (layered and bulk) can be obtained by selecting appropriate particle sizes of the bulk component and varying the epitaxial growth conditions for the layered component. In this work, we describe in detail the synthesis and characterization of this hybrid zeolite materials. Furthermore, we illustrate an application of this material based upon its roughened yet highly porous surface morphology, which can be used for obtaining a high degree of zeolite-polymer adhesion during the formation of composite zeolite/polymer membranes. Other recently-developed approaches for this purpose involve the growth of nanostructures of dense metal oxides/hydroxides such as $MgO/Mg(OH)_2$ on the zeolite surface.[23,149,150] However, the latter surface-roughened materials show variable stabilities of the surface nanostructures

and reductions in porosity.[150] The BMLM-type hybrid materials are shown to avoid these problems.

4.2. Experimental Methods

4.2.1. Synthesis

Conventional MFI particles of two different sizes (10 μm and 300 nm) were synthesized hydrothermally as described in previous works.[151] The synthesis of the the long-chain diquaternary ammonium cation (C_{22}-N^+-C_6-N^+-C_6) as a structure-directing agent (SDA) for layered MFI, was carried out as described previously.[145] For comparison with the BMLM material, pure layered MFI was also synthesized as described in previous work.[53,145] The synthesis of BMLM materials was accomplished by the same reaction gel composition used for synthesizing pure layered MFI. However, the bulk MFI particles were added to the gel. In this report, no aluminum source was included in the BMLM synthesis, and a pure-silica hybrid material was obtained. The molar composition of the reaction gel was 30 Na_2O: 100 TEOS : 10 $C_{22\text{-}6\text{-}6}Br_2$: 18 H_2SO_4: 70 bulk MFI: 4000-16000 H_2O. The molar quantity of the bulk MFI particles was set to 70% of the dissolved Si source (TEOS). The water content was varied from 4000 to 16000 to examine the corresponding morphological changes in the BMLM material.

4.2.3. Characterization

Scanning Electron Microscopy (SEM) of particles and membranes was performed with a JEOL LEO-1530 operating at 10 kV. Cross-sections of membranes were prepared by fracturing the sample in liquid nitrogen. Elemental analysis was performed by SEM-

EDX. Samples were gold-coated to prevent surface charging effects. Low-magnification Transmission Electron Microscopy (TEM) was performed with a Hitachi HF-2000 at 200 kV. High Resolution TEM (HR-TEM) was performed on a FEI Tecnai G^2 F30 TEM at 300 kV. Typically, the BMLM particles were embedded in epoxy and sliced into 50-nm thin sections by a Leica EM UC6 Ultramicrotome equipped with a diamond knife. Thermogravimetric analysis (TGA) was performed with a Netzsch STA409. The scanning temperature was 30-900°C at a ramping rate of 10°C/min, under an N_2:O_2 stream flowing at 90:50 ml/min. N_2 physisorption isotherms were obtained at 77 K with a Micrometrics Tristar II. The samples were degassed for 12 hrs at 150°C.

4.2.4. Membrane fabrication

MFI/ Matrimid® composite membranes were fabricated *via* a blade-casting method on a glass plate. Dichloromethane (DCM) was used to dissolve the polyimide (Matrimid®). For the fabrication of a 20 wt% particle-loaded composite membrane, 0.375 g of particles were dispersed in 8.5 g of DCM and sonicated for 30 min. Then, 1.5 g of Matrimid® powder was added and stirred for 1 day using a rotation bar. The dispersion was then sonicated for 30 min to remove any air bubbles. Then, the dispersion was poured on the glass surface and cast using a 'doctor's blade' with a height of 12 mils (300 □m). The cast membrane was placed in stagnant air for 1 day and then annealed at 180°C for 24 hrs.

4.2.5. Permeation measurements

The single-component permeabilities of CO_2 and CH_4 were determined using the isochoric (constant-volume, variable pressure) technique.[132] The upstream pressure was monitored using a 1000 psia Sensotec SC pressure transducer. The pressure in the downstream collection volume was measured using a 10 torr MKS Baratron (Type 127) pressure transducer. The output from the downstream pressure transducer was interfaced with a personal computer using the LabView software for real-time data recording. The entire permeation system was maintained to within ±0.1 ºC using a proportional controller (Cole Parmer, BA-2155-54). Several measurements were performed for the thickness of each membrane sample with a micrometer (Ames, Waltham, MA, Model #56212), and were then averaged.

4.3. Results and Discussion

4.3.1. Synthesis of Layered MFI and BMLM

The morphology and structure of layered MFI was found to be identical to that reported previously.[145] Figure 4-1 shows the SEM images of the synthesized layered MFI, which displays high-aspect-ratio platy structures aggregated with each other. Therefore, the surface morphology of the layered MFI aggregate is highly roughened. The XRD patterns (Figure 4-2) show the crystal structure of Layered MFI. The XRD pattern of layered MFI includes only (*h0l*) peaks while missing the (*0k0*) peaks, thereby representing the 2-D layered MFI. TEM images are shown in Figure 4-3. Layered MFI contains approximately 3-nm thin MFI layers with about 3 nm spaces between layers.

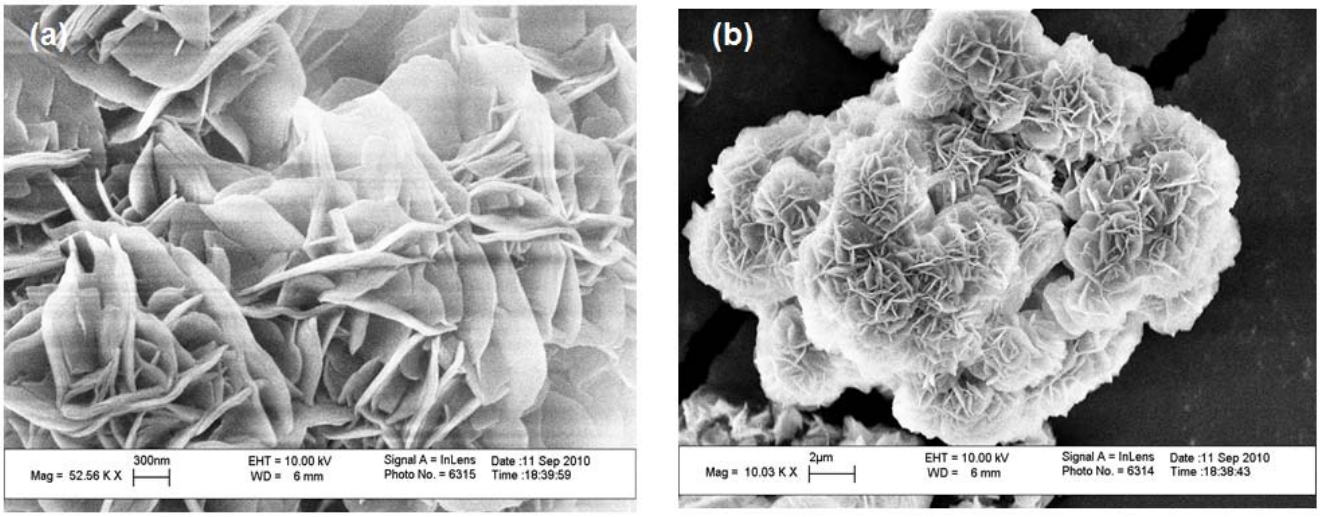

Figure 4-1. SEM Images of synthesized layered MFI.

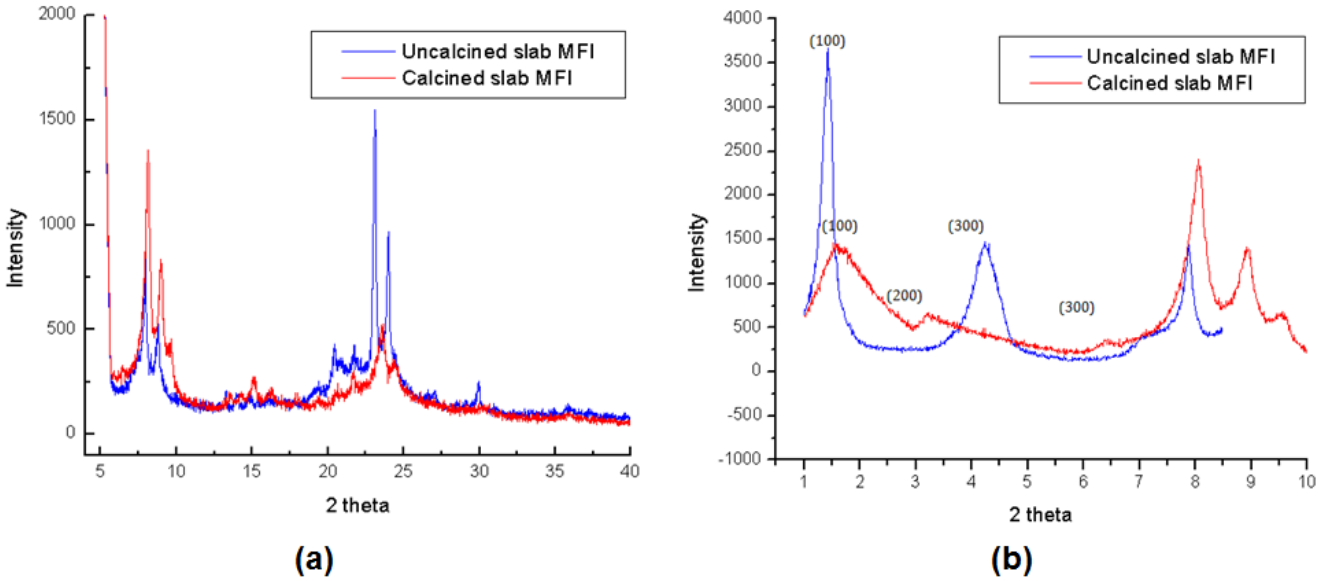

Figure 4-2. XRD pattern of synthesized layered MFI in the (a) high angle (5-40°) (b) low angle (1-10°) regions.

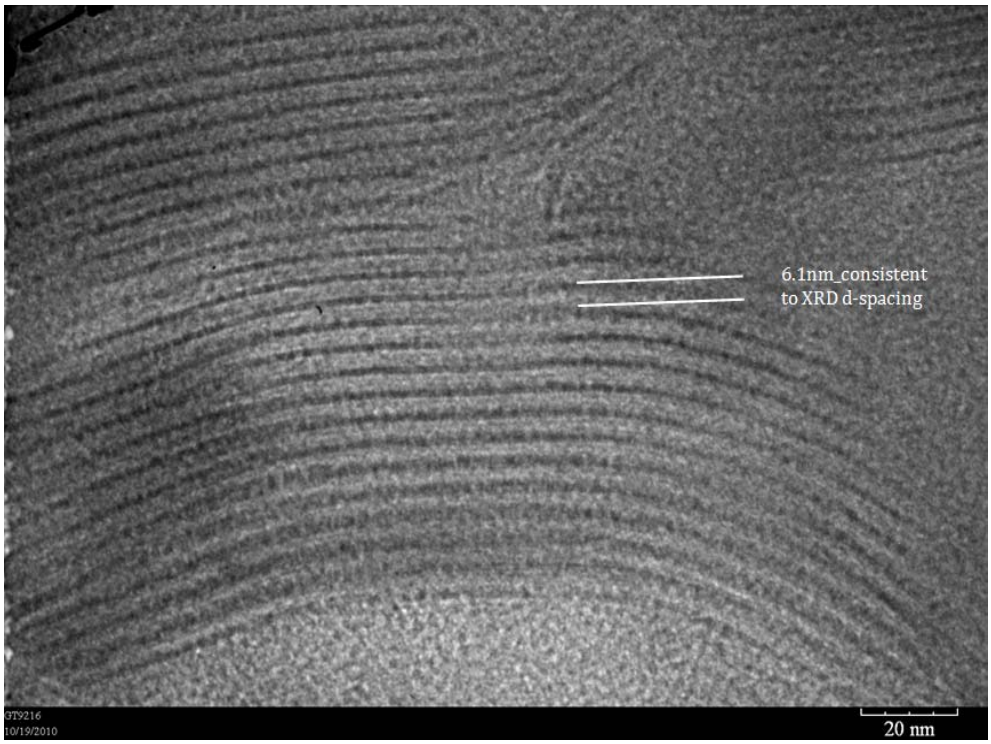

Figure 4-3. TEM Image of synthesized layered MFI.

The SEM image of Figure 4-4a shows the surface morphology of the 10 μm bare MFI particles. Figures 1b-1e show the surface morphologies of BMLM particles grown from the bare MFI particles. Layered MFI is seen to grow at the surface of conventional MFI, and the particle surface is highly roughened after the overgrowth of layered MFI. In Figures 1b-1d, it is seen that the surface morphology of the BMLM material can be controlled via the water concentration used in the synthesis. The thickness, extent, and roughness of the surface-grown layered MFI all increased upon decreasing the molar ratio of water from 16000 to 4000. Figure 1e captures different stages of growth of the layered MFI on bulk MFI. The layered MFI domains at various stages of growth all appeared to be morphologically aligned on the surface, hence suggesting an epitaxial

(lattice-matched) growth rather than a more random surface deposition and overgrowth process.

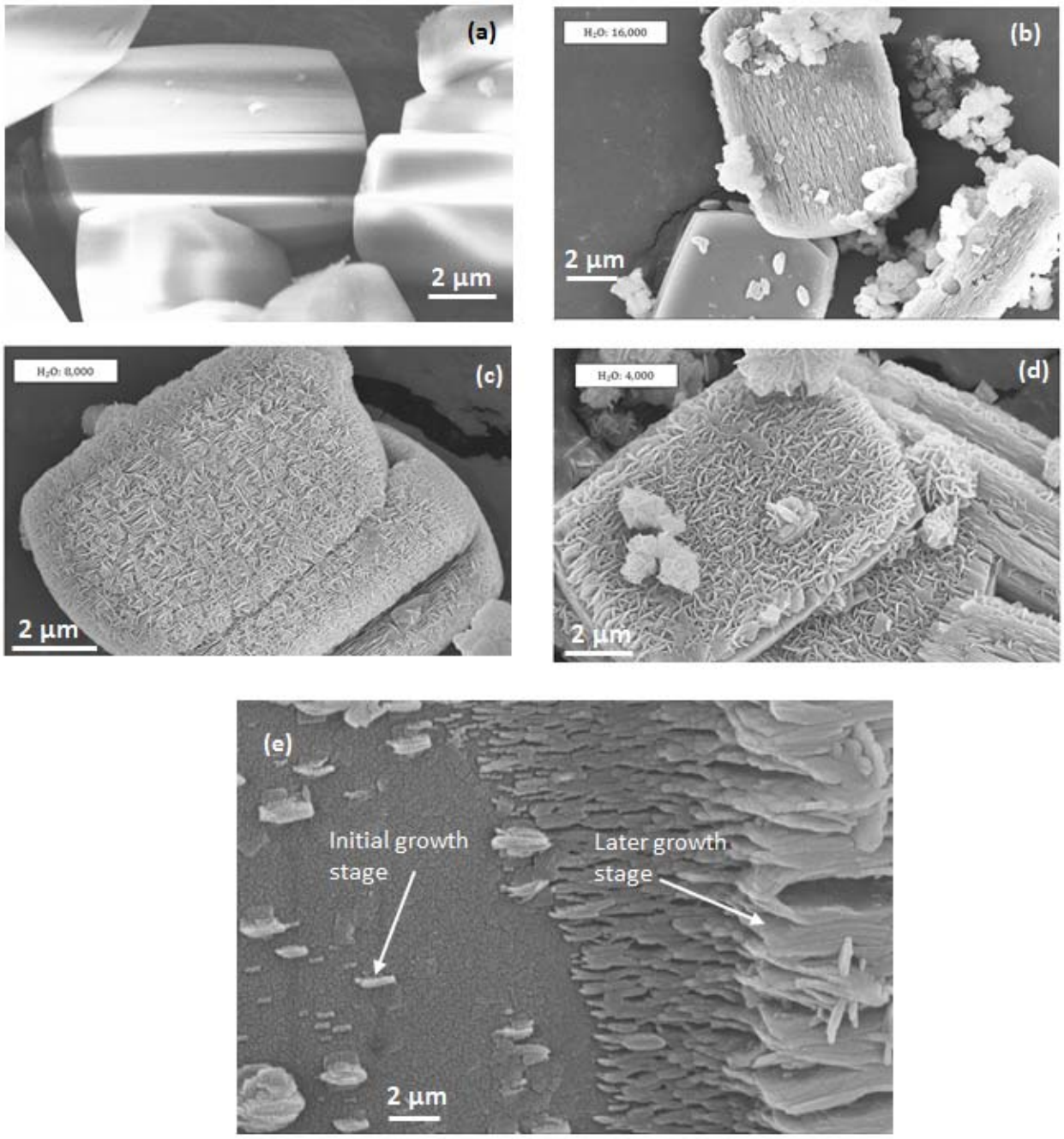

Figure 4-4. SEM images of (a) 10 µm Bare MFI and (b-e) BMLM particles at varying water concentrations in the synthesis.

Figure 4-5a shows XRD patterns of bulk MFI, layered MFI and the BMLM particles. The XRD pattern of the BMLM particles includes peaks from the bulk and layered MFI materials. Figure 4-5b shows the N_2 physisorption isotherms and calculated *t*-plot external surface areas of bare MFI and BMLM particles. As expected from the highly roughened surface morphology of the BMLM particles in Figure 4-4, the mesoporosity and calculated external surface area of BMLM particles are considerably larger than in bare MFI. Depending on the water content of the reaction gel, the calculated external surface areas ranged from 140-308 m^2/g. Based on SEM and N_2 physisorption measurements, it is found that a water molar content of 8000 in the reaction gel gives the maximum roughness and external surface area.

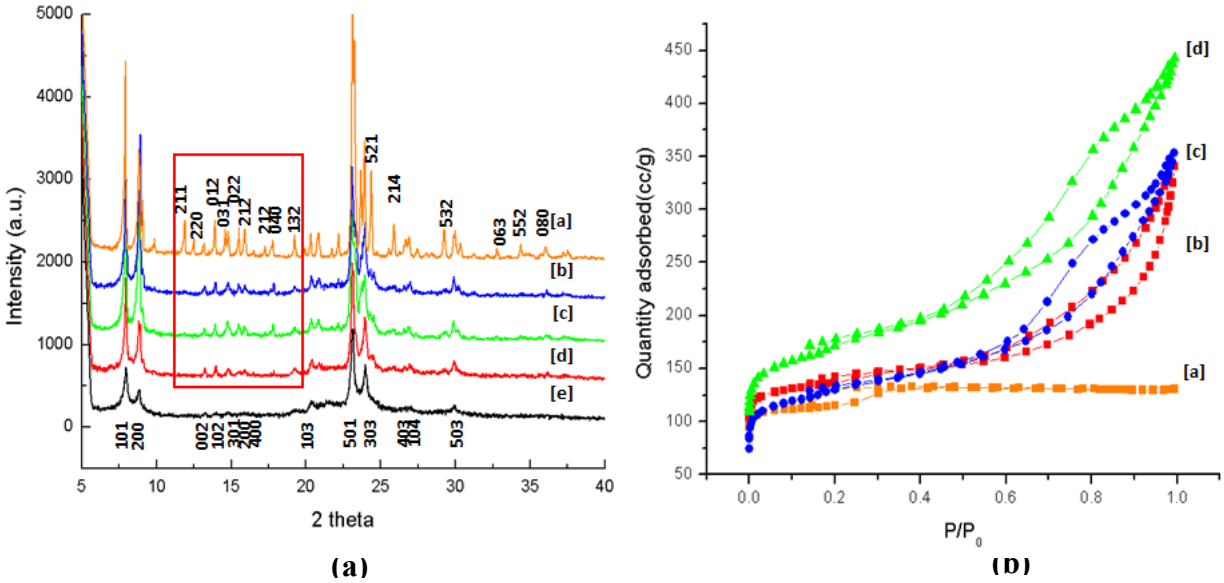

Figure 4-5. (a) XRD patterns of [a] Bulk MFI; [b] BMLM; H_2O contents: 16,000 [c] BMLM; 8,000 [d] BMLM; 4,000 [e] Pure Layered MFI; and (b) N_2 physisorption data of [a] Bulk MFI; External surface area: $90 m^2/g$ [b] BMLM 4,000; 140 m^2/g [c] BMLM 16,000; 236 m^2/g [d] BMLM 8,000; 308 m^2/g.

The large (10 μm) BMLM particles were used to optimize the synthesis method, but have limitations in their application. Therefore, we extended the BMLM synthesis technique to 300 nm bulk MFI particles. A water content of 8000 was used. Figures 4-6a~6c show SEM images of the bulk MFI and BMLM particles. Layered MFI was successfully grown on the surface of bulk MFI, and the surface morphology was highly roughened. Figure 4-6d shows the N_2 physisorption characterization, corroborating the increase in surface roughness and external surface areas.

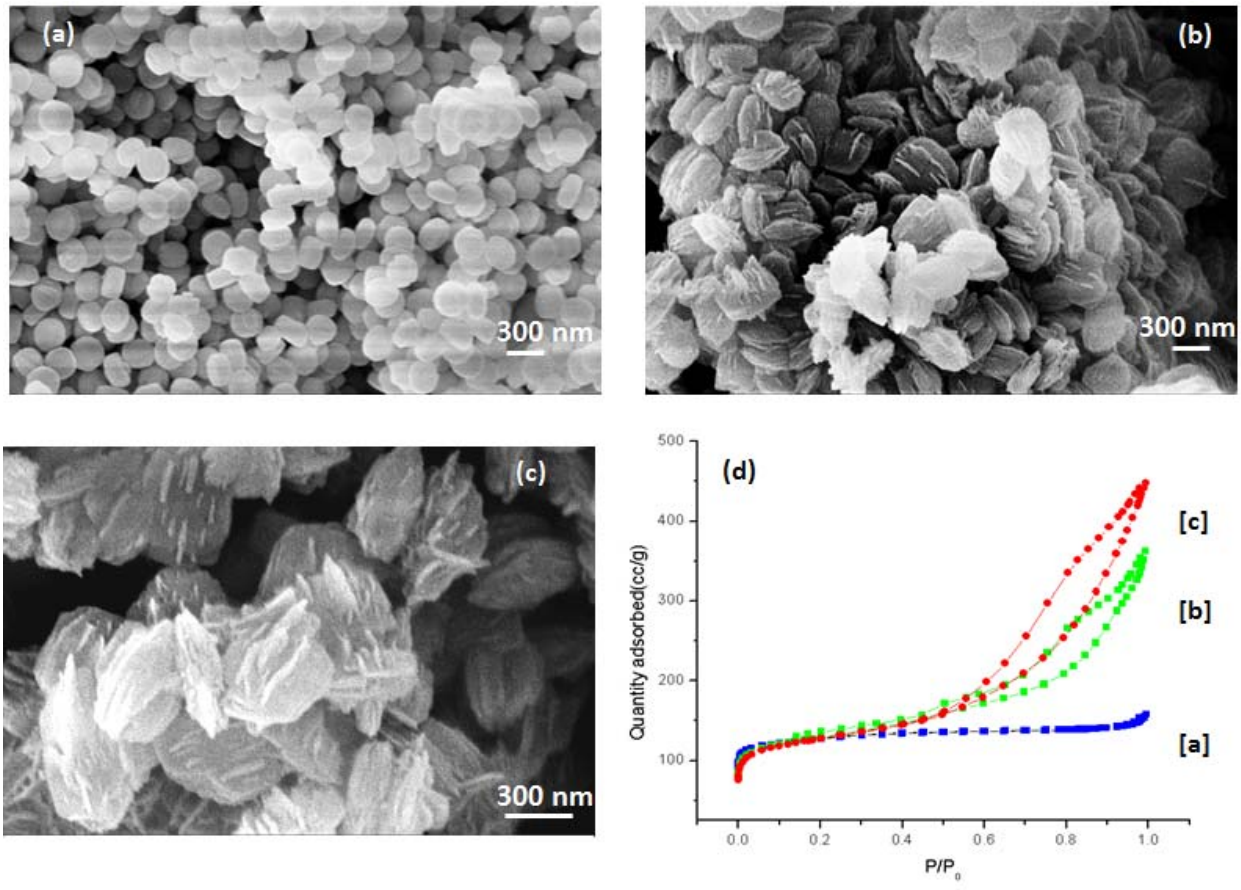

Figure 4-6. SEM images of (a) 300 nm bulk MFI; (b),(c) BMLM particles; and (d) N_2-physisorption data of [a] 300nm bulk MFI; External surface area=131 m^2/g [b] BMLM; 200 m^2/g [c] Pure layered MFI; 205 m^2/g.

Figure 4-7 shows thermogravimetric traces of as-made BMLM particles, bulk MFI, and layered MFI. The organic contents of bare MFI and layered MFI were measured to be 14% and 41%, respectively, whereas the organic loading of BMLM particles was measured to 31%. Based upon the known contents of the respective organic SDAs in bare and layered MFI, the mass fraction of bulk MFI in BMLM particles was calculated to be 37%. The density of bulk calcined MFI is known to be 1.73 g/cm^3, and 2.05 g/cm^3 before calcination.[152] The density of as-made layered MFI is 1.544 g/cm^3. Based upon these densities, the volume fraction of bulk MFI in BMLM particles is calculated to be 30.7 %. Hence, the average thickness of layered MFI on the surface of bulk MFI was calculated to be approximately 72 nm. The resulting overall average BMLM particle size of about 444 nm is comparable to the particle sizes seen in Figure 4-6.

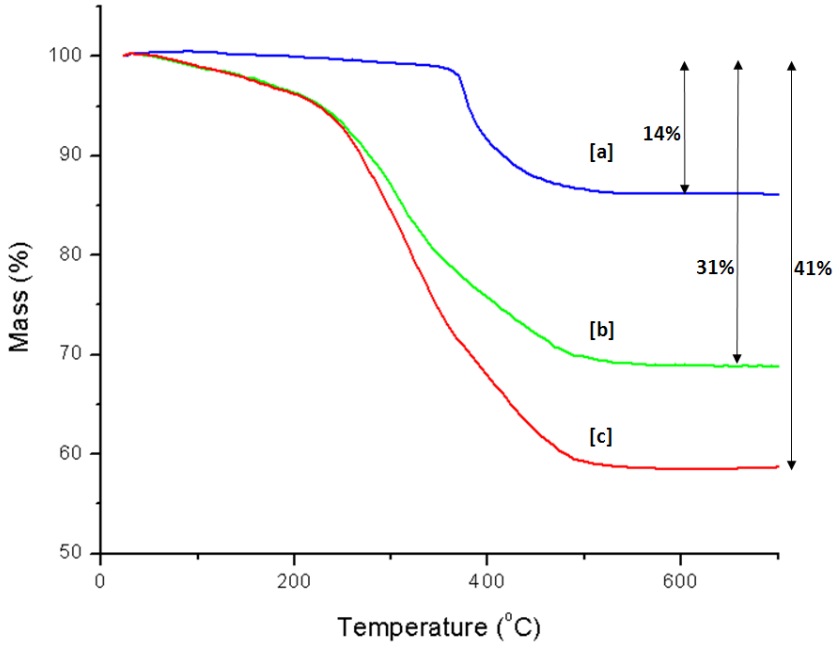

Figure 4-7. TGA analysis of [a] 300 nm Bulk MFI [b] BMLM [c] pure layered MFI.

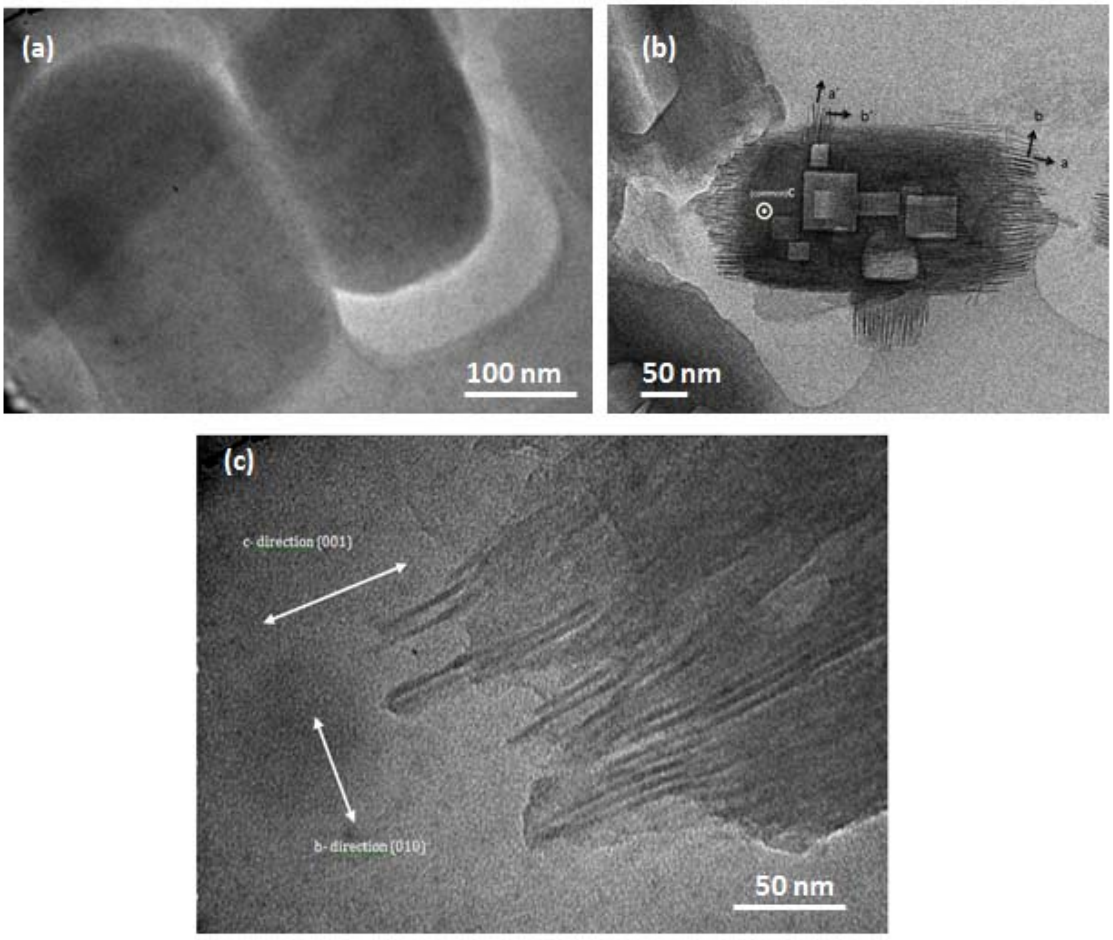

Figure 4-8. Low-resolution TEM images of BMLM particles.

4.3.2. Epitaxial growth of layered MFI in BMLM particles

The low-resolution TEM images in Figure 4-8 show the cross-sectional morphology of 300 nm BMLM particles. While bare MFI shows a smooth edge (Figure 4-8a), the BMLM particles clearly show the growth of layered MFI at the surface of the bulk MFI particle. Furthermore, it is clear that the layered MFI grows in all the three orthogonal crystallographic directions, consistent with Figure 4-6. The magnified image in Figure 4-8c demonstrates the high roughening of the MFI particle edge. One additional

interesting observation in Figure 4-8b is the presence of well-defined rectangular "holes". This is due to selective etching of silica from the bulk MFI crystal during growth of the layered MFI.

Scheme 4-1. BMLM morphology in three different crystal growth directions: **(a)** Type 1: *c*-directional, **(b)** Type 2: *a*-directional, and (c) Type 3: *b*-directional growth.

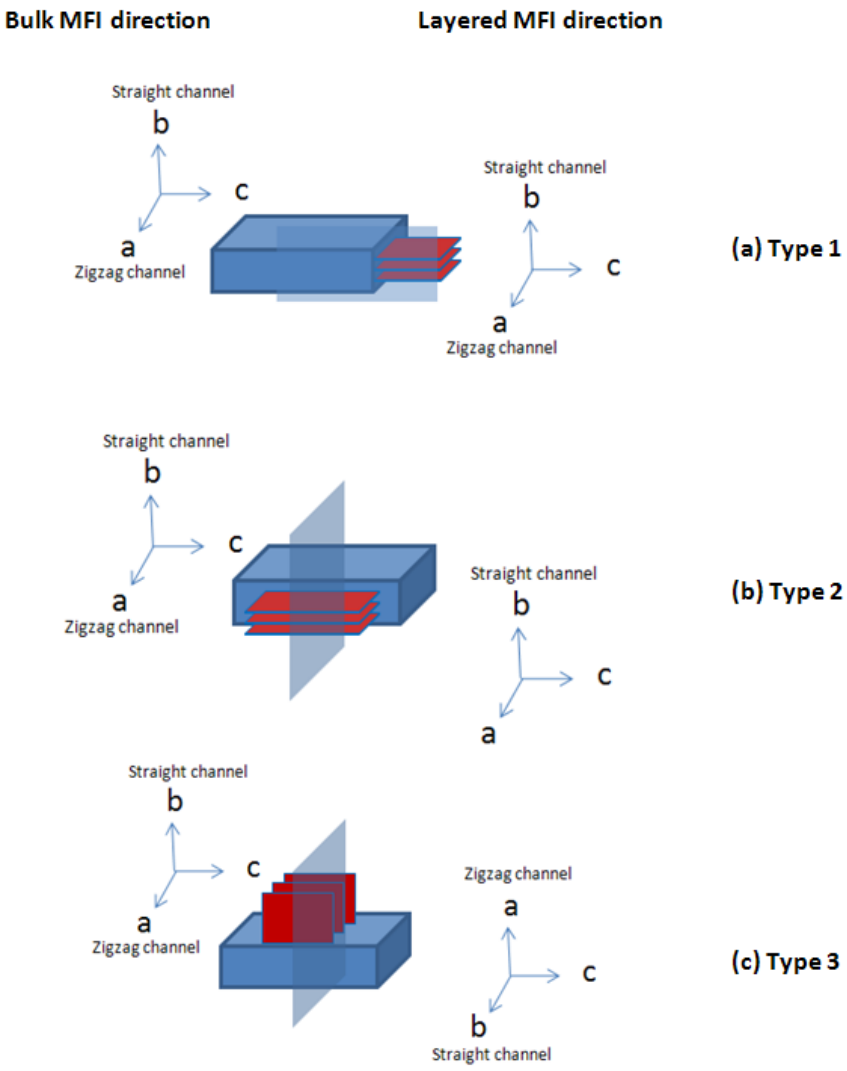

A detailed HRTEM analysis was performed to determine if the BMLM particles represent an epitaxially grown material. Epitaxial growth can be defined as the growth of a crystalline overlayer on another crystalline substrate, with lattice matching at the interface between the two phases. In this case, it is necessary that the crystal and pore structure of the layered MFI overgrowth be aligned with the structure of the bulk MFI substrate at the interface of the two phases. Scheme 1 shows the three possible crystal growth directions of layered MFI on bulk MFI as conjectured from the SEM images. As shown later in this report, Type 1 and 2 are homoepitaxial growths in which the bulk MFI substrate and layered MFI overgrowth are along a common crystal direction. However, Type 3 is a heteroepitaxial growth (or rotational overgrowth) involving twinning of the crystal directions of bulk and layered MFI.

Figures 4-9~11 show HRTEM images elucidating the crystal structure at the interface of BMLM particles. In all the three crystal growth directions represented in these Figures, both the pore structures and crystal structures of bulk MFI and layered MFI were exactly aligned, thereby representing the epitaxial growth of layered MFI at the surface of bulk MFI. The MFI pore size of 5.5 Å is clearly seen, and the pore direction in the bulk MFI region could be assigned *via* electron diffraction (ED) patterns after Fast Fourier transform (FFT) of the TEM images. Figure 4-9 shows the Type 1 (*c*-direction) crystal growth of layered MFI, represented in Scheme 1a. The electron diffraction spots of the bulk MFI region (blue square) after FFT is indexed in the inset. The diffraction spots coincide with the actual ED pattern of bulk MFI[52] and show that the structure is being viewed down the *a*-direction pores. The magnified interfacial region in Figure 4-9b

shows the continuity of the pore structure, as depicted by the Type 1 epitaxial growth model in Figure 4-9c.

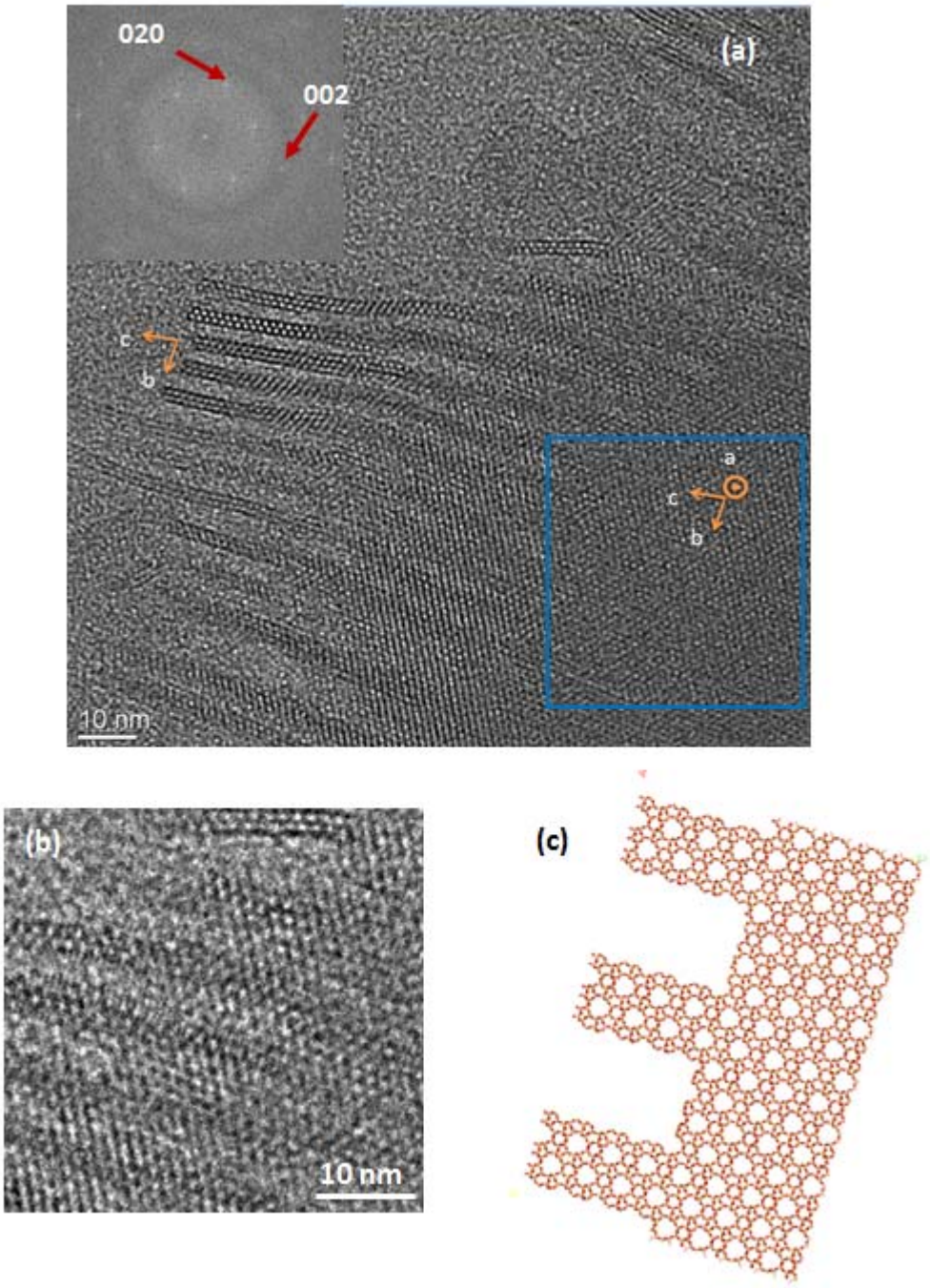

Figure 4-9. HRTEM analysis of BMLM epitaxial growth (Type 1, *c*-direction growth).

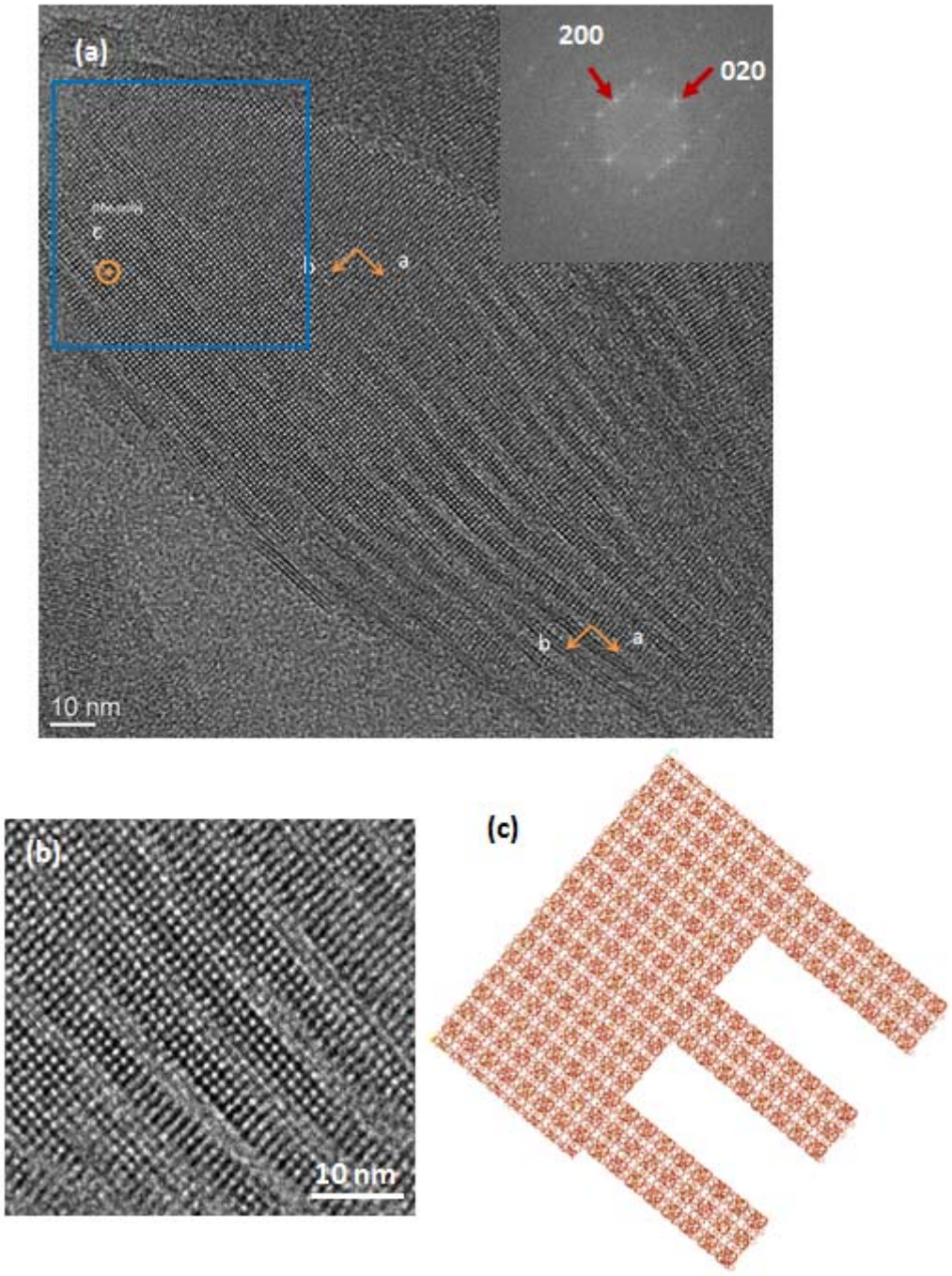

Figure 4-10. HRTEM analysis of BMLM epitaxial growth (Type 2, *a*-direction growth).

Figure 4-10 shows the interface of the Type 2 (*a*-direction) crystal growth represented in Scheme 4-1b. The diffraction pattern of conventional MFI region after

FFT processing coincides with that of the *c*-directional MFI pore structure, due to the indexed (200) and (020) diffraction spots. The magnified pore structure in Figure 4-10b is used to obtain the Type 2 epitaxial growth model shown in Figure 4-10c.

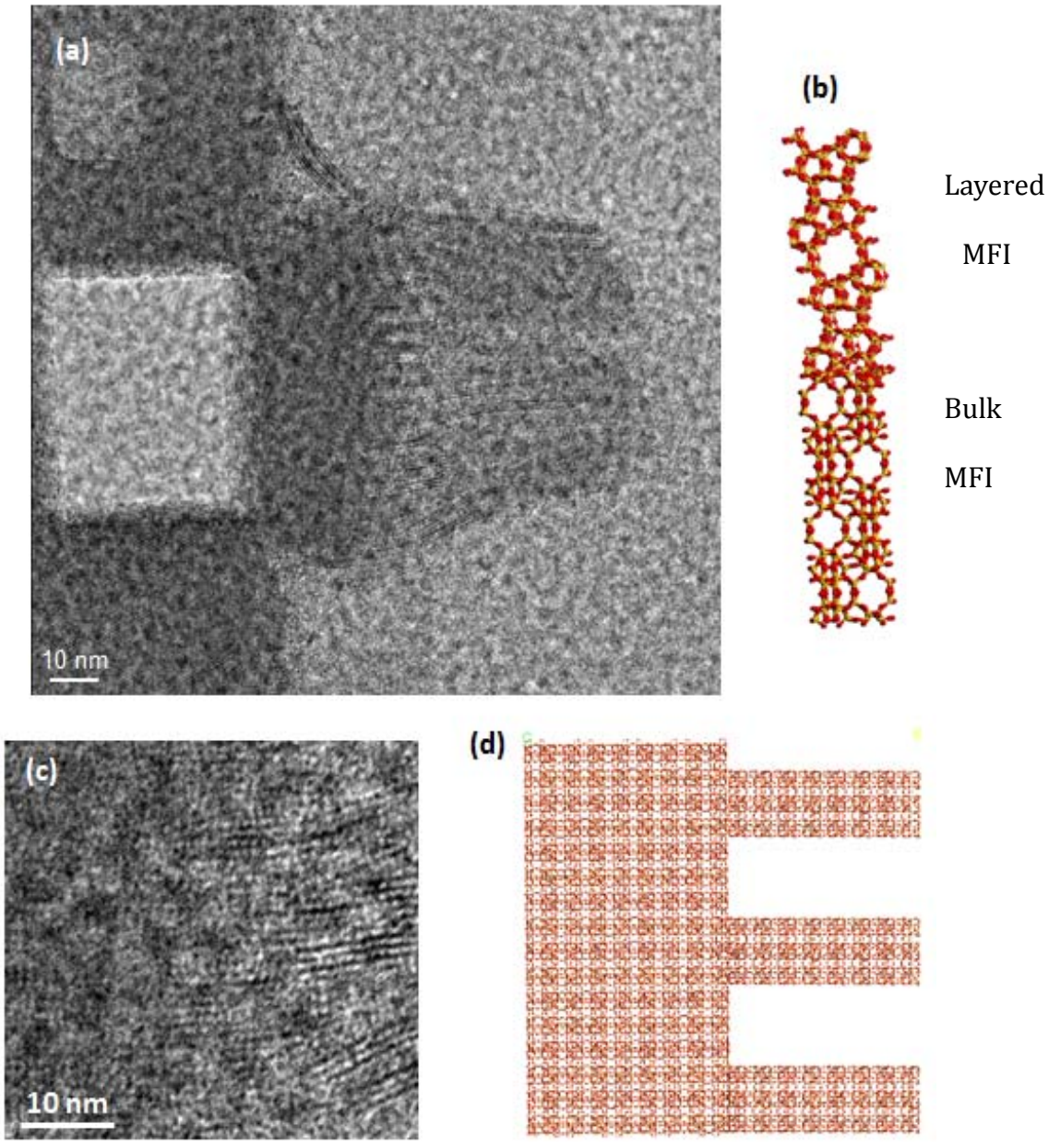

Figure 4-11. HRTEM analysis of BMLM epitaxial growth (Type 3, *b*-direction growth).

Figure 4-11 shows the interface of the Type 3 *b*-directional crystal growth case represented in Scheme 4-1c. In this case, a homoepitaxial growth is not possible, and the crystal direction of layered MFI is twinned with respect to that of the bulk MFI substrate (Figures 4-11b and 4-11d). This rotational overgrowth occurs because the *b*-direction of layered MFI is determined by the alignment of the C_{22} long-chain hydrocarbon moiety of the SDA. However, the alignment of the C_{22} chains is perpendicular to the *b*-direction of bulk MFI. The heteroepitaxial growth hence likely occurs by a 90° rotation or twinning of the overgrown layer with respect to the substrate. Heteroepitaxial growths, as in the present BMLM Type 3 case, are expected to be thermodynamically less favorable than homoepitaxial growths. It was found that the incidence of the Type 3 growth was much rarer than the other two (homoepitaxial) growths. Due to the rarity of finding this type of growth, and the fact that there is no clearly defined pore structure available as a guideline for interpreting the HRTEM images (Figure 4-11d), it proved difficult to obtain a complete characterization of this growth direction. In general, the connectivity of rotational overgrowths in the MFI system is not fully resolved yet. In the case of pure layered MFI, Zhang et al. have suggested the possible connectivities of layered MFI after repetitive branching based upon a hypothesis of their connection by a needle-like MEL domain.[153] Detailed atomic structures of various MFI crystal intergrowth defects have also been suggested.[154]

4.3.3. Fabrication and characterization of composite membranes

The BMLM particles were incorporated in Matrimid®, a well-known polyimide membrane material for gas separation applications. The particle/polymer interfacial adhesion in such composite/hybrid membrane materials is a key determinant of the separation performance. The highly roughened surface of BMLM particles is hypothesized to provide a much larger 'external' surface area than bare MFI,[23] and also would allow penetration of the polymer chains into the mesopores between the layered MFI sheets; thereby allowing much better adhesion than bare MFI. Furthermore, the roughened surfaces have a micropore structure similar to that of the bulk MFI, thereby allowing selective molecular transport through the interfaces. Figure 4-12 shows cross-sectional images of the BMLM/Matrimid and bare MFI/Matrimid membranes. To clearly observe the differences in adhesion properties, the larger (10 μm) MFI particles are used. The bare MFI particles (Figure 4-12a) adhere very poorly to the polymer, leading to macrovoids (~500 nm) at the interfaces. However, the BMLM particles (Figure 4-12b) show excellent adhesion to the polymer matrix, and no significant voids were detected at the interface. The magnified image at the interfacial region (Figure 4-12c) shows clear adhesion beween layered MFI and Matrimid. The SEM images indicate penetration of the polymer into the mesoporous spaces between the layered MFI sheets. Figure 4-13 shows the cross-sectional images of membranes prepared with 300 nm MFI and BMLM particles. In the low-magnification SEM images of Figures 4-13a~b, the conventional MFI particles were seen to be highly aggregated and poorly adhered to the polymer, whereas the BMLM particles were better-dispersed and well-adhered to the polymer. In the magnified SEM images (Figures 4-13c~d), it is clearly seen that the BMLM particles

showed good adhesion to Matrimid whereas the bare MFI particles formed macrovoids around aggregated particles.

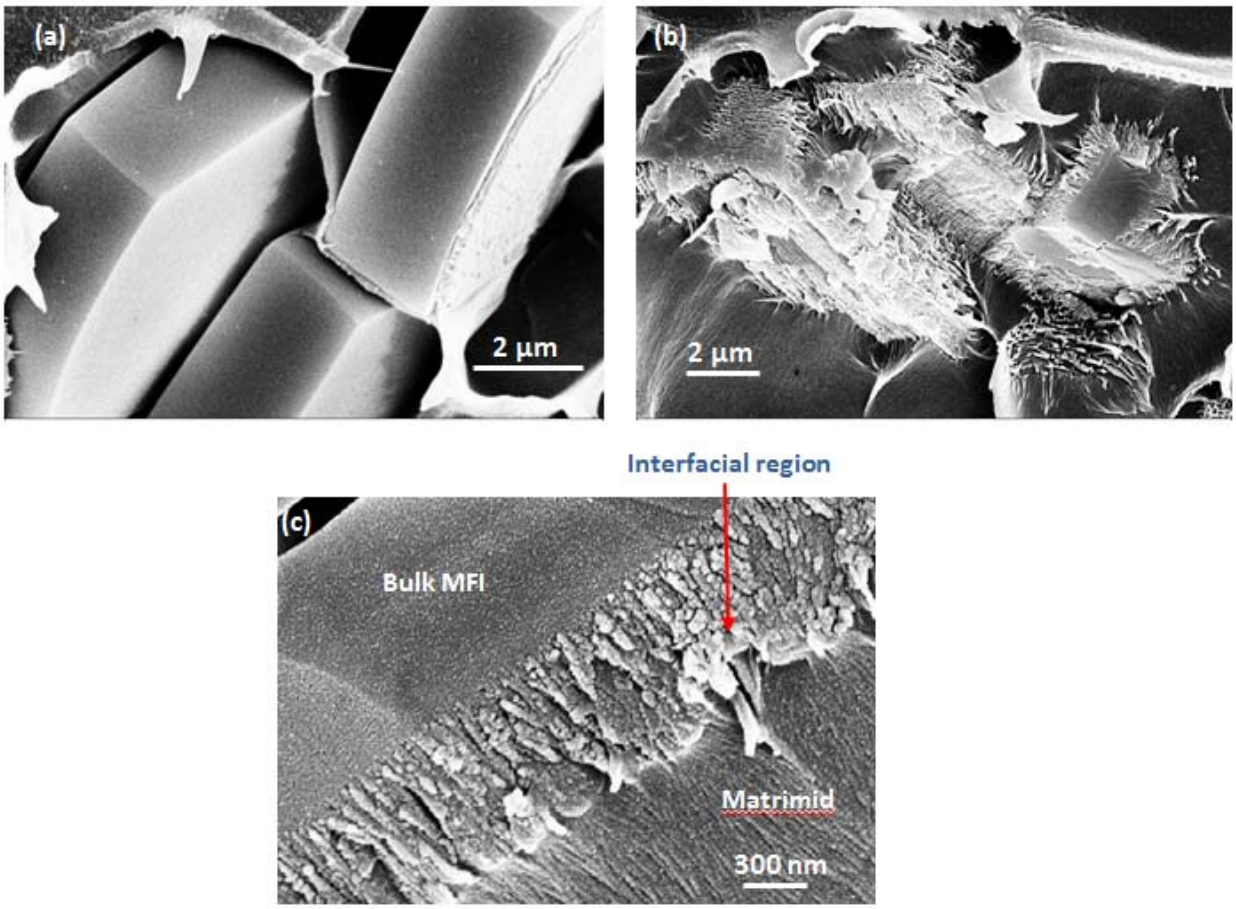

Figure 4-12. SEM cross-section images of zeolite/Matrimid® composite membranes made with (a) bulk MFI, and (b,c) BMLM materials. The crystal size of the bulk MFI was 10 µm.

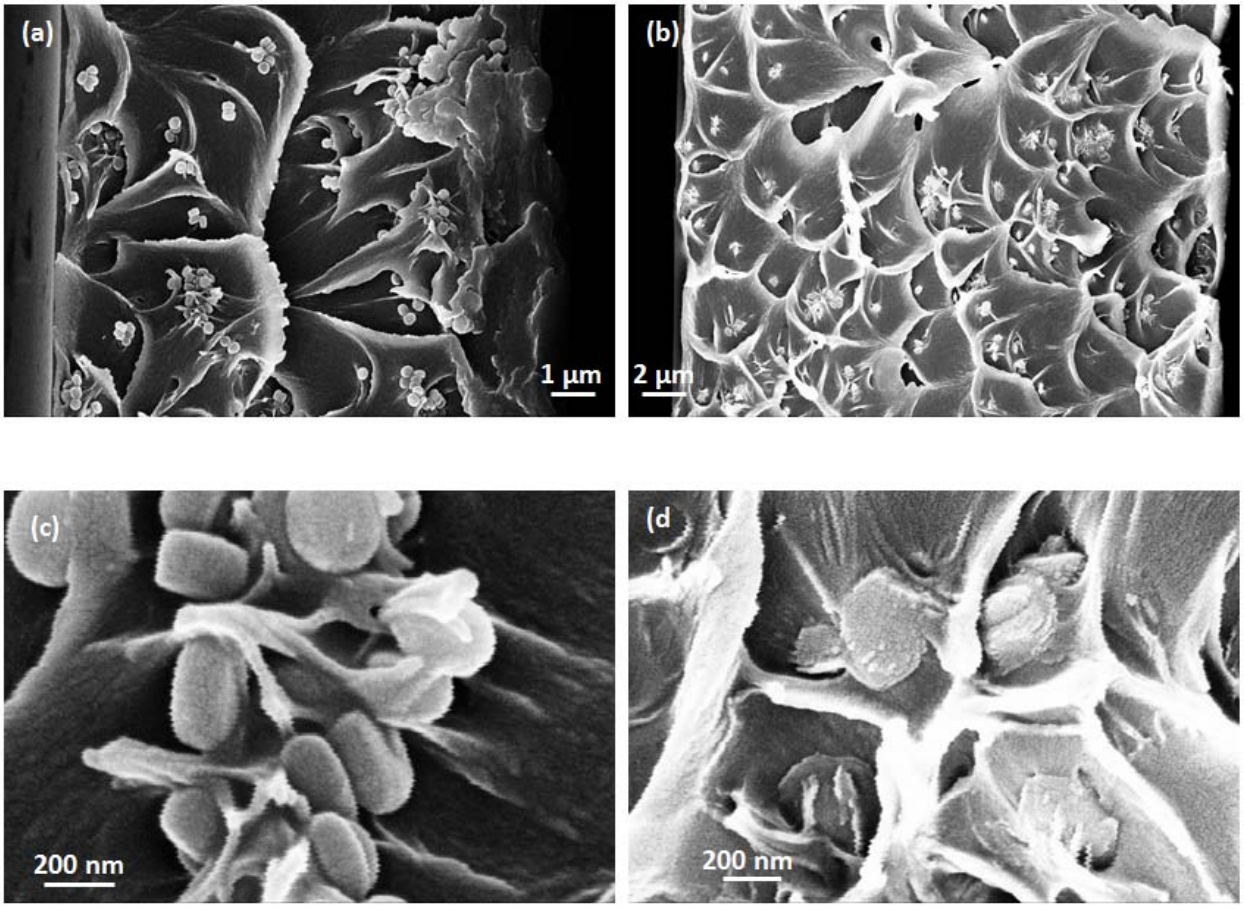

Figure 4-13. SEM cross-section images of zeolite/Matrimid® composite membranes made with (a,c) bare MFI, and (b,d) BMLM materials. The crystal size of the bulk MFI was 300 nm.

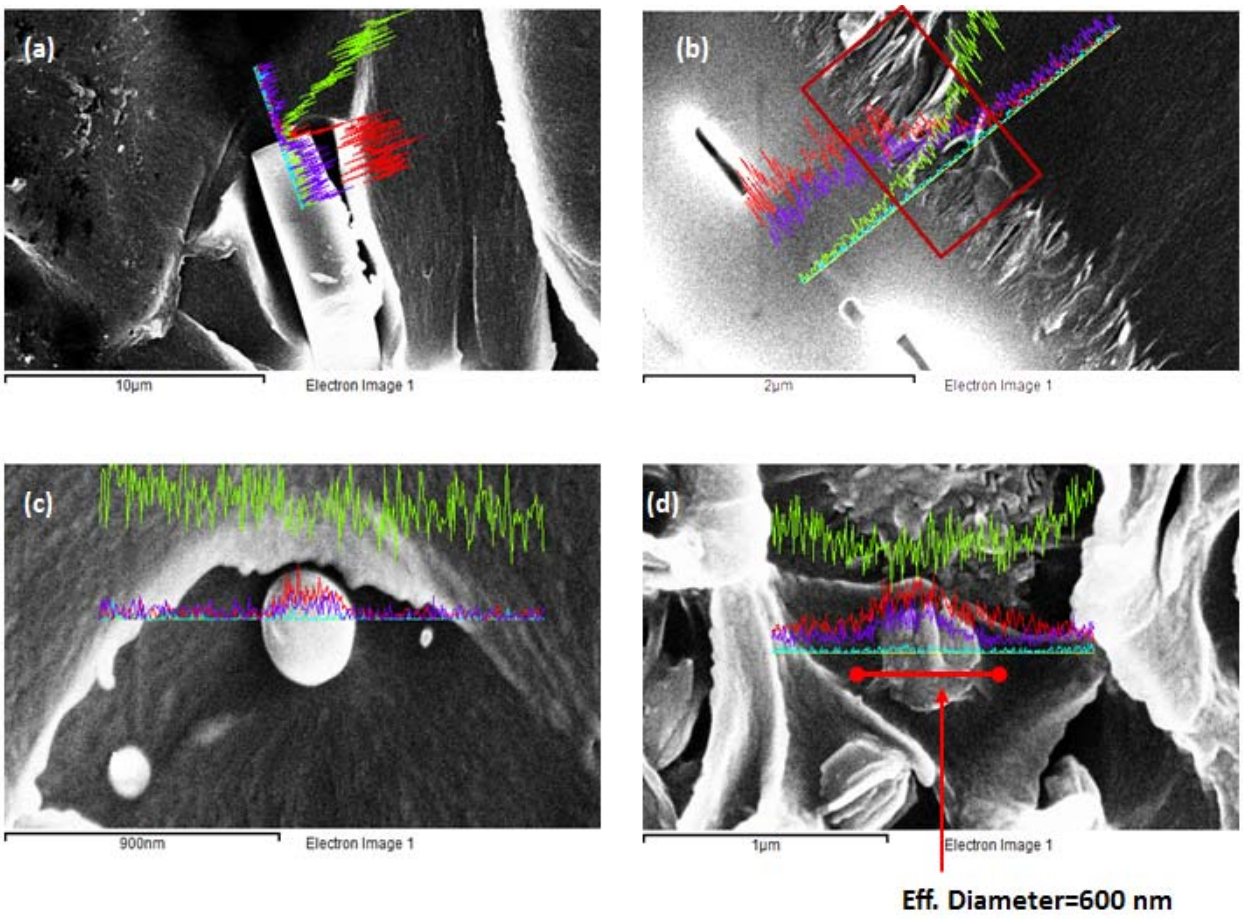

Figure 4-14. EDX compositional analysis of zeolite/Matrimid® composite membranes made with (a,c) bare MFI, and (b,d) BMLM materials. The crystal sizes of the bulk MFI were 10 µm (a,c) or 300 nm (b,d). Red: Si, Purple: O, Green: C, Turquoise: N.

Figure 4-14 shows the SEM-EDX carbon and silicon compositional analyses at the BMLM/polymer interfacial region. In contrast with the membranes containing bare MFI particles (Figures 4-14a, c), the membranes containing BMLM particles (Figures 4-14b, d) clearly show the interpenetration of the carbon and silicon profiles. Additionally, in Figure 4-14d the silicon profile around the particle can be used to estimate the effective diameter of BMLM particles in the composite membrane. The EDX-estimated

effective diameter of BMLM particles is about 600 nm, which is twice as large as the diameter of the underlying bulk MFI particle (300 nm). Hence, the volume of the interfacial region (including both of layered MFI and polymer) is about 7 times larger than the volume of the bulk MFI region, and occupies 87.5% of the total particle volume.

4.3.4. CO_2 and CH_4 gas permeation

Figure 4-15a depicts CO_2 permeability and and CO_2/CH_4 single-component selectivity of Matrimid membranes incorporating 300 nm bare MFI and the corresponding BMLM material. In the bare MFI composite membranes, the CO_2/CH_4 selectivity was significantly decreased below that of the pure Matrimid membrane. As confirmed from the foregoing discussion, the poor adhesion between the bare MFI particles and the polymer resulted in the formation of macrovoids, which are possibly also interconnected to allow a continuous non-selective permeation pathway through the membrane.[152] On the other hand, the BMLM composite membrane showed better CO_2/CH_4 separation performance than the conventional MFI composite membrane. The introduction of the highly permeable MFI particles has a large effect on the membrane permeability, and the selectivity is only slightly decreased due to the lower CO_2/CH_4 selectivity of MFI in comparison to Matrimid. This improved separation performance is due to the tight adherence of the BMLM particles to the polymer due to infiltration of the polymer into the mesoporous spaces between the layered MFI sheets.

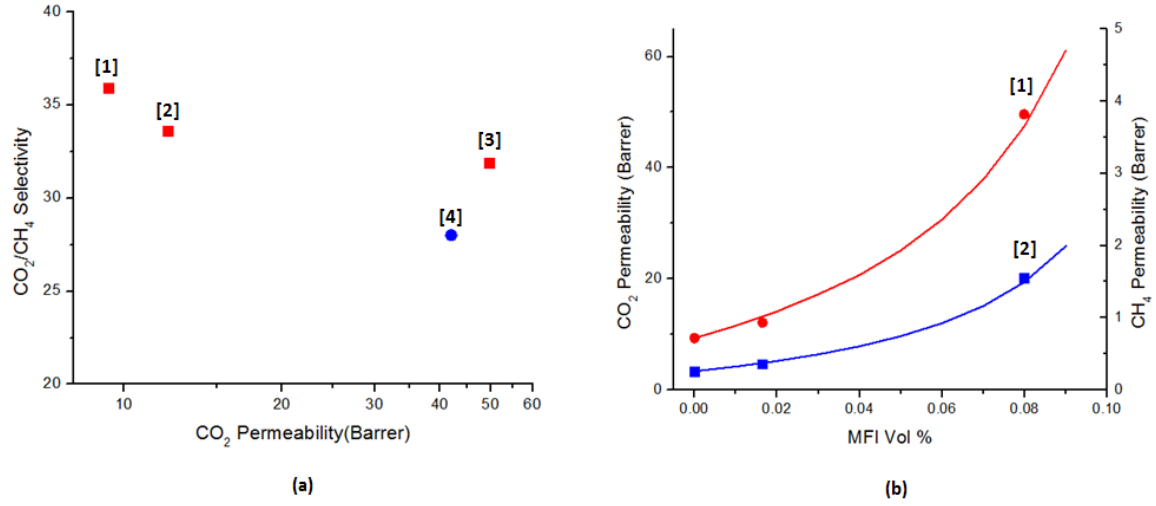

Figure 4-15. (a) Gas permeation data from [1] bare Matrimid, [2] 5wt% BMLM composite, [3] 24wt% BMLM composite, and [4] 20 wt% bulk MFI composite membranes, at 35 ^{o}C and 65 psi pressure differential; (b) [1] CO_2 and [2] CH_4 permeabilities (symbols) and fitted prediction by modified Maxwell equations (solid curves).

To analyze the dependence of the permeation behavior on the membrane microstructure in more detail, the gas permeation data were fitted to the modified Maxwell equation. In particular, our objective was to estimate the effective particle size and the permeability of the interfacial region. The modified Maxwell equations are given in equations 4-1~3 and consider the membrane to have three structural components[15]: the continuous phase (polymer), the bulk dispersed phase (bulk MFI), and an interfacial phase (which in the case of the bare MFI/Matrimid membrane is a void, and in the case of the BMLM/Matrimid membrane is the inorganic/polymer interfacial composite region found in Figures 4-13,14). In calculating the effective permeability of the composite membrane, the properties of the interface are represented by the two dimensionless parameters β (ratio of the thickness of the interfacial layer to the radius of the underlying

bulk MFI substrate) and γ (ratio of the permeabilities of the interfacial layer and the underlying bulk MFI substrate). The properties of the continuous (polymer) and dispersed (bulk MFI) phases are known from the literature. We used CO_2 (CH_4) permeabilities of 9.33 (0.26) Barrers for Matrimid and 8,960 (4,032) Barrers for bulk MFI.[155]

For the macrovoids around the bare MFI particles, the gas permeabilities will clearly be close to the Knudsen values of 1,165,849 (1,985,158) Barrers and therefore we have γ = 130 (479) for CO_2 (CH_4) in this case. However, the modified Maxwell equations (4-1~3) failed to correctly fit the permeability of bare MFI composite membranes for any physically reasonable values of β and γ. It was therefore concluded that in addition to the individual macrovoids present around the bare MFI particles, there is some interconnection of these voids leading to a small but continuous leakage path through the membrane. This feature was added in the form of the leakage fraction χ (Equation 4-4). The values of β and χ were estimated by least squares fitting. The fitted value of χ was 2×10^{-7}. This very small leakage fraction, in addition to the individual macrovoids, is highly deleterious to the separation performance as seen in Figure 4-15. The fitted value of β was 0.53. This is quite comparable to the SEM observations, which indicate that the thicknesses of the macrovoids are of the same order of magnitude as the bare MFI particle radius.

$$P_{mm} = P_C \frac{P_d + 2P_c - 2\varphi_d(P_c - P_d)}{P_d + 2P_c + \varphi_d(P_c - P_d)} \quad (4\text{-}1)$$

$$P_{eff} = P_d \frac{[2(1-\gamma) + (1+\beta)^3(1+2\gamma)]\gamma}{-(1-\gamma) + (1+\beta)^3(1+2\gamma)}; \quad \gamma = \frac{P_I}{P_d}; \ \beta = \frac{h}{r} \quad (4\text{-}2)$$

$$P_{3mm} = P_C \frac{P_{eff} + 2P_c - 2(1+\beta)^3\varphi_d(P_c - P_{eff})}{P_{eff} + 2P_c + (1+\beta)^3\varphi_d(P_c - P_{eff})} \quad (4\text{-}3)$$

$$P_{\text{Bare MFI Composite}} = (1-\chi)P_{3mm} + \chi P_{Knudsen}; \ \chi = \text{leaking fraction} \quad (4\text{-}4)$$

where, Pd, Pc, and P_I are the permeabilities of the gas molecule through the dispersed bulk particle, the continuous polymer phase, and the interfacial layer between polymer and particle, respectively. φ_d is the volume fraction of dispersed particles, *r* is the radius of the dispersed bulk particle, and *h* is the thickness of the interfacial layer.

In the BMLM/ Matrimid composite membranes, there were no macrovoids at the interfacial region, and the polymer chain infiltrate into the mesopores of the layered MFI eptiaxially grown at the surface of bare MFI. In this case, the modified Maxwell equation could be applied to estimate the interfacial parameters β and γ. While β is a structural parameter, γ is a permeability parameter and hence differs for the two gases. As the result of the fitting calculations, we obtain the interfacial permeabilities $P_{I, CO2}$ ($P_{I, CH4}$) = 434 (216) Barrers. The interfacial layer is constituted of layered MFI and infiltrated polymer. As expected from such an interfacial layer, the gas permeabilities are intermediate between bulk MFI (several thousand Barrers) and the polymer matrix (< 10 Barrer). The fitted β value was estimated as 0.97, which agrees very well with the value of 1.0 obtained from the EDX analysis in Figure 4-14. Figures 4-15b shows the

individual measured permeabilities of CO_2 and CH_4 in the BMLM/Matrimid composite membranes, along with the modified Maxwell equation predictions using the best fit parameters. This consistent agreement of the gas permeabilities over the range of bulk MFI volume fractions, as well as the excellent agreement of the effective interface thickness, further confirms the good quality of the BMLM/Matrimid composite membranes. The increase in membrane permeability (more than a factor of 5 at 8 vol% loading) upon incorporation of the nanoporous, high-flux BMLM material is much larger than that obtained by incorporating the same loading of nonporous (e.g., TiO_2) nanoparticles into Matrimid (a factor of 1.5-1.7). The latter effect is hypothesized as being caused by disruption of polymer chain packing near the interfaces.[17,156]

4.4. Conclusions

A new type of hybrid zeolitic material, namely an overgrowth of layered MFI over a bulk MFI substrate, has been shown. Detailed HRTEM analysis shows epitaxial growth of layered MFI on the bulk MFI substrate in at least two, and possibly all three, principal crystallographic directions. In this "bulk-MFI/layered-MFI (BMLM)" material, the layered MFI creates a large 'external surface area' and 'surface roughness'. The capability of epitaxially growing a layered zeolite on a conventional bulk zeolite creates the possibility of a new class of hybrid zeolitic materials whose properties can be rationally controlled by independently tuning the morphologies of the layered and bulk zeolitic components of the hybrid material. In one example application, we have shown that the highly roughened surface resulted in excellent adhesion to a dense glassy

polymer. BMLM/Matrimid composite membranes showed better gas permeation properties than bare MFI/Matrimid composite membranes, and the fit of the permeation data to the modified Maxwell model yielded physically reasonable values for the interface properties. The BMLM particles are interesting materials for application in molecular separation using composite/hybrid membranes, and may also have uses as catalytic materials after substituting some of the Si atoms with Al atoms.

CHAPTER 5: SYNTHESIS AND CHARACTERIZATION OF A LAYERED SILICOALUMINOPHOSPHATE (SAPO) MATERIAL

5.1. Introduction

Zeolites are important materials that are widely applied in separations and catalysis because of their shape/size-selective nanopores and large surface area of active sites.[138,139] However, they present limitations on the diffusion rates of larger molecules. To overcome the molecular diffusion limitations in zeolite materials and expand their applications to handling bulky molecules such as heavy hydrocarbons or biomolecules, several interesting developments have recently emerged, such as the synthesis of nano-sized zeolites[140,157] as well as layered and exfoliated (i.e., 2-D) zeolites.[42,43,45]

Another effective way to overcome diffusion limitation is to develop hierarchical zeolite-mesoporous hybrid materials.[141,142] The interconnected micropores and mesopores in the structure of hierarchical zeolites combine different advantages such as active acid sites in the micropores and fast diffusion paths through the mesopores.[143,144] While many top-down and bottom-up synthesis method have been attempted for developing these materials, the direct synthesis method using designed long-chain structure directing agents (SDAs) has shown particular promise. For example, ultrathin (2 nm) layered MFI materials have been obtained and are being developed for reaction and separation applications.[145] However, MFI is a "medium-pore" zeolite with 10MR (5.5Å) pores. My interest in this thesis is focused primarily on materials that can separate light

gases. Successful synthesis of small-pore layered nanoporous materials (equivalent, e.g., to zeolitic materials such as SAPO-34 or DDR) canlead to new applications in gas separation and membrane reactors.[158]

The silicoaluminophosphate zeolite SAPO-34 has the topology of chabazite (CHA), and is an attractive target material with 8MR pores of size ~3.8 Å. SAPO-34 membranes have been fabricated and applied to light gas separations such as CO_2/CH_4 or CO_2/N_2.[159-161] A previous attempt to synthesize a hierarchical SAPO-34 material used natural clay (kaolin) materials as the(Si, Al) source.[162] The resulting particles showed a clear hierarchical structure of SAPO-34, but may have limited application due to the high degree of crystal intergrowth.

I noted that the synthesis of SAPO-34 uses TEAOH as the structure directing agent, which is similar to TPAOH used as the SDA for MFI synthesis. I hypothesized that, as in the case of layered MFI synthesis, a long chain alkyl template (C_6-C_6-$C_{22}Br_2$) can be synthesized and used to crystallize layered porous SAPO materials. The quaternary ammonium cation may be used to generate pores in layered SAPO materials and the aligned C_{22} carbon chains will prevent crystal growth perpendicular to the layers. After the synthesis of my new layered SAPO material, detailed studies on its crystalline materials were performed to evaluate the morphology, elemental analysis, crystal structure, organic loading, and porosity.

5.2. Experimental Methods

5.2.1. Synthesis of conventional SAPO-34 and layered SAPO materials

The conventional SAPO-34 was synthesized as described in previous work. The molar composition of the reaction gel was $1Al_2O_3$: $1P_2O_5$: $0.32SiO_2$ 1TEAOH : 1.6DPA (dipropylamine): $52H_2O$. Typically, 3.92g of H_3PO_4(Aldrich) and 8.17g of Al(i-$C_3H_7O)_3$ (Aldrich) had been dissolved in 13.4 g of DI H_2O at room temperature and mixed for 3 hrs. Then 1.28g of Ludox solution (HS-40, Aldrich) has been added and mixed for another 3 hrs. Then 7.365 g of TEAOH (Aldrich) as template has been added followed by addition of 1.62 g of DPA(Aldrich) after 30 min. The reaction gel was aged for 4 days followed by 1 day reaction in 210°C rotation oven. The synthesis of layered SAPO materials has been designed by substituting long chain template to TEAOH and NaOH has been added to balance the pH value. The molar composition of the reaction gel was $1Al_2O_3$: $1P_2O_5$: $0.32SiO_2$ 0.2Template : 0.8DPA (dipropylamine): $52H_2O$: 0.2NaOH. The synthesis of the the long-chain diquaternary ammonium cation (C_{22}-N^+-C_6-N^+-C_6) as a structure-directing agent (SDA) was similar to the previously described method for MFI SDAs.[145]

5.2.2. Characterization

Scanning Electron Microscopy (SEM) of particles and membranes was performed with a JEOL LEO-1530 operating at 10 kV. Samples were gold-coated to prevent surface charging effects. Elemental analysis was performed by SEM-EDX. High Resolution TEM (HR-TEM) was performed on a FEI Tecnai G^2 F30 TEM at 300 kV. To show the cross-sectional image of particles, the particles were embedded in epoxy and sliced into

50-nm thin sections by a Leica EM UC6 Ultramicrotome equipped with a diamond knife. N_2 physisorption isotherms were obtained at 77 K with a Micrometrics Tristar II. The samples were degassed for 12 hrs at 150°C. Thermogravimetric analysis (TGA) and Differential scanning calorimetry (DSC) was performed using a Netzsch STA409. The scanning temperature was 30-900°C at a ramping rate of 10°C/min, under an N_2:O_2 stream flowing at 90:50 ml/min.

5.3. Results and Discussion

5.3.1. Synthesis of conventional SAPO-34 and Layered SAPO materials

Figure 5-1a shows the SEM image of synthesized conventional SAPO-34, whose morphology is consistent with previous reports.[160] However, the synthesized layered SAPO materials have very different morphology from conventional SAPO-34 materials. Specifically, in the Figures 5-1b-d, the layered SAPO material is found to consist of agglomerated platy structures. A similar difference has been shown in the previous reports of layered MFI synthesis.[54,145]

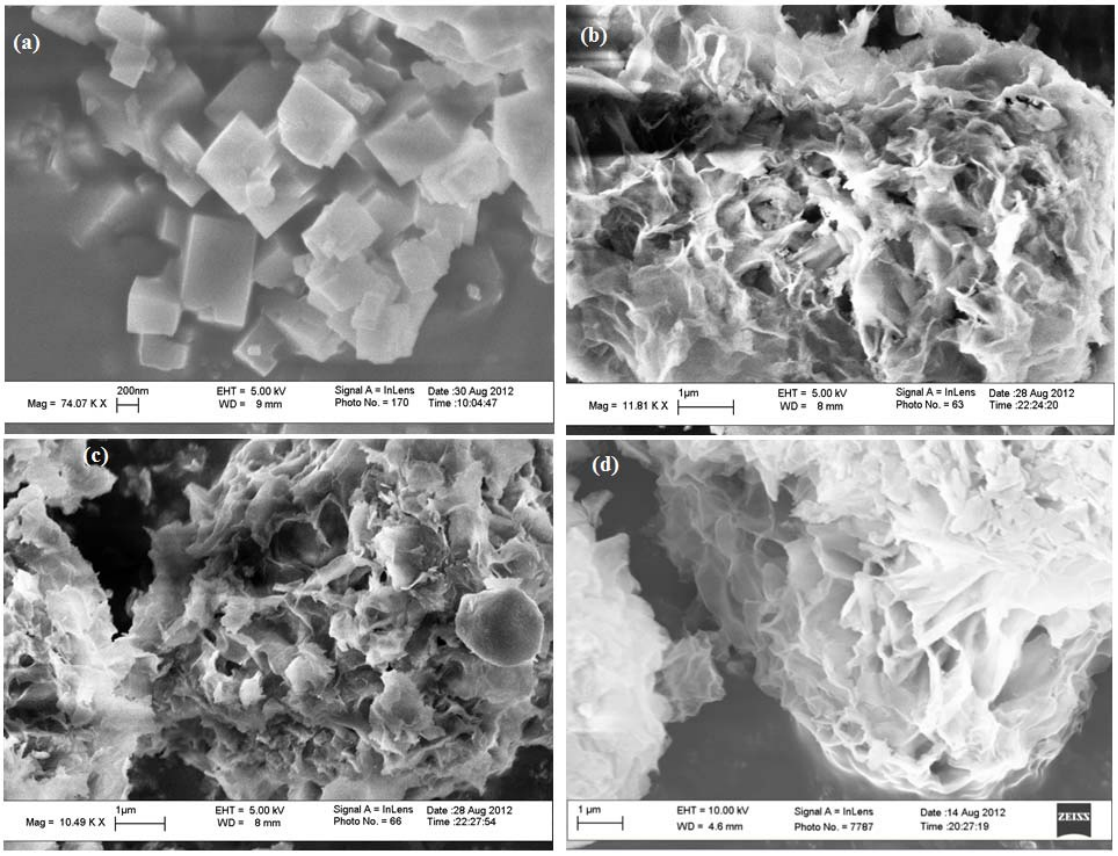

Figure 5-1 SEM images of (a) Conventional SAPO-34, and (b)-(d) Layered SAPO material.

Table 5-1. Elemental composition of Conventional SAPO-34 and Layered SAPO materials. (by SEM-EDX)

Atomic %	C	O	Al	Si	P
Conv. SAPO-34	34.55	47.5	9.32	2.26	6.37
		Only Al, Si, P	**52**	**13**	**36**
Layered SAPO	55.0	32.63	6.64	1.32	4.41
		Only Al, Si, P	**53**	**11**	**36**

Elemental analysis on conventional SAPO-34 and the layered SAPO material has been performed by SEM-EDX (Table 5-1). The same chemical composition (Si, Al, and P) were used in the reaction gel for the synthesis of both two materials, and the resultant materials have almost the same atomic compositions of Al, Si and P. However, the composition of carbon in the layered SAPO material is much higher (55%) than in conventional SAPO-34 (35%). This indicates that the layered SAPO material successfully incorporates the long-chain hydrocarbon template.

HR-TEM images (Figure 5-2) of the layered SAPO material clearly show the layered structure with uniform *d*-spacings. To show the cross-sectional image of synthesized layered SAPO materials, dried powder has been dispersed in epoxy resin and microtomed into thin slices (~50 nm). The low magnification TEM image in Figure 5-2a shows the typical morphology of the layered SAPO flakes, indicating their high aspect ratio. As seen in Figures 5-2b-c, we found regions with uniformly stacked layers as well as fully exfoliated layers. The interlayer spacings in the stacked areas has been clearly measured as 4 nm (Figure 5-2d), consistent with the XRD result shown later in Figure 5-5. A promising characteristic of the layered SAPO material appears to be the easy exfoliation and dispersion of single layers without the need for exfoliation processes such as high shear mixing or melt blending, earlier developed for AMH-3 and MFI. This easy exfoliation is possibly because there is not much twinned crystal growth among the layered SAPO crystals, a phenomenon quite different from layered MFI crystals.

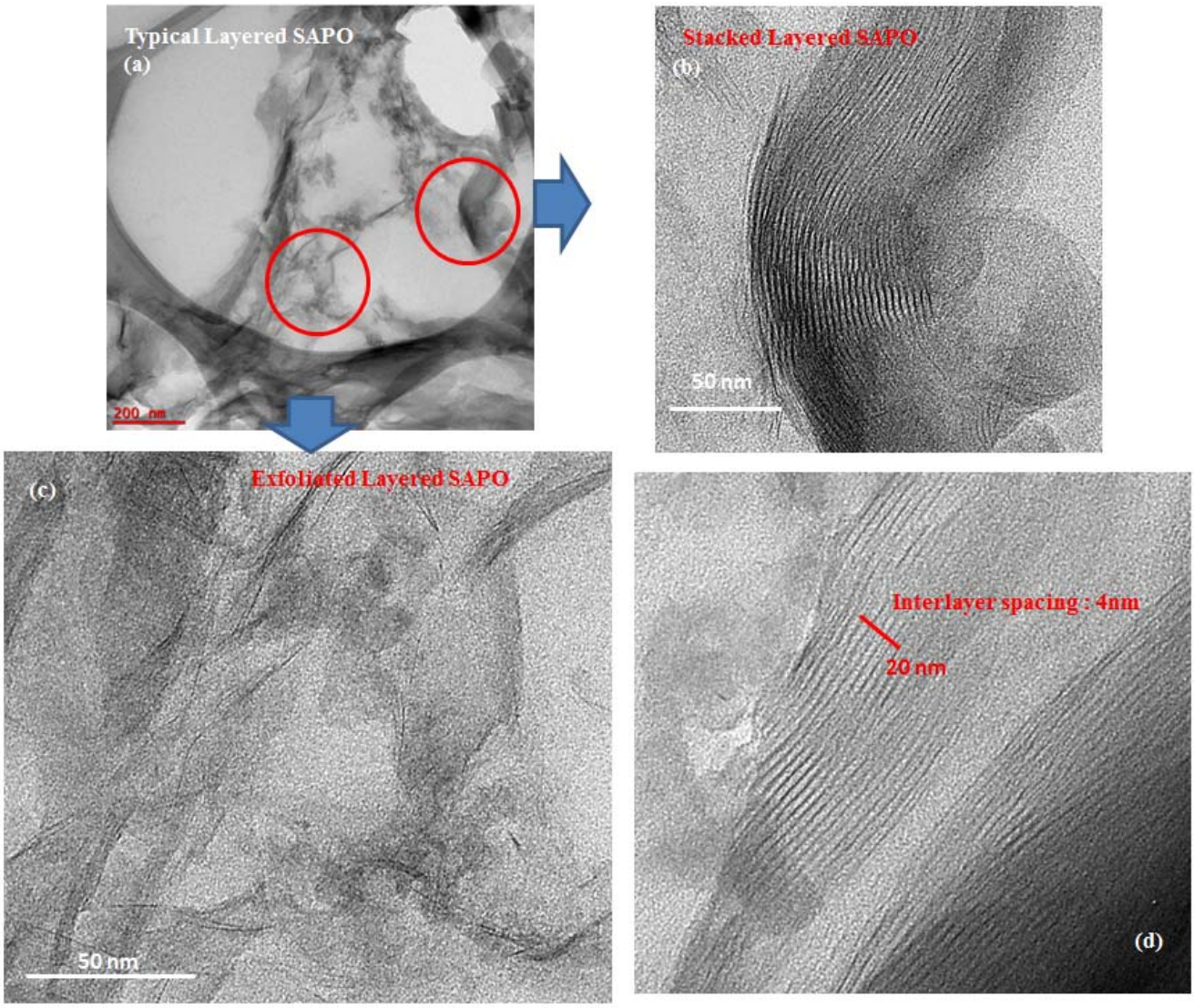

Figure 5-2. HR-TEM images of (a) low-magnification image of layered SAPO, (b) and (d): Stacked layered SAPO, and (c) Exfoliated layered SAPO.

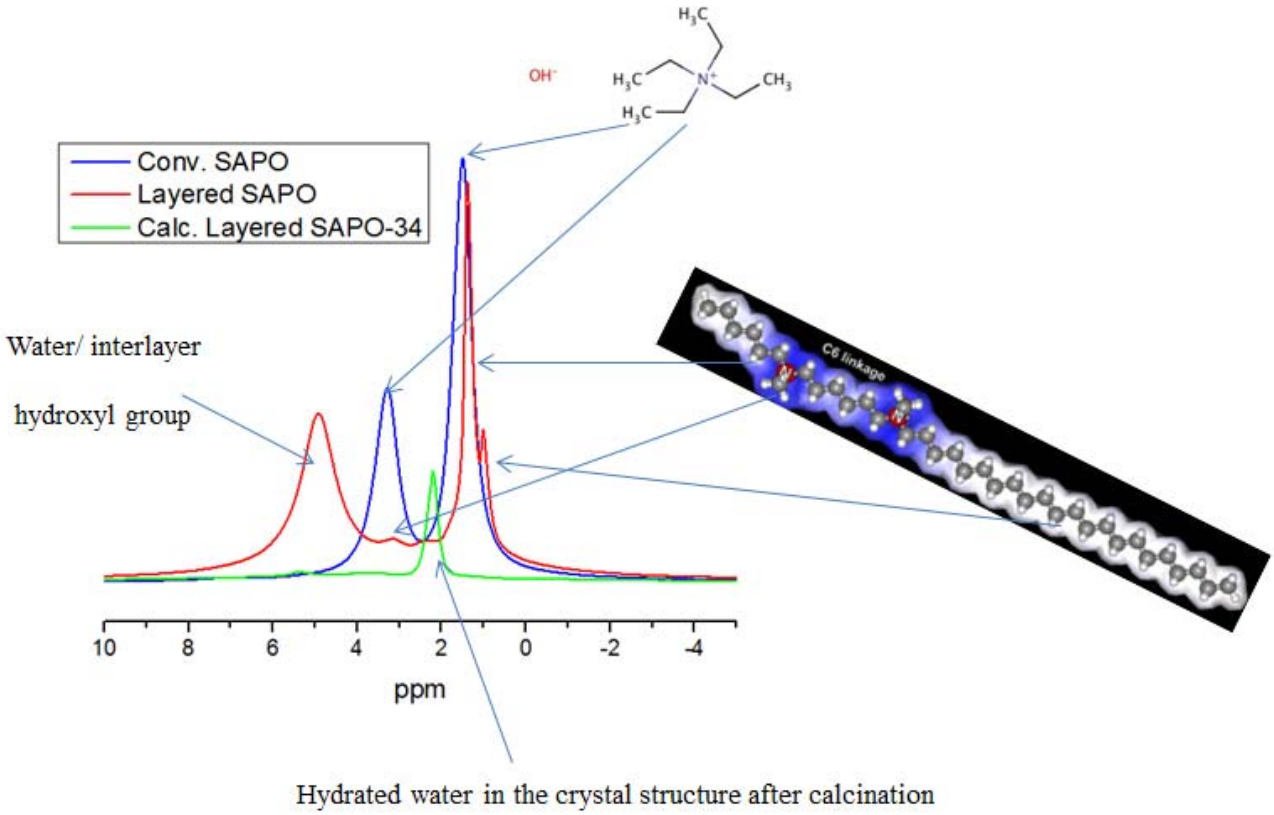

Figure 5-3. H^+-NMR spectra for conventional SAPO-34 and layered SAPO materials.

Figure 5-3 shows the H^+-NMR spectra for SAPO-34 and layered SAPO materials. The templates for the synthesis of SAPO-34 (TEAOH) and layered SAPO ($C_{22\text{-}6\text{-}6}Br_2$) are assigned clearly. The layered SAPO material includes an additional large peak at 5 ppm, representing water/hydroxyl groups. This is a strong indication that hydroxyl groups are present at the surfaces of each layer. After the calcination of layered SAPO at 550°C, only one peak at 2.5 ppm remained, and it may possibly represent octahedrally coordinated residual water adsorbed in the structure.[161]

Figure 5-4 shows the ^{27}Al, ^{29}Si, and ^{31}P-NMR spectra of SAPO-34 and the layered SAPO. Both materials show similar coordination of Al, Si and P species. However, the peak intensity ratios in layered SAPO are quite different from that of SAPO-34, indicating a different crystal structure.

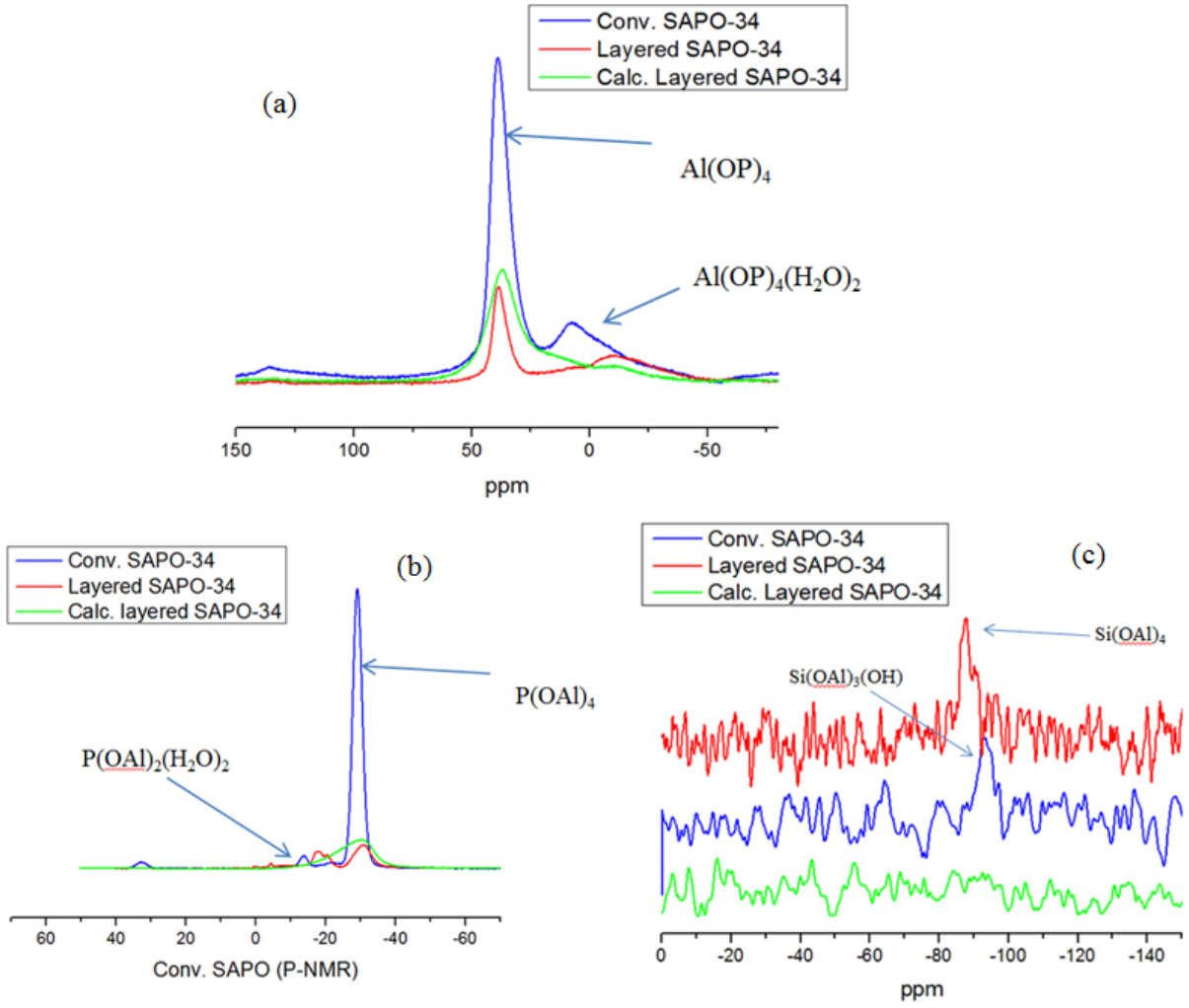

Figure 5-4. (a)^{27}Al, (b)^{31}P (c)^{29}Si -NMR spectra for SAPO-34 and layered SAPO.

5.3.2. Structural analysis of synthesized layered SAPO materials

The crystal structure of the layered SAPO material was revealed *via* detailed structural analysis using XRD and SAED analysis. Figure 5-5 shows the XRD pattern of SAPO-34 and layered SAPO materials. The XRD pattern of layered SAPO showed a sharp and clear peak at 36 Å, indicating the interlayer spacings. The (100) *d*-spacing of 36 Å is consistent with that obtained from TEM analysis shown in Figure 5-2. The XRD pattern of layered SAPO shows very different Bragg diffraction peaks than conventional SAPO-34. It indicates that the layered SAPO material does not have the SAPO-34 (CHA) structure even though it has been synthesized using the same (Si, Al, P) precursor compositions as SAPO-34. The fine-scanned characteristic XRD peaks of the layered SAPO material were compared to various other SAPO materials. This comparison revealed an initial similarity with SAPO-16 that has the AST framework topology.[163] In Figure 5-5, the XRD pattern of SAPO-16 (AST) has been simulated (pink line) and each peak has been indexed. Based upon the simulated peak positions of SAPO-16, each characteristic XRD peak of synthesized layered SAPO material has been tentatively assigned. However, some of the peaks have been shifted and an additional peak appears at 9.8° 2θ.

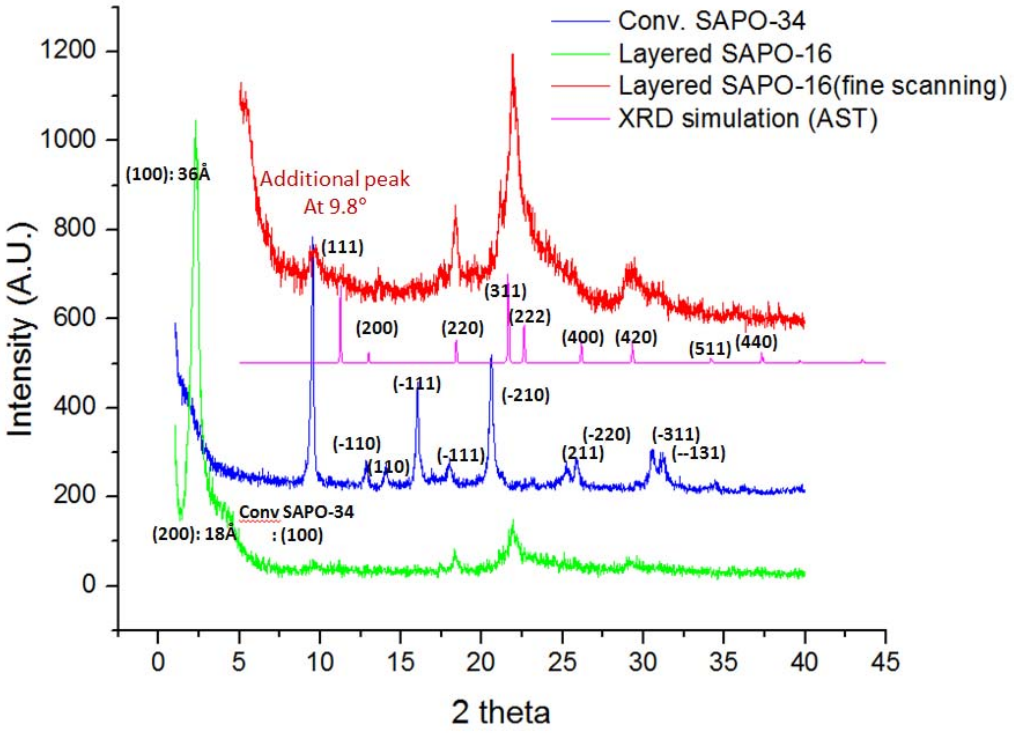

Figure 5-5. XRD patterns of SAPO-34 and layered SAPO materials.

The experimental XRD pattern of layered SAPO has been indexed more rigorously using the Materials Studio (Accelrys) package. Figure 5-6a shows the indexed pattern showing the indexed peak positions (from Table 5-2), and the suggested unit cell of layered SAPO material is represented in Table 5-3. From the result of XRD pattern indexing, the layered SAPO material has been suggested to have an orthorhombic crystal structure as in Figure 5-6b. However, the unit cell of the overall layered material can give no indication of the structure of the individual SAPO layers. As in the case of layered MFI[145], it is difficult to extract detailed structural information on the layers from XRD analysis.

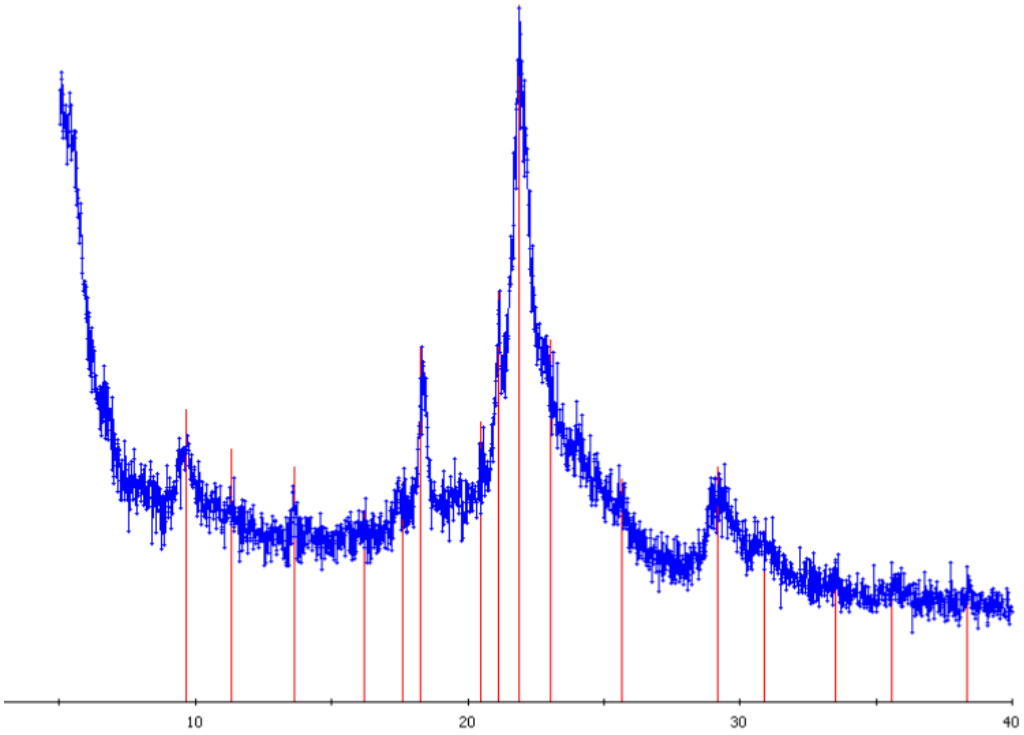

Figure 5-6. Assigned peak position in XRD pattern of layered SAPO materials.

Table 5-2. Indexed peak in XRD pattern of layered SAPO materials.

H	K	L	2TH-OBS	2TH-CALC	D-OBS
1	1	0	9.63	9.63	9.17
1	0	1	11.35	11.34	7.79
3	0	0	13.63	13.61	6.49
4	0	0	18.25	18.18	4.86
3	2	0	21.87	21.87	4.06
1	1	2	23.04	23.02	3.86
0	3	0	25.67	25.68	3.47
4	1	2	calculated line		
3	3	0	29.18	29.17	3.06
2	3	1	calculated line		
3	1	3	35.56	35.56	2.52
8	0	1	38.36	38.37	2.34

Table 5-3. Suggested unit cell of layered SAPO materials from XRD indexing *via* Material Studio.

Unit cell Dimension	Angle
A = 19.5	**α = 90**
B = 10.4	**β= 90**
C = 8.5	**γ= 90**

Selected Area Electron Diffraction (SAED) revealed the detailed crystal structure of the layers. Figure 5-7 shows the SAED pattern from a single (delaminated/exfoliated) layer. The sharp ED spots seen in Figure 5-7b demonstrate that the layered SAPO is a highly crystaline material. The ED pattern has 4-fold-symmetric spots that indicate a cubic structure. This is consistent with our initial hypothesis of a SAPO-16 structure. The measured ED pattern was then indexed with Materials Studio, and the indexed peaks are shown in Figure 5-7b. The layer has a cubic structure with a unit cell size of 13.6 Å, which is the same as that of the AST (SAPO-16) topology. The (100) zone axis of the AST structure is expected to show (200), (202), (400), and (404) peaks as seen in Figure 5-7b.

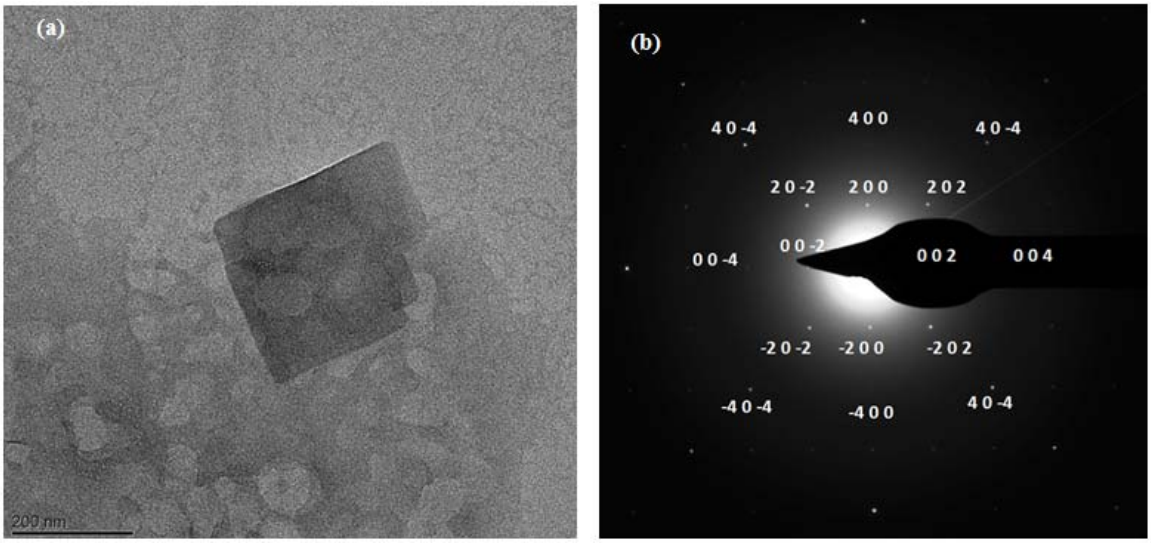

Figure 5-7. SAED (Selected Area Electron Diffraction) analysis of the layered SAPO: (a) TEM image of single layer, and (b) electron diffraction pattern from the layer.

The HR-TEM image and ED pattern of an AST-type layer were also simulated (Figure 5-8) using the software SIMTEM.[164] An 8 × 8 supercell model silicoaluminophosphate (SAPO) layer of AST structure was prepared using Materials Studio. The ED simulation results (Figure 5-8b) show good agreement with the experimental SAED pattern (Figure 5-7b). One difference between the simulation and the experimental ED pattern is that the simulation shows a (402) spot, which was not observed in the measured pattern. The synthesized layered SAPO may have slightly different structure from the 3D SAPO-16 material, and additional analysis such as EXAFS or HR-TEM imaging may be required to confirm the structure of the layered SAPO material.

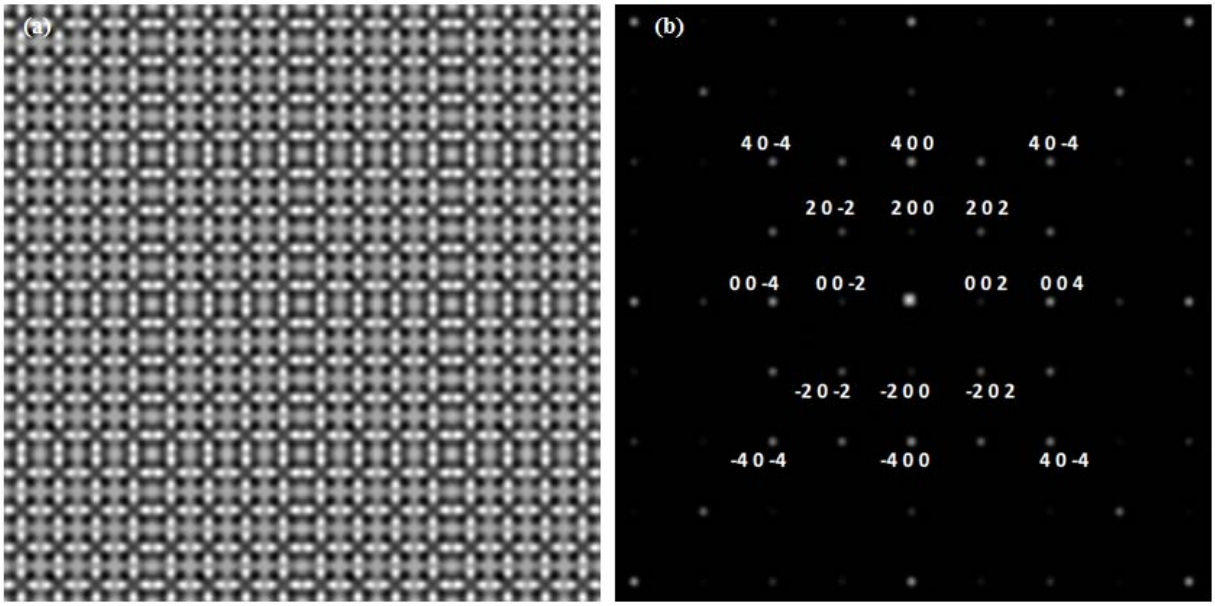

Figure 5-8. Simulated (a) HRTEM image, and (b) SAED pattern from an 8×8 supercell model of a layer with AST topology.

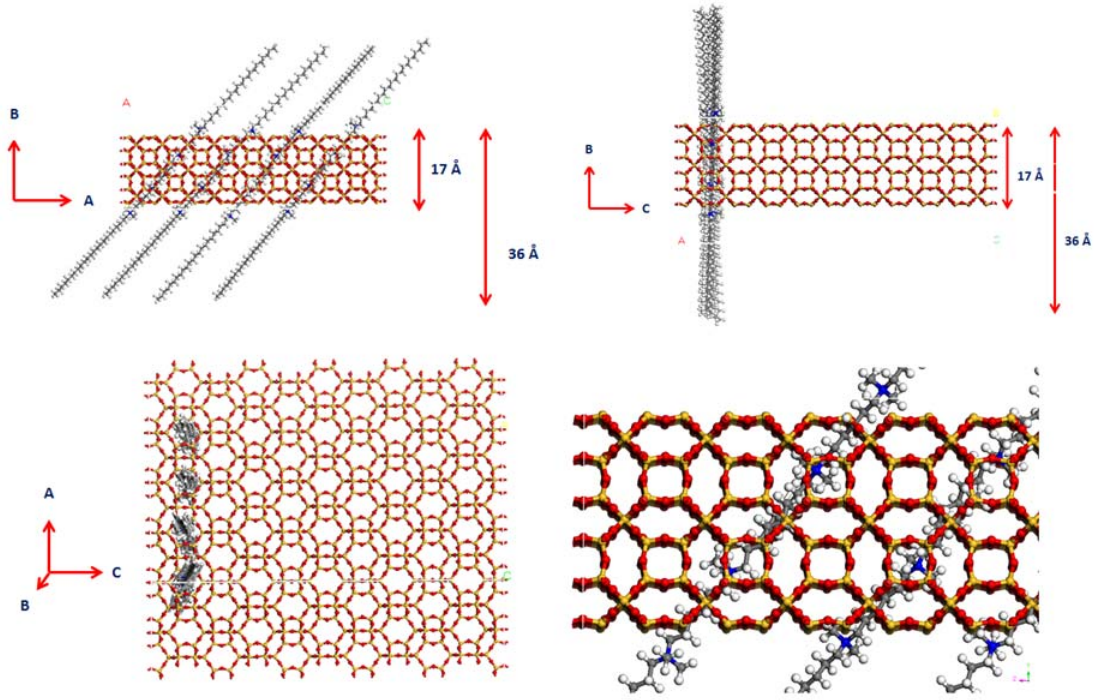

Figure 5-9. Model structure of layered SAPO-16 material.

5.3.3. Model of Layered SAPO-16.

Based on detailed structural analysis of the layered SAPO materials, we find that it has very similar crystal and pore structure to SAPO-16. The tentative structure of the as-made layered SAPO-16 is shown in Figure 5-9. SAPO-16 has the AST framework type and the unit cell is cubic. Because the structure of SAPO-16 layers consists of 6MR pore openings through the diagonal direction, the long-chain diquaternary ammonium cations reside along the diagonal direction. The *d*-spacings obtained from such a model are consistent with our XRD and TEM data. The 6MR pore openings along the diagonal direction could be useful to H_2 separations as in the case of MCM-22.[46]

5.3.4. The analysis on organic loading, porosity and surface area

The TGA data in Figure 5-10 gives quantitative information on the organic template in the layered SAPO-16 material. The weight loss until 100°C is caused by the evaporation of water. The weight loss from 100-500°C allows the estimation of the organic template loading in the layered SAPO-16 material. The measured organic template loading in layered SAPO-16 is 23% and that in conventional SAPO-34 is 15%. Converting these loadings to the number density of template molecules per unit mass of each material, the templates in layered SAPO-16 materials occupy only 38% of the total mass relative to the template in SAPO-34. After eliminating the organic template, the pore fraction in layered SAPO-16 is about 43% of that in conventional SAPO-34. This lower pore density in layered SAPO-16 materials is consistent with the structures of AST and CHA topologies.

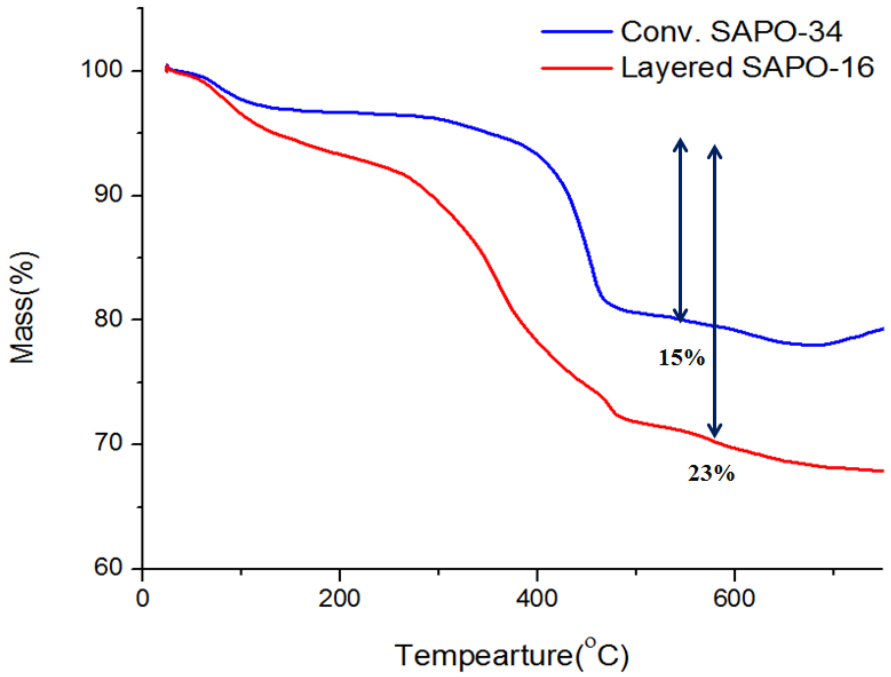

Figure 5-10. TGA data for SAPO-34 and layered SAPO-16 materials.

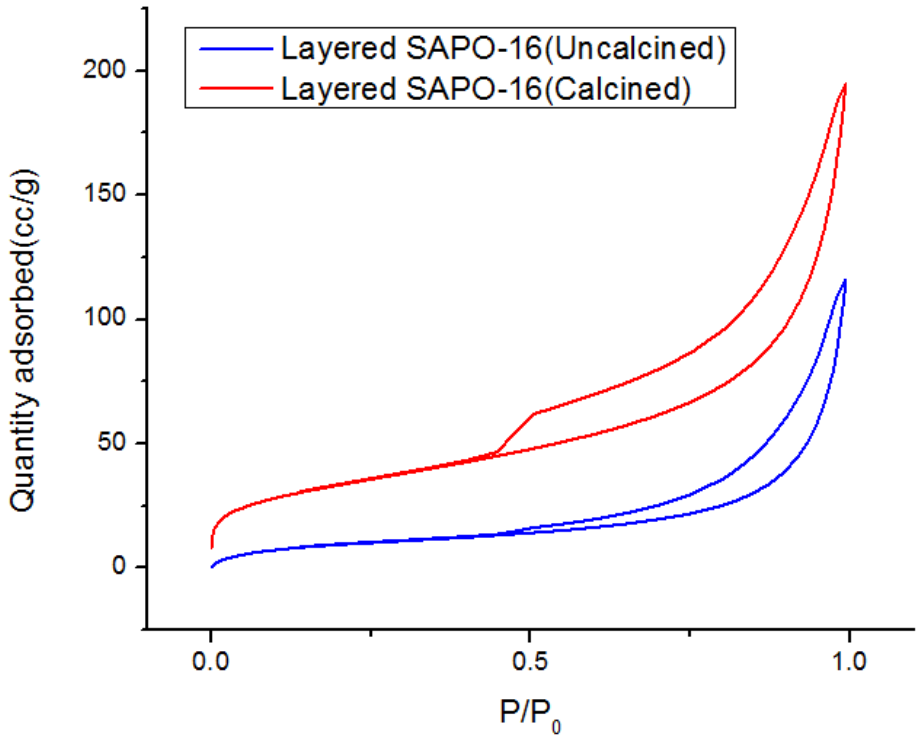

Figure 5-11. N_2 physisorption data of Layered SAPO-16

Figure 5-11 shows the N_2 physisorption isotherms for the layered SAPO-16 materials (as-made and calcined). The corresponding BET and *t*-plot external surface areas are shown in Table 5-2. For the unncalcined sample, the *t*-plot external surface area has been calculated to be larger than the BET total surface area. This result is caused by its highly roughened external surface morphology. The N_2 physisorption isotherm of uncalcined layered SAPO-16 shows hysteresis due to the mesoporosity inherent in the aggregated flakes. After calcination, the mesoporosity increases, likely due to the removal of residual template species in the mesopores. In Table 5-2, the calcined material shows highly increased external surface area, as expected from the SEM images in Figure 5-1. However, the internal surface area (calculated by subtracting external surface area from BET total surface area) is negligible. This is probably because the pore size of layered SAPO-16 structure contains 6MR pores, into which N_2 molecules cannot diffuse.

Table 5-4. Calculated BET surface area and t-plot external surface area of Layered SAPO-16 materials.

	Layered SAPO-16 (Uncalcined)	**Layered SAPO-16 (Calcined)**
BET Surface Area:	34.32 m²/g	**116.74 m²/g**
t-Plot External Surface Area:	45.87 m²/g	**116.67 m^2/g**

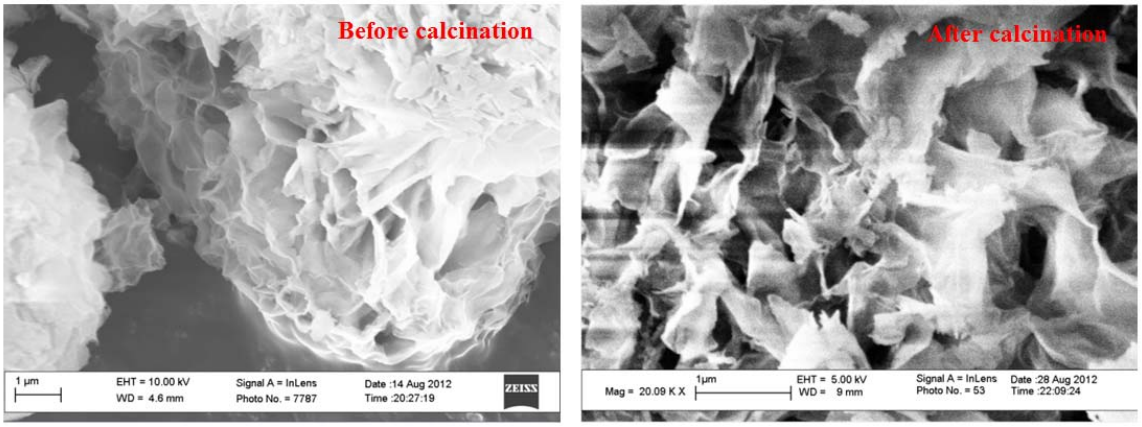

Figure 5-12. SEM image of Layered SAPO-16 (a) before calcination (b) after calcination.

Figure 5-12 shows the surface morphology of layered SAPO-16 before and after calcination. The surface morphology of layered SAPO-16 does not change significantly. However, the elemental analysis shown in Table 3 shows large changes in composition of Al, Si, and P after calcination of layered SAPO-16. The Si content decreases significantly, showing that Si atoms are removed from the structure during calcination. The general mechanism for the formation of SAPO crystal structures is the Si substitution to P or Al atoms.[165] The Si atoms in SAPO materials are possibly the most unstable in the crystal structure of SAPO materials. The XRD data in Figure 5-13 also show that the crystal structure became poorly-defined after calcination. Hence, high temperature calcination may not be the best processing technique for utilizing the layered SAPO-16 materials in catalysis or membrane applications.

Table 5-5. Elemental composition of Layered SAPO-16 materials after calcination. (by SEM-EDX)

Atomic %	O	Al	Si	P
Calcined Layered SAPO-16	60.97	19.86	3.41	15.76
	Only Al, Si, P	**51**	**9**	**40**

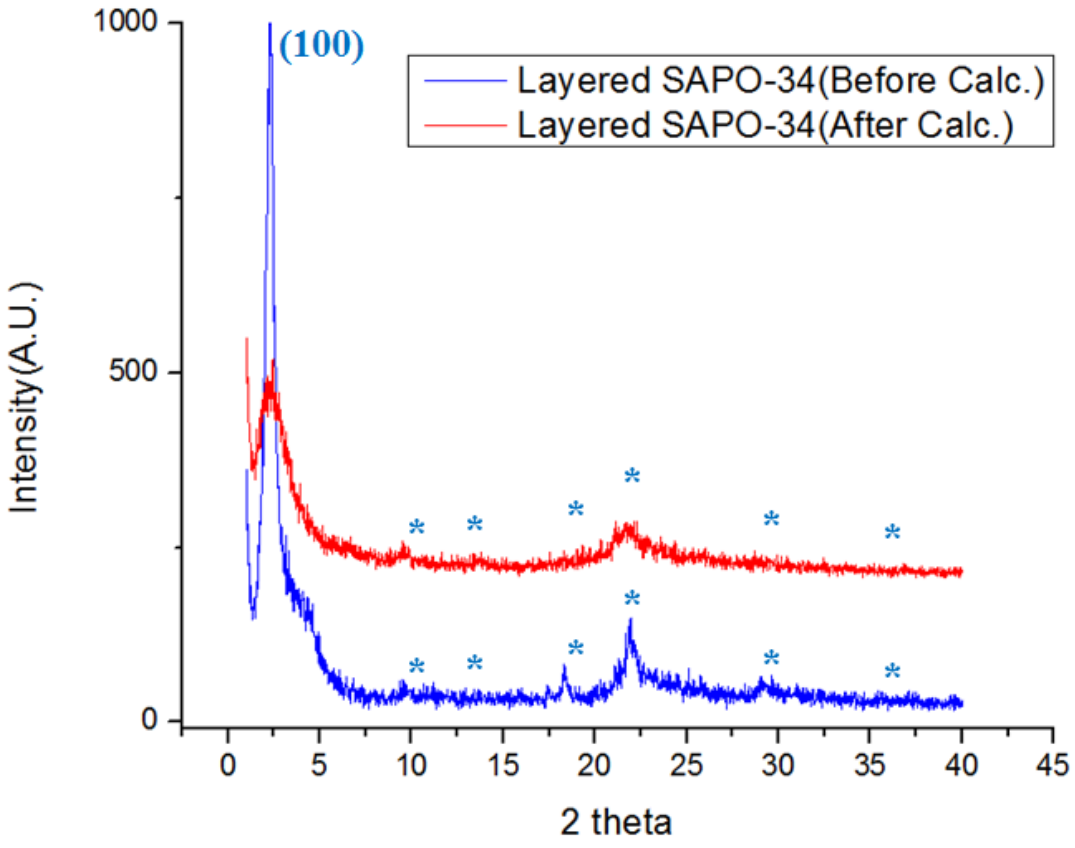

Figure 5-13. XRD pattern of layered SAPO-16 materials before and after calcination

5.3.5. Exfoliation of layered SAPO-16 in DCM solvent

The layered SAPO-16 material has promising exfoliation properties (as seen during HR-TEM analysis in Figure 5-2c), because it has almost no twinned crystal growth during hydrothermal synthesis. A simple exfoliation process was attempted by dispersing this material in dichloromethane (DCM). Typically, 0.1 g of layered SAPO-16 materials was dispersed in 100 ml of DCM solvent, agitated using a magnetic bar for 1 day, then sonicated for 30 min, and dried. Figure 5-14 shows the SEM images of exfoliated layered SAPO flakes. As expected, even the simple dispersion of particles in organic solvent resulted in high degree of exfoliation. Inorganic membranes can be fabricated by coating these exfoliated flakes on porous ceramic, metallic, or polymeric supports. The template molecules can be removed by HCl extraction.

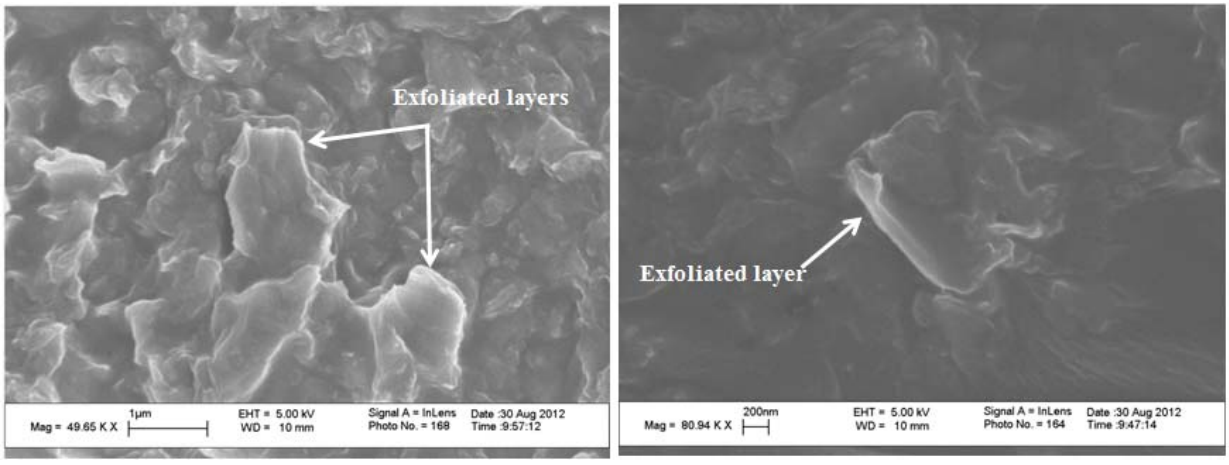

Figure 5-14. SEM image of exfoliated SAPO materials deposited on Carbon tape.

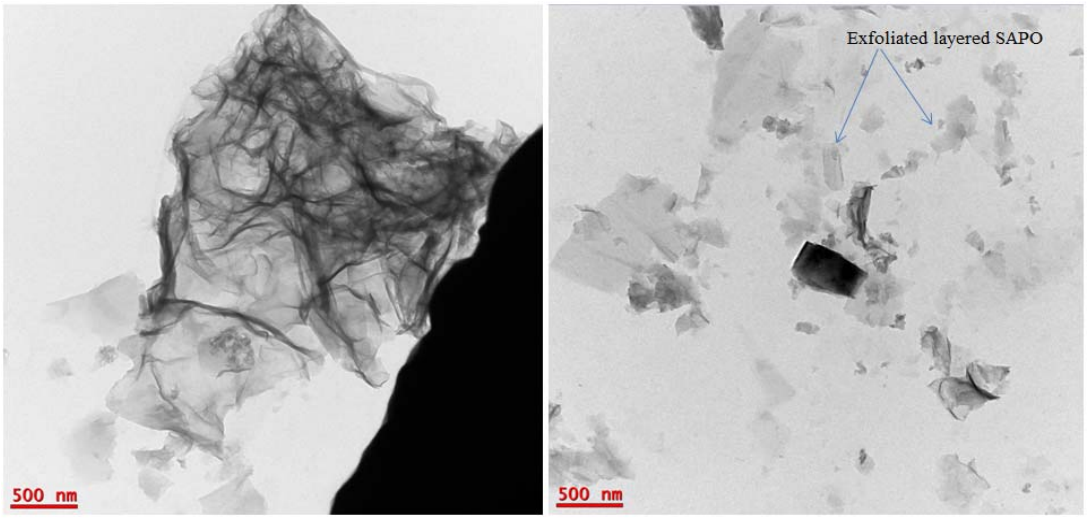

(a) (b)

Figure 5-15. TEM images of exfoliated layered SAPO-16 materials.

While the SEM images show high aspect ratio flakes deposited on a support, single layers of exfoliated layered SAPO-16 are clearly visualized by TEM as shown in Figure 5-15. The layered SAPO-16 flakes in Figure 5-14a are at various stages of exfoliation. The fully exfoliated layered SAPO material is shown in Figure 5-15b, and it has significantly lower contrast than unexfoliated particles.

5.3.6. Exfoliation of layered SAPO-16 materials via template extraction

Dispersing layered SAPO-16 in an organic solvent is an effective way to exfoliate it. However, to fully open up the porosity one must eliminate the SDA molecules. As seen previously, high-temperature calcination may destroy the crystal structure of the layered SAPO-16 (Figure 5-13 and Table 5-3). Therefore, a liquid extraction process was developed to remove the SDA from the structure. A 0.05M HCl/ EtOH solution has been used as the extraction solvent. Typically, 0.1g of layered SAPO-16 powder is dispersed in 100 ml of the solvent and stirred for 1 day, followed by 30 min ultrasonication. The extraction process also resulted in excellent exfoliation of layered SAPO-16. Figure 5-16a shows a thick coating of extracted SAPO-16 material deposited on carbon tape. The platy exfoliated flakes are clearly seen. Figure 5-16b shows that the layered SAPO-16 materials can be deposited in a layer-by-layer fashion, which may be quite useful for fabrication of inorganic membranes. Table 5-6 shows the elemental analysis of extracted layered SAPO-16. The extracted layered SAPO-16 materials shows lower concentration of carbon than as-synthesized layered SAPO-16 (Table 5-1), indicating that some of the long-chain SDA molecules have been extracted. The Al, Si, and P composition of exfoliated layered SAPO-16 remains similar to that of the as-synthesized material.

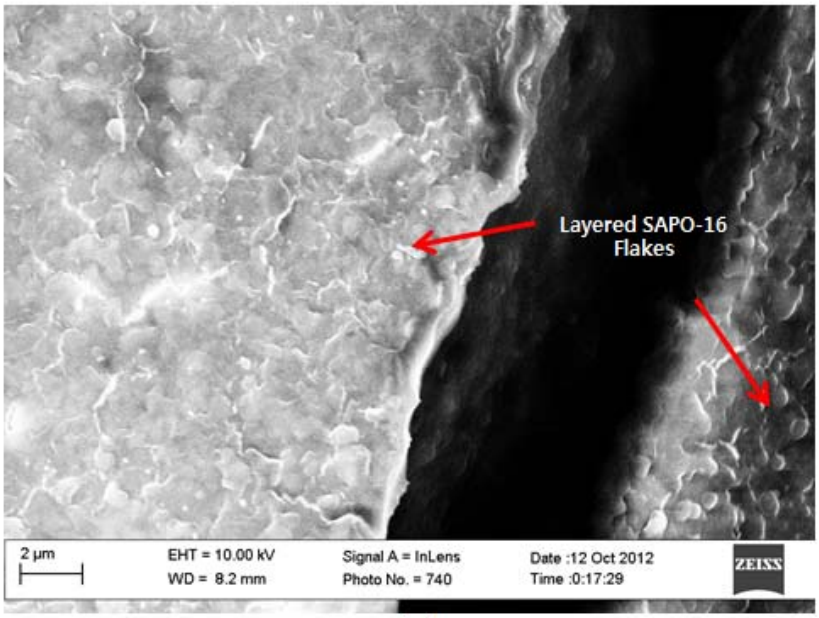

(a)

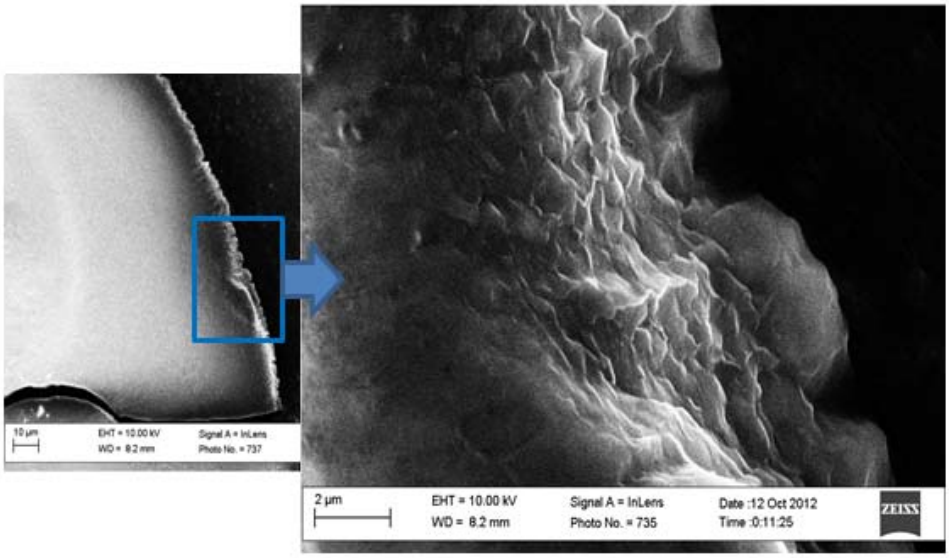

(b)

Figure 5-16. SEM image of extracted Layered SAPO-16 materials.

Table 5-6. Elemental composition of extracted layered SAPO-16 (by SEM-EDX).

Atomic %	C	O	Al	Si	P	Cl
Extracted Layered SAPO-16	44.83	36.65	7.03	1.85	4.98	4.06
		Only Al, Si, P	**51**	**13**	**36**	

Figure 5-17 shows the XRD pattern of layered SAPO-16 after liquid extraction. The (100) peak position representing the interlayer spacing has moved from 36 Å to 42 Å. Due to the lack of alignment of the layers after the extraction process, the XRD peaks at higher angle have been significantly eliminated. However, the magnified XRD pattern shows the remaining traces of these peaks, marked with asterisks. The crystal structure of extracted layered SAPO-16 is expected to be the same as that of the as-made layered SAPO-16 materials.

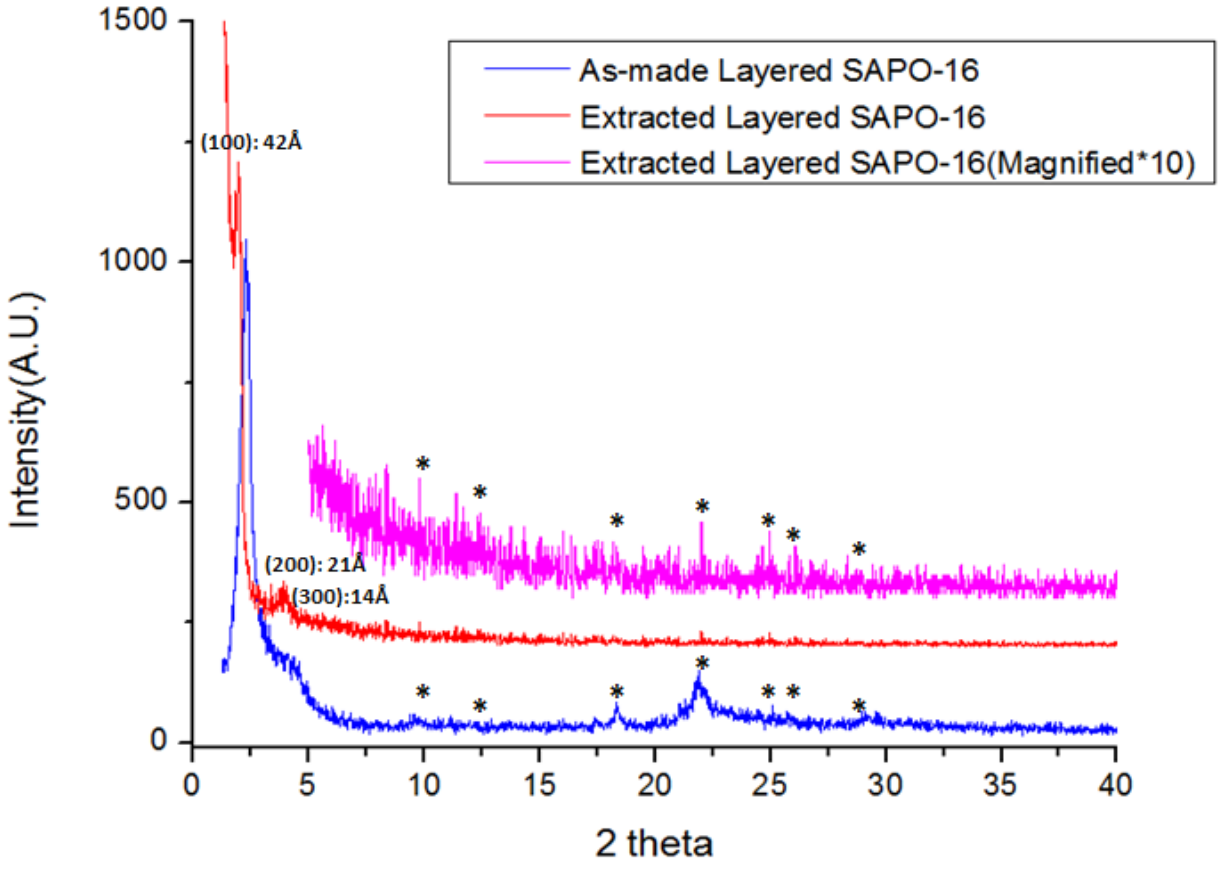

Figure 5-17. XRD patterns of as-made and extracted layered SAPO-16 materials.

5.4. Conclusion

A small-pore layered SAPO material has been synthesized for the first time by the direct hydrothermal synthesis method utilizing long-chain diquaternary ammonium cations. Detailed characterizations of its crystal structure, morphology, and chemical composition have been performed *via* SEM, NMR, XRD, TEM, and SAED analysis with ED simulations. The crystal structure is concluded to be very similar to that of SAPO-16 material with AST crystal topology. The promising properties of this material such as its simple exfoliation chemistry may enable its application to the fabrication of inorganic membranes for separations of gases such as H_2, exploiting its 6MR pore openings. Furthermore, this work sets the stage for possible synthesis of a range of other small-pore layered materials using the long-chain SDA approach.

CHAPTER 6: CONCLUSIONS AND RELATED FUTURE WORKS

6.1. Main Findings

The work described in this thesis has made large progress towards the overall objective of developing ways to fabricate a new class of inorganic or nanocomposite membranes utilizing high-aspect-ratio, nanometer-thin, nanoporous flakes. The present wok has spanned from chemical/mechanical treatments (swelling, functionalization) of existing layered materials, to the discovery of new hybrid and layered zeolitic materials, as well as the fabrication of composite/hybrid membranes that show substantial increases in performance over the corresponding pure polymeric membrane materials.

As a first objective of this thesis, I reported the development and detailed analysis of surface modification techniques for nanoporous layered materials such as AMH-3 and MCM-22. A modified swelling method for AMH-3 was developed using diamine swelling agents. Upon using dodecyldiamine as an effective swelling agent, I obtained a swollen AMH-3 material with a well-defined XRD pattern and a better-preserved crystal pore structure (in relation to the previous use of monoamine swelling agents). Then, a step-wise covalent functionalization method for AMH-3 and MCM-22 was developed. Detailed characterization confirmed the incorporation of covalently-bonded surface functionalizing agents at the surfaces of AMH-3 and MCM-22. The functionalization

process also yielded an AMH-3 material with partially exfoliated layers and improved hydrophobicity.

After the detailed studies on synthesis and chemical treatment of layered materials, SAMH-3/Cellulose Acetate (CA) nanocomposite membranes were successfully fabricated using a high-shear mixer to exfoliate the layers. The microstructure and properties of the resulting membranes were investigated by a variety of experimental techniques. As a result of detailed SAXS and TEM studies, the numbers of SAMH-3 layers in an exfoliated stack are found to be 4-8, which represents a high degree of exfoliation. The SAMH-3/CA composite membranes have been applied to gas separations and their CO_2 and CH_4 gas permeation characteristics have been investigated. Significant improvements in mixed-gas separation performance were attained with only 2-6 wt% of AMH-3 loadings. This effect cannot be predicted by conventional models, and a complex combination of transport phenomena occurring in such membrane systems has been suggested in the present work. Specifically, such transport phenomena include competing effects of transport through the SAMH-3 pores, the mesoporous interlayer spaces, and potentially through a lower-density CA matrix phase. The present results using low particle loadings of AMH-3 could be practically useful in mitigating effects of particle aggregation and polymer-particle interface problems while composite membranes usually using higher volume fractions of inorganic materials.

A type of hybrid zeolitic material, namely an epitaxial growth of layered MFI over a bulk MFI substrate, has been syntheszied and characterized. This microporous-

mesoporous hybrid material may open new possibilities in the applications of zeolite materials to separations and catalysis. Detailed HRTEM analysis elucidated the epitaxial growth of layered MFI on the bulk MFI substrate in principal crystallographic directions. In this "bulk-MFI/layered-MFI" (BMLM) material, the layered MFI creates a large 'external surface area' and 'surface roughness'. The capability of epitaxially growing a layered zeolite on a conventional bulk zeolite creates the possibility of a new class of hybrid zeolitic materials whose properties can be rationally controlled by independently tuning the morphologies of the layered and bulk zeolitic components of the hybrid material. In one example application of this hybrid material, I showed that the highly roughened surface resulted in excellent adhesion to a dense glassy polymer. BMLM containing composite membranes showed better gas permeation properties than bare MFI containing composite membranes, and the fit of the permeation data to the modified Maxwell model yielded physically reasonable values for the interface properties.

I also explored the synthesis of small-pore layered materials by the long-chain surfactant template method, with a view to expand the application of layered porous materials in gas separations. In the last section of my thesis, I synthesized a new small-pore layered SAPO material and conducted detailed characterization studies on it. The synthesized layered SAPO material was found to be the layered counterpart of SAPO-16 material with the AST topology. This type of SAPO layered material with 6MR openings could be valuable in separations of gases such as H_2.

6.2. Related future works and challenges

A new generation of molecular sieving membrane architectures utilizing nanoporous layered materials can lead to significant opportunities in industrial applications. Because these materials can be incorporated in very thin separating layers (~100 nm), they show substantial promise for use in high-performance separations. Much progress has been made, in this thesis and in the literature, towards this goal. However, several challenging issues remain:

Scale up of layered materials and membrane fabrication: It is envisaged that porous layered materials will eventually be coated as membranes on inorganic or polymeric supports. For this purpose, it will be necessary to scale up and process these materials at an industrial scale. Some of the techniques developed in the present work may find use in scaled-up processing of porous layered materials.

Preparation of uniformly exfoliated layered materials: The high purity (uniformity) of exfoliated layered materials is important to prevent the unexpected failure on membrane fabrication and overall separation performances. However, the top-down exfoliation process of layered materials using high shear mixing process may provide a variety of different shapes of exfoliated particles, such as well-exfoliated (or un-exfoliated) and broken flakes. The issue of maintaining the uniformity of exfoliated flakes can be addressed by either optimizing exfoliation conditions or by synthesizing new pre-exfoliated (or easily exfoliated) layered materials. The effective separation of well exfoliated flakes from byproducts (unexfoliated particles) can also improve the

quality of exfoliated layered materials to be used in membranes.

Fabrication of selective flake/polymer composite membranes: There is a growing range of selective flakes with different pore sizes, elemental compositions, and crystallography. Depending on the target gas separations (e.g.CO_2/CH_4, H_2/N_2, etc), the right combination of layered materials and polymer matrices should be selected. The consideration criteria are the permeability "matching" of selective flakes to the permeability in polymer matrix, adhesion at the organic/inorganic surface, operation conditions, etc. A challenge in this area exists in that the performance of membranes with nanoscale flakes cannot be predicted from conventional models. Hence, new computational and theoretical approaches may be needed to provide performance data that can be used to design and optimize the right combination of membrane materials.

REFERENCES

(1) Pandey, P.; Chauhan, R. S.: Membranes for gas separation. *Prog Polym Sci* **2001**, *26*, 853-893.

(2) Jagur-Grodzinski, J.: Polymeric materials for fuel cells: concise review of recent studies. *Polym Advan Technol* **2007**, *18*, 785-799.

(3) Vane, L. M.: A review of pervaporation for product recovery from biomass fermentation processes. *J Chem Technol Biot* **2005**, *80*, 603-629.

(4) Bernardo, P.; Drioli, E.; Golemme, G.: Membrane gas separation: a review/state of the art. *Industrial & Engineering Chemistry Research* **2009**, *48*, 4638-4663.

(5) Stern, S. A.; Mi, Y.; Yamamoto, H.; Stclair, A. K.: Structure Permeability Relationships of Polyimide Membranes - Applications to the Separation of Gas-Mixtures. *J Polym Sci Pol Phys* **1989**, *27*, 1887-1909.

(6) Park, J. Y.; Paul, D. R.: Correlation and prediction of gas permeability in glassy polymer membrane materials via a modified free volume based group contribution method. *J Membrane Sci* **1997**, *125*, 23-39.

(7) Schultz, J.; Peinemann, K. V.: Membranes for separation of higher hydrocarbons from methane. *J Membrane Sci* **1996**, *110*, 37-45.

(8) Pinnau, I.; He, Z. J.: Pure- and mixed-gas permeation properties of polydimethylsiloxane for hydrocarbon/methane and hydrocarbon/hydrogen separation. *J Membrane Sci* **2004**, *244*, 227-233.

(9) Robeson, L. M.: The upper bound revisited. *J Membrane Sci* **2008**, *320*, 390-400.

(10) Davis, M. E.: Ordered porous materials for emerging applications. *Nature* **2002**, *417*, 813-821.

(11) Snyder, M. A.; Tsapatsis, M.: Hierarchical nanomanufacturing: From shaped zeolite nanoparticles to high-performance separation membranes. *Angew Chem Int Edit* **2007**, *46*, 7560-7573.

(12) Caro, J.; Noack, M.: Zeolite membranes - Recent developments and progress. *Micropor Mesopor Mat* **2008**, *115*, 215-233.

(13) Choi, J.; Jeong, H. K.; Snyder, M. A.; Stoeger, J. A.; Masel, R. I.; Tsapatsis, M.: Grain Boundary Defect Elimination in a Zeolite Membrane by Rapid Thermal Processing. *Science* **2009**, *325*, 590-593.

(14) Koros, W. J.: Evotving beyond the thermat age of separation processes: Membranes can lead the way. *Aiche J* **2004**, *50*, 2326-2334.

(15) Mahajan, R.; Koros, W. J.: Mixed matrix membrane materials with glassy polymers. Part 1. *Polym Eng Sci* **2002**, *42*, 1420-1431.

(16) Vu, D. Q.; Koros, W. J.; Miller, S. J.: Mixed matrix membranes using carbon molecular sieves - I. Preparation and experimental results. *J Membrane Sci* **2003**, *211*, 311-334.

(17) Merkel, T. C.; Freeman, B. D.; Spontak, R. J.; He, Z.; Pinnau, I.; Meakin, P.; Hill, A. J.: Ultrapermeable, reverse-selective nanocomposite membranes. *Science* **2002**, *296*, 519-522.

(18) Jia, M. D.; Peinemann, K. V.; Behling, R. D.: Molecular-Sieving Effect of the Zeolite-Filled Silicone-Rubber Membranes in Gas Permeation. *J Membrane Sci* **1991**, *57*, 289-296.

(19) Vankelecom, I. F. J.; DeKinderen, J.; Dewitte, B. M.; Uytterhoeven, J. B.: Incorporation of hydrophobic porous fillers in PDMS membranes for use in pervaporation. *J Phys Chem B* **1997**, *101*, 5182-5185.

(20) Moermans, B.; De Beuckelaer, W.; Vankelecom, I. F. J.; Ravishankar, R.; Martens, J. A.; Jacobs, P. A.: Incorporation of nano-sized zeolites in membranes. *Chem Commun* **2000**, 2467-2468.

(21) Vane, L. M.; Namboodiri, V. V.; Bowen, T. C.: Hydrophobic zeolite-silicone rubber mixed matrix membranes for ethanol-water separation: Effect of zeolite and silicone component selection on pervaporation performance. *J Membrane Sci* **2008**, *308*, 230-241.

(22) Shu, S.; Husain, S.; Koros, W. J.: A general strategy for adhesion enhancement in polymeric composites by formation of nanostructured particle surfaces. *J Phys Chem C* **2007**, *111*, 652-657.

(23) Bae, T. H.; Liu, J. Q.; Lee, J. S.; Koros, W. J.; Jones, C. W.; Nair, S.: Facile High-Yield Solvothermal Deposition of Inorganic Nanostructures on Zeolite Crystals for Mixed Matrix Membrane Fabrication. *J Am Chem Soc* **2009**, *131*, 14662-+.

(24) Adams, R. T.; Lee, S. S.; Bae, T. H.; Ward, J. K.; Johnson, J. R.; Jones, C. W.; Nair, S.; Koros, W. J.: CO2-CH4 permeation in high zeolite 4A loading mixed matrix membranes. *J Membrane Sci* **2011**, *367*, 197-203.

(25) Jeong, H. K.; Krych, W.; Ramanan, H.; Nair, S.; Marand, E.; Tsapatsis, M.: Fabrication of polymer/selective-flake nanocomposite membranes and their use in gas separation. *Chem Mater* **2004**, *16*, 3838-3845.

(26) Zornoza, B.; Gorgojo, P.; Casado, C.; Tellez, C.; Coronas, J.: Mixed matrix membranes for gas separation with special nanoporous fillers. *Desalin Water Treat* **2011**, *27*, 42-47.

(27) Galve, A.; Sieffert, D.; Vispe, E.; Tellez, C.; Coronas, J.; Staudt, C.: Copolyimide mixed matrix membranes with oriented microporous titanosilicate JDF-L1 sheet particles. *J Membrane Sci* **2011**, *370*, 131-140.

(28) Ray, S. S.; Okamoto, M.: Polymer/layered silicate nanocomposites: a review from preparation to processing. *Prog Polym Sci* **2003**, *28*, 1539-1641.

(29) Johnson, J. R.; Koros, W. J.: Utilization of nanoplatelets in organic-inorganic hybrid separation materials: Separation advantages and formation challenges. *J Taiwan Inst Chem E* **2009**, *40*, 268-275.

(30) Dasgupta, S.; Torok, B.: Application of clay catalysts in organic synthesis. A review. *Org Prep Proced Int* **2008**, *40*, 1-65.

(31) Liu, P.: Polymer modified clay minerals: A review. *Appl Clay Sci* **2007**, *38*, 64-76.

(32) Centi, G.; Perathoner, S.: Catalysis by layered materials: A review. *Micropor Mesopor Mat* **2008**, *107*, 3-15.

(33) Paul, D. R.; Robeson, L. M.: Polymer nanotechnology: Nanocomposites. *Polymer* **2008**, *49*, 3187-3204.

(34) Pinnavaia, T. J.: Intercalated Clay Catalysts. *Science* **1983**, *220*, 365-371.

(35) Kloprogge, J. T.: Synthesis of smectites and porous pillared clay catalysts: A review. *J Porous Mat* **1998**, *5*, 5-41.

(36) Usuki, A.; Kojima, Y.; Kawasumi, M.; Okada, A.; Fukushima, Y.; Kurauchi, T.; Kamigaito, O.: Synthesis of Nylon 6-Clay Hybrid. *J Mater Res* **1993**, *8*, 1179-1184.

(37) Messersmith, P. B.; Giannelis, E. P.: Synthesis and Characterization of Layered Silicate-Epoxy Nanocomposites. *Chem Mater* **1994**, *6*, 1719-1725.

(38) Choudalakis, G.; Gotsis, A.: Permeability of polymer/clay nanocomposites: A review. *European Polymer Journal* **2009**, *45*, 967-984.

(39) Rhee, C. H.; Kim, H. K.; Chang, H.; Lee, J. S.: Nafion/sulfonated montmorillonite composite: A new concept electrolyte membrane for direct methanol fuel cells. *Chem Mater* **2005**, *17*, 1691-1697.

(40) Thomassin, J. M.; Pagnoulle, C.; Bizzari, D.; Caldarella, G.; Germain, A.; Jerome, R.: Improvement of the barrier properties of Nafion (R) by fluoro-modified montmorillonite. *Solid State Ionics* **2006**, *177*, 1137-1144.

(41) Lin, Y. F.; Yen, C. Y.; Hung, C. H.; Hsiao, Y. H.; Ma, C. C. M.: A novel composite membranes based on sulfonated montmorillonite modified Nafion((R)) for DMFCs. *J Power Sources* **2007**, *168*, 162-166.

(42) Leonowicz, M. E.; Lawton, J. A.; Lawton, S. L.; Rubin, M. K.: Mcm-22 - a Molecular-Sieve with 2 Independent Multidimensional Channel Systems. *Science* **1994**, *264*, 1910-1913.

(43) Corma, A.; Fornes, V.; Pergher, S. B.; Maesen, T. L. M.; Buglass, J. G.: Delaminated zeolite precursors as selective acidic catalysts. *Nature* **1998**, *396*, 353-356.

(44) Corma, A.; Diaz, U.; Domine, M. E.; Fornes, V.: New aluminosilicate and titanosilicate delaminated materials active for acid catalysis, and oxidation reactions using H2O2. *J Am Chem Soc* **2000**, *122*, 2804-2809.

(45) Corma, A.; Fornes, V.; Diaz, U.: ITQ-18 a new delaminated stable zeolite. *Chem Commun* **2001**, 2642-2643.

(46) Choi, J.; Tsapatsis, M.: MCM-22/Silica Selective Flake Nanocomposite Membranes for Hydrogen Separations. *J Am Chem Soc* **2010**, *132*, 448-+.

(47) Jeong, H. K.; Nair, S.; Vogt, T.; Dickinson, L. C.; Tsapatsis, M.: A highly crystalline layered silicate with three-dimensionally microporous layers. *Nat Mater* **2003**, *2*, 53-58.

(48) Robeson, L. M.: Correlation of Separation Factor Versus Permeability for Polymeric Membranes. *J Membrane Sci* **1991**, *62*, 165-185.

(49) Choi, S.; Coronas, J.; Jordan, E.; Oh, W.; Nair, S.; Onorato, F.; Shantz, D. F.; Tsapatsis, M.: Layered silicates by swelling of AMH-3 and nanocomposite membranes. *Angew Chem Int Edit* **2008**, *47*, 552-555.

(50) Choi, S.; Coronas, J.; Sheffel, J. A.; Jordan, E.; Oh, W.; Nair, S.; Shantz, D. F.; Tsapatsis, M.: Layered silicate by proton exchange and swelling of AMH-3. *Micropor Mesopor Mat* **2008**, *115*, 75-84.

(51) Choi, M.; Na, K.; Kim, J.; Sakamoto, Y.; Terasaki, O.; Ryoo, R.: Stable single-unit-cell nanosheets of zeolite MFI as active and long-lived catalysts (vol 461, pg 246, 2009). *Nature* **2009**, *461*.

(52) Diaz, I.; Kokkoli, E.; Terasaki, O.; Tsapatsis, M.: Surface structure of zeolite (MFI) crystals. *Chem Mater* **2004**, *16*, 5226-5232.

(53) Na, K.; Choi, M.; Park, W.; Sakamoto, Y.; Terasaki, O.; Ryoo, R.: Pillared MFI Zeolite Nanosheets of a Single-Unit-Cell Thickness. *J Am Chem Soc* **2010**, *132*, 4169-4177.

(54) Kim, W.; Zhang, X.; Lee, J. S.; Tsapatsis, M.; Nair, S.: Epitaxially Grown Layered MFI-Bulk MFI Hybrid Zeolitic Materials. *ACS nano* **2012**.

(55) Thomas, J. M.; Raja, R.; Sankar, G.; Bell, R. G.: Molecular sieve catalysts for the regioselective and shape-selective oxyfunctionalization of alkanes in air. *Accounts of Chemical Research* **2001**, *34*, 191-200.

(56) Li, J. Y.; Yu, J. H.; Yan, W. F.; Xu, Y. H.; Xu, W. G.; Qiu, S. L.; Xu, R. R.: Structures and templating effect in the formation of 2D layered aluminophosphates with Al3P4O163- stoichiometry. *Chem Mater* **1999**, *11*, 2600-2606.

(57) Williams, I. D.; Yu, J. H.; Gao, Q. M.; Chen, J. S.; Xu, R. R.: New chain architecture for a one-dimensional aluminophosphate, [H3NCH2CH2NH3][AlP2O8H]. *Chem Commun* **1997**, 1273-1274.

(58) Yu, J.; Sugiyama, K.; Zheng, S.; Qiu, S.; Chen, J.; Xu, R.; Sakamoto, Y.; Terasaki, O.; Hiraga, K.; Light, M.; Hursthouse, M. B.; Thomas, J. M.: Al16P20O80H4.4C(6)H(18)N(2): A new microporous aluminophosphate containing intersecting 12- and 8-membered ring channels. *Chem Mater* **1998**, *10*, 1208-1211.

(59) Yan, W. F.; Yu, J. H.; Shi, Z.; Xu, R. R.: A novel open-framework aluminophosphate [AlP2O6(OH)(2)][H3O] containing propeller-like chiral motifs. *Chem Commun* **2000**, 1431-1432.

(60) Yu, J.; Terasaki, O.; Williams, I. D.; Quiv, S.; Xu, R.: Solvothermal synthesis and characterization of new aluminophosphate layers templated by imidazolium ions. *Supramolecular Science* **1998**, *5*, 297-302.

(61) Williams, I. D.; Gao, Q. M.; Chen, J. S.; Ngai, L. Y.; Lin, Z. Y.; Xu, R. R.: Organo-template control of inorganic structures: A low-symmetry two-dimensional sheet aluminophosphate3[NH(3)CHMeCH(2)NH(3)][Al6P8O32]center dot H2O. *Chem Commun* **1996**, 1781-1782.

(62) Novoselov, K. S.; Geim, A. K.; Morozov, S. V.; Jiang, D.; Zhang, Y.; Dubonos, S. V.; Grigorieva, I. V.; Firsov, A. A.: Electric field effect in atomically thin carbon films. *Science* **2004**, *306*, 666-669.

(63) Bunch, J. S.; van der Zande, A. M.; Verbridge, S. S.; Frank, I. W.; Tanenbaum, D. M.; Parpia, J. M.; Craighead, H. G.; McEuen, P. L.: Electromechanical resonators from graphene sheets. *Science* **2007**, *315*, 490-493.

(64) Staley, N.; Wang, H.; Puls, C.; Forster, J.; Jackson, T. N.; McCarthy, K.; Clouser, B.; Liu, Y.: Lithography-free fabrication of graphene devices. *Appl Phys Lett* **2007**, *90*.

(65) Liu, H. T.; Ryu, S. M.; Chen, Z. Y.; Steigerwald, M. L.; Nuckolls, C.; Brus, L. E.: Photochemical Reactivity of Graphene. *J Am Chem Soc* **2009**, *131*, 17099-+.

(66) Urban, K. W.: ELECTRON MICROSCOPY The challenges of graphene. *Nat Mater* **2011**, *10*, 165-166.

(67) Tung, V. C.; Allen, M. J.; Yang, Y.; Kaner, R. B.: High-throughput solution processing of large-scale graphene. *Nat Nanotechnol* **2009**, *4*, 25-29.

(68) Bagri, A.; Mattevi, C.; Acik, M.; Chabal, Y. J.; Chhowalla, M.; Shenoy, V. B.: Structural evolution during the reduction of chemically derived graphene oxide. *Nat Chem* **2010**, *2*, 581-587.

(69) Allen, M. J.; Tung, V. C.; Kaner, R. B.: Honeycomb Carbon: A Review of Graphene. *Chem Rev* **2010**, *110*, 132-145.

(70) Shao, Y. Y.; Wang, J.; Wu, H.; Liu, J.; Aksay, I. A.; Lin, Y. H.: Graphene Based Electrochemical Sensors and Biosensors: A Review. *Electroanal* **2010**, *22*, 1027-1036.

(71) Blankenburg, S.; Bieri, M.; Fasel, R.; Mullen, K.; Pignedoli, C. A.; Passerone, D.: Porous Graphene as an Atmospheric Nanofilter. *Small* **2010**, *6*, 2266-2271.

(72) Fischbein, M. D.; Drndic, M.: Electron beam nanosculpting of suspended graphene sheets. *Appl Phys Lett* **2008**, *93*.

(73) Bieri, M.; Treier, M.; Cai, J. M.; Ait-Mansour, K.; Ruffieux, P.; Groning, O.; Groning, P.; Kastler, M.; Rieger, R.; Feng, X. L.; Mullen, K.; Fasel, R.: Porous graphenes: two-dimensional polymer synthesis with atomic precision. *Chem Commun* **2009**, 6919-6921.

(74) Schrier, J.: Helium Separation Using Porous Graphene Membranes. *J Phys Chem Lett* **2010**, *1*, 2284-2287.

(75) Jiang, D. E.; Cooper, V. R.; Dai, S.: Porous Graphene as the Ultimate Membrane for Gas Separation. *Nano Lett* **2009**, *9*, 4019-4024.

(76) Schaefer, D. W.; Justice, R. S.: How nano are nanocomposites? *Macromolecules* **2007**, *40*, 8501-8517.

(77) Vaia, R. A.; Maguire, J. F.: Polymer nanocomposites with prescribed morphology: Going beyond nanoparticle-filled polymers. *Chem Mater* **2007**, *19*, 2736-2751.

(78) Pavlidou, S.; Papaspyrides, C. D.: A review on polymer-layered silicate nanocomposites. *Prog Polym Sci* **2008**, *33*, 1119-1198.

(79) Varoon, K.; Zhang, X. Y.; Elyassi, B.; Brewer, D. D.; Gettel, M.; Kumar, S.; Lee, J. A.; Maheshwari, S.; Mittal, A.; Sung, C. Y.; Cococcioni, M.; Francis, L. F.; McCormick, A. V.; Mkhoyan, K. A.; Tsapatsis, M.: Dispersible Exfoliated Zeolite Nanosheets and Their Application as a Selective Membrane. *Science* **2011**, *333*, 72-75.

(80) Ray, S. S.; Bousmina, M.: Biodegradable polymers and their layered silicate nano composites: In greening the 21st century materials world. *Prog Mater Sci* **2005**, *50*, 962-1079.

(81) Krikorian, V.; Pochan, D. J.: Poly (L-lactic acid)/layered silicate nanocomposite: Fabrication, characterization, and properties. *Chem Mater* **2003**, *15*, 4317-4324.

(82) Lee, S. S.; Ma, Y. T.; Rhee, H. W.; Kim, J.: Exfoliation of layered silicate facilitated by ring-opening reaction of cyclic oligomers in PET-clay nanocomposites. *Polymer* **2005**, *46*, 2201-2210.

(83) Nair, R. R.; Wu, H. A.; Jayaram, P. N.; Grigorieva, I. V.; Geim, A. K.: Unimpeded Permeation of Water Through Helium-Leak-Tight Graphene-Based Membranes. *Science* **2012**, *335*, 442-444.

(84) Koenig, S. P.; Wang, L. D.; Pellegrino, J.; Bunch, J. S.: Selective molecular sieving through porous graphene. *Nat Nanotechnol* **2012**, *7*, 728-732.

(85) Kang, D. Y.; Tong, H. M.; Zang, J.; Choudhury, R. P.; Sholl, D. S.; Beckham, H. W.; Jones, C. W.; Nair, S.: Single-Walled Aluminosilicate

Nanotube/Poly(vinyl alcohol) Nanocomposite Membranes. *Acs Appl Mater Inter* **2012**, *4*, 965-976.

(86) Gebel, G.; Diat, O.: Neutron and x-ray scattering: Suitable tools for studying ionomer membranes. *Fuel Cells* **2005**, *5*, 261-276.

(87) Schmidt-Rohr, K.; Chen, Q.: Parallel cylindrical water nanochannels in Nafion fuel-cell membranes. *Nat Mater* **2008**, *7*, 75-83.

(88) Kulkarni, S.; Krause, S.; Wignall, G. D.: Investigation of the Pore Structure and Morphology of Cellulose-Acetate Membranes Using Small-Angle Neutron-Scattering .2. Ultrafiltration and Reverse-Osmosis Membranes. *Macromolecules* **1994**, *27*, 6785-6790.

(89) Kratky, O.; Porod, G.: Diffuse small-angle scattering of X-rays in colloid systems. *Journal of colloid science* **1949**, *4*, 35.

(90) Wang, B. N.; Bennett, R. D.; Verploegen, E.; Hart, A. J.; Cohen, R. E.: Characterizing the morphologies of mechanically manipulated multiwall carbon nanotube films by small-angle X-ray scattering. *J Phys Chem C* **2007**, *111*, 17933-17940.

(91) Ho, D. L.; Briber, R. M.; Glinka, C. J.: Characterization of organically modified clays using scattering and microscopy techniques. *Chem Mater* **2001**, *13*, 1923-1931.

(92) Hanley, H. J. M.; Muzny, C. D.; Ho, D. L.; Glinka, C. J.: A small-angle neutron scattering study of a commercial organoclay dispersion. *Langmuir* **2003**, *19*, 5575-5580.

(93) Yoonessi, M.; Toghiani, H.; Daulton, T. L.; Lin, J. S.; Pittman, C. U.: Clay delamination in clay/poly(dicyclopentadiene) nanocomposites quantified by small angle neutron scattering and high-resolution transmission electron microscopy. *Macromolecules* **2005**, *38*, 818-831.

(94) Xu, B.; Leisen, J.; Beckham, H. W.; Abu-Zurayk, R.; Harkin-Jones, E.; McNally, T.: Evolution of Clay Morphology in Polypropylene/Montmorillonite Nanocomposites upon Equibiaxial Stretching: A Solid-State NMR and TEM Approach. *Macromolecules* **2009**, *42*, 8959-8968.

(95) Cussler, E. L.: Membranes Containing Selective Flakes. *J Membrane Sci* **1990**, *52*, 275-288.

(96) Sheffel, J. A.; Tsapatsis, M.: A model for the performance of microporous mixed matrix membranes with oriented selective flakes. *J Membrane Sci* **2007**, *295*, 50-70.

(97) Sheffel, J. A.; Tsapatsis, M.: A semi-empirical approach for predicting the performance of mixed matrix membranes containing selective flakes. *J Membrane Sci* **2009**, *326*, 595-607.

(98) Choi, S. H.; Coronas, J.; Lai, Z. P.; Yust, D.; Onorato, F.; Tsapatsis, M.: Fabrication and gas separation properties of polybenzimidazole (PBI)/nanoporous silicates hybrid membranes. *J Membrane Sci* **2008**, *316*, 145-152.

(99) Karan, S.; Samitsu, S.; Peng, X. S.; Kurashima, K.; Ichinose, I.: Ultrafast Viscous Permeation of Organic Solvents Through Diamond-Like Carbon Nanosheets. *Science* **2012**, *335*, 444-447.

(100) Ismail, A. F.; Rana, D.; Matsuura, T.; Foley, H. C.: *Carbon-based membranes for separation processes*; Springer, 2011.

(101) Paul, D. R.: Creating New Types of Carbon-Based Membranes. *Science* **2012**, *335*, 413-414.

(102) Jung, D. H.; Cho, S. Y.; Peck, D. H.; Shin, D. R.; Kim, J. S.: Preparation and performance of a Nafion (R)/montmorillonite nanocomposite membrane for direct methanol fuel cell. *J Power Sources* **2003**, *118*, 205-211.

(103) Hudiono, Y.; Choi, S.; Shu, S.; Koros, W. J.; Tsapatsis, M.; Nair, S.: Porous layered oxide/Nafion (R) nanocomposite membranes for direct methanol fuel cell applications. *Micropor Mesopor Mat* **2009**, *118*, 427-434.

(104) Kim, J.; Jeon, J. D.; Kwak, S. Y.: Delamination of microporous layered silicate by acid-hydrothermal treatment and its use for reduction of methanol crossover in DMFC. *Micropor Mesopor Mat* **2012**.

(105) Mahajan, R.; Koros, W. J.: Mixed matrix membrane materials with glassy polymers. Part 2. *Polym Eng Sci* **2002**, *42*, 1432-1441.

(106) Vu, D. Q.; Koros, W. J.; Miller, S. J.: Mixed matrix membranes using carbon molecular sieves - II. Modeling permeation behavior. *J Membrane Sci* **2003**, *211*, 335-348.

(107) Hudiono, Y.; Choi, S.; Shu, S.; Koros, W.; Tsapatsis, M.; Nair, S.: Porous layered oxide/Nafion® nanocomposite membranes for direct methanol fuel cell applications. *Micropor Mesopor Mat* **2009**, *118*, 427-434.

(108) Maheshwari, S.; Jordan, E.; Kumar, S.; Bates, F. S.; Penn, R. L.; Shantz, D. F.; Tsapatsis, M.: Layer structure preservation during swelling, pillaring, and exfoliation of a zeolite precursor. *J Am Chem Soc* **2008**, *130*, 1507-1516.

(109) Shimojima, A.; Umeda, N.; Kuroda, K.: Synthesis of layered inorganic-organic nanocomposite films from mono-, di-, and trimethoxy(alkyl)silane-tetramethoxysilane systems. *Chem Mater* **2001**, *13*, 3610-3616.

(110) Carrado, K. A.; Xu, L. Q.; Csencsits, R.; Muntean, J. V.: Use of organo- and alkoxysilanes in the synthesis of grafted and pristine clays. *Chem Mater* **2001**, *13*, 3766-3773.

(111) Wang, Z.; Pinnavaia, T. J.: Hybrid organic-inorganic nanocomposites: Exfoliation of magadiite nanolayers in an elastomeric epoxy polymer. *Chem Mater* **1998**, *10*, 1820-1826.

(112) Ruizhitzky, E.; Rojo, J. M.: Intracrystalline Grafting on Layer Silicic Acids. *Nature* **1980**, *287*, 28-30.

(113) Tunney, J. J.; Detellier, C.: Interlamellar Covalent Grafting of Organic Units on Kaolinite. *Chem Mater* **1993**, *5*, 747-748.

(114) Mercier, L.; Detellier, C.: Preparation, Characterization and Applications as Heavy-Metals Sorbents of Covalently Grafted Thiol Functionalities on the Interlamellar Surface of Montmorillonite. *Environ Sci Technol* **1995**, *29*, 1318-1323.

(115) Rhee, C. H.; Kim, H. K.; Chang, H.; Lee, J. S.: Nafion/Sulfonated Montmorillonite Composite: A New Concept Electrolyte Membrane for Direct Methanol Fuel Cells. *Chem Mater* **2005**, *17*, 1691-1697.

(116) Fyfe, C. A.; Niu, J.: Direct Solid-State C-13 Nmr Evidence for Covalent Bond Formation between an Immobilized Vinylsilane Linking Agent and Polymer Matrices. *Macromolecules* **1995**, *28*, 3894-3897.

(117) Lai, Z. P.; Bonilla, G.; Diaz, I.; Nery, J. G.; Sujaoti, K.; Amat, M. A.; Kokkoli, E.; Terasaki, O.; Thompson, R. W.; Tsapatsis, M.; Vlachos, D. G.:

Microstructural optimization of a zeolite membrane for organic vapor separation. *Science* **2003**, *300*, 456-460.

(118) Noble, R. D.: Perspectives on mixed matrix membranes. *J Membrane Sci* **2011**, *378*, 393-397.

(119) Bae, T. H.; Lee, J. S.; Qiu, W. L.; Koros, W. J.; Jones, C. W.; Nair, S.: A High-Performance Gas-Separation Membrane Containing Submicrometer-Sized Metal-Organic Framework Crystals. *Angew Chem Int Edit* **2010**, *49*, 9863-9866.

(120) Zornoza, B.; Martinez-Joaristi, A.; Serra-Crespo, P.; Tellez, C.; Coronas, J.; Gascon, J.; Kapteijn, F.: Functionalized flexible MOFs as fillers in mixed matrix membranes for highly selective separation of CO(2) from CH(4) at elevated pressures. *Chem Commun* **2011**, *47*, 9522-9524.

(121) Kang, D. Y.; Jones, C. W.; Nair, S.: Modeling molecular transport in composite membranes with tubular fillers. *J Membrane Sci* **2011**, *381*, 50-63.

(122) Liu, J. Q.; Bae, T. H.; Qiu, W. L.; Husain, S.; Nair, S.; Jones, C. W.; Chance, R. R.; Koros, W. J.: Butane isomer transport properties of 6FDA-DAM and MFI-6FDA-DAM mixed matrix membranes. *J Membrane Sci* **2009**, *343*, 157-163.

(123) Lydon, M. E.; Unocic, K. A.; Bae, T.-H.; Jones, C. W.; Nair, S.: Structure-Property Relationships of Inorganically Surface-Modified Zeolite Molecular Sieves for Nanocomposite Membrane Fabrication. *The Journal of Physical Chemistry C* **2012**, *116*, 9636-9645

(124) Roth, W. J.; Cejka, J.: Two-dimensional zeolites: dream or reality? *Catal Sci Technol* **2011**, *1*, 43-53.

(125) Rubio, C.; Casado, C.; Gorgojo, P.; Etayo, F.; Uriel, S.; Tellez, C.; Coronas, J.: Exfoliated Titanosilicate Material UZAR-S1 Obtained from JDF-L1. *Eur J Inorg Chem* **2010**, 159-163.

(126) Gorgojo, P.; Sieffert, D.; Staudt, C.; Tellez, C.; Coronas, J.: Exfoliated zeolite Nu-6(2) as filler for 6FDA-based copolyimide mixed matrix membranes. *J Membrane Sci* **2012**, *411*, 146-152.

(127) Xiong, D. B.; Zhao, J. T.; Chen, H. H.; Yang, X. X.: A borogermanate with three-dimensional open-framework layers. *Chem-Eur J* **2007**, *13*, 9862-9865.

(128) Takahashi, N.; Kuroda, K.: Materials design of layered silicates through covalent modification of interlayer surfaces. *J Mater Chem* **2011**, *21*, 14336-14353.

(129) Kim, W. G.; Choi, S. H.; Nair, S.: Swelling, Functionalization, and Structural Changes of the Nanoporous Layered Silicates AMH-3 and MCM-22. *Langmuir* **2011**, *27*, 7892-7901.

(130) Pan, C. Y.: Gas Separation by High-Flux, Asymmetric Hollow-Fiber Membrane. *Aiche J* **1986**, *32*, 2020-2027.

(131) Baker, R. W.; Lokhandwala, K.: Natural gas processing with membranes: An overview. *Industrial & Engineering Chemistry Research* **2008**, *47*, 2109-2121.

(132) Lee, J. S.; Madden, W.; Koros, W. J.: Antiplasticization and plasticization of Matrimid (R) asymmetric hollow fiber membranes-Part A. Experimental. *J Membrane Sci* **2010**, *350*, 232-241.

(133) Wang, H. S.; Zhao, T.; Zhi, L. J.; Yan, Y. H.; Yu, Y. Z.: Synthesis of novolac/layered silicate nanocomposites by reaction exfoliation using acid-modified montmorillonite. *Macromol Rapid Comm* **2002**, *23*, 44-48.

(134) Yoshioka, M.; Takabe, K.; Sugiyama, J.; Nishio, Y.: Newly developed nanocomposites from cellulose acetate/layered silicate/poly(epsilon-caprolactone): synthesis and morphological characterization. *J Wood Sci* **2006**, *52*, 121-127.

(135) Idris, A.; Ismail, A. F.; Gordeyev, S. A.; Shilton, S. J.: Rheology assessment of cellulose acetate spinning solution and its influence on reverse osmosis hollow fiber membrane performance. *Polym Test* **2003**, *22*, 319-325.

(136) Kline, S. R.: Reduction and analysis of SANS and USANS data using IGOR Pro. *J Appl Crystallogr* **2006**, *39*, 895-900.

(137) Konduri, S.; Nair, S.: A computational study of gas molecule transport in a polymer/nanoporous layered silicate nanocomposite membrane material. *J Phys Chem C* **2007**, *111*, 2017-2024.

(138) Cundy, C. S.; Cox, P. A.: The hydrothermal synthesis of zeolites: History and development from the earliest days to the present time. *Chem Rev* **2003**, *103*, 663-701.

(139) Davis, M. E.: Zeolite catalysis: Past, present, and future. *Abstr Pap Am Chem S* **2000**, *219*, U528-U528.

(140) Tosheva, L.; Valtchev, V. P.: Nanozeolites: Synthesis, crystallization mechanism, and applications. *Chem Mater* **2005**, *17*, 2494-2513.

(141) Kresge, C. T.; Leonowicz, M. E.; Roth, W. J.; Vartuli, J. C.; Beck, J. S.: Ordered Mesoporous Molecular-Sieves Synthesized by a Liquid-Crystal Template Mechanism. *Nature* **1992**, *359*, 710-712.

(142) Zhao, D. Y.; Feng, J. L.; Huo, Q. S.; Melosh, N.; Fredrickson, G. H.; Chmelka, B. F.; Stucky, G. D.: Triblock copolymer syntheses of mesoporous silica with periodic 50 to 300 angstrom pores. *Science* **1998**, *279*, 548-552.

(143) Fan, W.; Snyder, M. A.; Kumar, S.; Lee, P. S.; Yoo, W. C.; McCormick, A. V.; Penn, R. L.; Stein, A.; Tsapatsis, M.: Hierarchical nanofabrication of microporous crystals with ordered mesoporosity. *Nat Mater* **2008**, *7*, 984-991.

(144) Choi, M.; Cho, H. S.; Srivastava, R.; Venkatesan, C.; Choi, D. H.; Ryoo, R.: Amphiphilic organosilane-directed synthesis of crystalline zeolite with tunable mesoporosity. *Nat Mater* **2006**, *5*, 718-723.

(145) Choi, M.; Na, K.; Kim, J.; Sakamoto, Y.; Terasaki, O.; Ryoo, R.: Stable single-unit-cell nanosheets of zeolite MFI as active and long-lived catalysts. *Nature* **2009**, *461*, 246-U120.

(146) Na, K.; Jo, C.; Kim, J.; Cho, K.; Jung, J.; Seo, Y.; Messinger, R. J.; Chmelka, B. F.; Ryoo, R.: Directing Zeolite Structures into Hierarchically Nanoporous Architectures. *Science* **2011**, *333*, 328-332.

(147) Nair, S.; Villaescusa, L. A.; Camblor, M. A.; Tsapatsis, M.: Zeolite-beta grown epitaxially on SSZ-31 nanofibers. *Chem Commun* **1999**, 921-922.

(148) Okubo, T.; Wakihara, T.; Plevert, J.; Nair, S.; Tsapatsis, M.; Ogawa, Y.; Komiyama, H.; Yoshimura, M.; Davis, M.: Heteroepitaxial growth of a zeolite. *Angew Chem Int Edit* **2001**, *40*, 1069-+.

(149) Liu, J. Q.; Bae, T. H.; Esekhile, O.; Nair, S.; Jones, C. W.; Koros, W. J.: Formation of Mg(OH)(2) nanowhiskers on LTA zeolite surfaces using a sol-gel method. *J Sol-Gel Sci Techn* **2011**, *60*, 189-197.

(150) Lydon, M. E.; Unocic, K. A.; Bae, T. H.; Jones, C. W.; Nair, S.: Structure-Property Relationships of Inorganically Surface-Modified Zeolite Molecular Sieves for Nanocomposite Membrane Fabrication. *J Phys Chem C* **2012**, *116*, 9636-9645.

(151) Hsu, C. Y.; Chiang, A. S. T.; Selvin, R.; Thompson, R. W.: Rapid synthesis of MFI zeolite nanocrystals. *J Phys Chem B* **2005**, *109*, 18804-18814.

(152) Chaidou, C. I.; Pantoleontos, G.; Koutsonikolas, D. E.; Kaldis, S. P.; Sakellaropoulos, G. P.: Gas Separation Properties of Polyimide-Zeolite Mixed Matrix Membranes. *Sep Sci Technol* **2012**, *47*, 950-962.

(153) Zhang, X. Y.; Liu, D. X.; Xu, D. D.; Asahina, S.; Cychosz, K. A.; Agrawal, K. V.; Al Wahedi, Y.; Bhan, A.; Al Hashimi, S.; Terasaki, O.; Thommes, M.; Tsapatsis, M.: Synthesis of Self-Pillared Zeolite Nanosheets by Repetitive Branching. *Science* **2012**, *336*, 1684-1687.

(154) Ramsahye, N. A.; Slater, B.: Incidence and properties of nanoscale defects in silicalite. *Chem Commun* **2006**, 442-444.

(155) Kusakabe, K.; Yoneshige, S.; Murata, A.; Morooka, S.: Morphology and gas permeance of ZSM-5-type zeolite membrane formed on a porous alpha-alumina support tube. *J Membrane Sci* **1996**, *116*, 39-46.

(156) Moghadam, F.; Omidkhah, M. R.; Vasheghani-Farahani, E.; Pedram, M. Z.; Dorosti, F.: The effect of TiO2 nanoparticles on gas transport properties of Matrimid5218-based mixed matrix membranes. *Sep Purif Technol* **2011**, *77*, 128-136.

(157) van Heyden, H.; Mintova, S.; Bein, T.: Nanosized SAPO-34 synthesized from colloidal solutions. *Chem Mater* **2008**, *20*, 2956-2963.

(158) Wilson, S.; Barger, P.: The characteristics of SAPO-34 which influence the conversion of methanol to light olefins. *Micropor Mesopor Mat* **1999**, *29*, 117-126.

(159) Carreon, M. A.; Li, S. G.; Falconer, J. L.; Noble, R. D.: Alumina-supported SAPO-34 membranes for CO2/CH4 separation. *J Am Chem Soc* **2008**, *130*, 5412-+.

(160) Li, S. G.; Carreon, M. A.; Zhang, Y. F.; Funke, H. H.; Noble, R. D.; Falconer, J. L.: Scale-up of SAPO-34 membranes for CO2/CH4 separation. *J Membrane Sci* **2010**, *352*, 7-13.

(161) Arevalo-Hidalgo, A. G.; Santana, J. A.; Fu, R. Q.; Ishikawa, Y.; Hernandez-Maldonado, A. J.: Separation of CO2 from light gas mixtures using nanoporous silicoaluminophosphate sorbents: Effect of multiple-step ion exchange and adsorption mechanism via computational studies. *Micropor Mesopor Mat* **2010**, *130*, 142-153.

(162) Zhu, J.; Cui, Y.; Wang, Y.; Wei, F.: Direct synthesis of hierarchical zeolite from a natural layered material. *Chem Commun* **2009**, 3282-3284.

(163) Balkus, K. J.; Gabrielov, A. G.; Sandler, N.: The Synthesis and Characterization of the Molecular Sieve SAPO-16 as well as Other SAPO and CoAPO Phases Using bis(cyclopentadienyl) cobalt(III) Hydroxide as a Structure Directing Agent. *J Porous Mat* **1995**, *1*, 199-206.

(164) Kirkland, E. J.: *Advanced computing in electron microscopy*; Springer, 2010.

(165) Tan, J.; Liu, Z. M.; Bao, X. H.; Liu, X. C.; Han, X. W.; He, C. Q.; Zhai, R. S.: Crystallization and Si incorporation mechanisms of SAPO-34. *Micropor Mesopor Mat* **2002**, *53*, 97-108.